DISS. ETH No. 16330

CMOS-based Microelectrode Array for Communication with Electrogenic Cells

A dissertation submitted to the

SWISS FEDERAL INSTITUTE OF TECHNOLOGY

for the degree of

DOCTOR OF NATURAL SCIENCE

presented by

Flavio Heer
Dipl. Phys. ETHZ
Born February 11th, 1976
Citizen of Switzerland

accepted on the recommendation of

Prof. Dr. Andreas Hierlemann
Dr. Roland Thewes
Dr. Kay-Uwe Kirstein
Prof. Dr. Henry Baltes

2005

Copyright © 2005 by Flavio Heer, Physical Electronics Laboratory

Cover page: The picture shows a fluorescence image of chicken cortical neurons. The cell nuclei are represented by the blue color, the neurons are shown in red, and glia cells in green. Picture courtesy of Tanja Ugniwenko and Prof. Axel Blau, TU Kaiserslautern, Germany.

Contents

Abbreviations

AP	Action Potential
BPF	Band-Pass Filter
CAM	Cell Adhesion Molecule
CMOS	Complementary Metal Oxide Semiconductor
CMRR	Common Mode Rejection Ratio
COB	Chip on Board
DIV	Days in vitro
ECM	Extracellular Matrix
FET	Field-Effect Transistor
g_{K^+}	Potassium Channel Conductance
g_{Na^+}	Sodium Channel Conductance
HPF	High-Pass Filter
ITO	Indium Tin Oxide
LPF	Low-Pass Filter
MEA	Micro Electrode Array
MEA128	Actual design comprising 128 electrodes
MEA16	First generation chip comprising 16 electrodes
MOS	Metal Oxide Semiconductor
MOSFET	MOS Field Effect Transistor
OpAmp	Operational Amplifier
OTA	Operational Transconductance Amplifier
PBS	Phosphate Buffered Saline
PCB	Printed Circuit Board
PECVD	Plasma Enhanced Chemical Vapor Deposition
PEI	Polyethyleneimine
PSRR	Power Source Rejection Ratio
Pt-black	Platinum Black
RMS	Root Mean Square
SA Node	Sinoatrial Node
THD	Total Harmonic Distortion

Seite Leer /
Blank leaf

Abstract

This thesis reports on the design of a CMOS microelectrode array (MEA) for bidirectional interaction with electrogenic cells. The study of electrogenic cells (e.g. neurons, heart cells, retina cells, or muscle cells) opens a wide area of applications since a myriad of biochemical processes in vertebrates are based on the activity of these cells. MEAs facilitate recordings of electrical events in cell cultures at high spatiotemporal resolution, which facilitates a continuous study of the evolution of cell activity.

Signal acquisition is based on extracellular recording. For extracellular recording, cells are cultured directly on top of a transducing element, which generally is either a metallic electrode or an open-gate transistor. When an action potential occurs in a cell, the local flow of ions in and out of the cell causes a voltage pulse in the cleft between cell and electrode. Extracellular recordings are non-invasive, which facilitates long measurement periods (months), in addition MEAs provide multi-site measurement capabilities.

The 6.5 x 6.5 mm^2 chip presented in this thesis comprises 128 stimulation- and recording-capable electrodes in an 8x16 array. The chip has been fabricated in commercial 0.6 μm CMOS-technology with several post-CMOS processing steps to realize biocompatible electrodes and to ensure chip stability in a physiological environment. The use of CMOS overcomes the interconnect challenge that limits today's bidirectional MEAs using passive substrates. The system comprises all necessary control circuitry and on-chip A/D and D/A conversion. A modular architecture has been implemented, where individual stimulation- and signal-conditioning circuitry units are associated with each electrode. This approach offers important advantages in comparison to other CMOS MEAs published in the literature.

The electronics features include continuous recording of all electrodes at a sampling rate of 20 kHz/electrode and an overall amplification of the electrode potential of 1000 or 3000. An equivalent-input noise of 8.9 μV_{RMS} (1 Hz to 100 kHz) has been measured. An arbitrary stimulation pattern (with a maxi-

mum sampling rate of 60 kHz) can be applied to any subset of electrodes. The readout circuitry at each electrode can be individually reset to its operating point in order to suppress artifacts evoked by the stimulation pulses. An on-chip temperature sensor monitors the temperature of the cell culture.

The noise and impedance spectra of blank-Pt and Pt-black microelectrodes have been measured. The impedance data have been fitted to an commonly used equivalent-circuit model. The electrodes show a charge storage capacity of about 2 - 5 F/m^2 for bright Pt and 150 - 300 F/m^2 for Pt-black. The noise power-spectral density is smaller for larger electrodes. The noise at low frequencies shows a plateau with a $1/f^2$ roll-off, which substantiates the need for AC-coupling, when biological signals are measured with metal electrodes.

Electrophysiological recordings of neural and cardiac cells cultured on the MEA were performed. The biocompatibiltiy of the design has been proven by recording from chicken neurons after as many as 56 days in culture. Peak-to-peak amplitudes of up to 700 μV_{PP} were recorded. Recordings from cardiac myocytes at 5 days in vitro showed amplitudes of 1.8 mV_{PP}. The stimulation capability of the design has been demonstrated by triggering activity in cell cultures originating from primary neonatal rat cardiomyocytes after 4 days in vitro.

Zusammenfassung

Die vorliegende Dissertation beschreibt die Entwicklung, Charakterisierung und Integration eines CMOS Mikroelektrodenarrays (MEA) für extrazelluläre Stimulation und Signalaufzeichnung von Kulturen elektrogener Zellen. Elektrogene Zellen sind Zellen, die elektrische Aktivität zeigen, z.B. Hirn-, Herz-, Retina- oder Muskelzellen. Diese Zellen werden auf dem MEA direkt auf den Elektroden kultiviert. Wenn nun die Zelle ein sogenanntes Aktionspotential generiert, fliessen Ionenströme durch die Zellmembran und erzeugen einen Spannungspuls, der auf den Mikroelektroden messbar ist. Diese Messmethode ist für die Zelle nicht invasiv und ermöglicht lange Messzeiten (Monate) und eine hohe räumliche Auflösung, da viele Elektroden dicht beieinander angeordnet werden können. Das CMOS-System hat ein breites Anwendungsspektrum nicht nur für biochemische Sensormessungen, sondern auch im Bereich der Medikamentenentwicklung/Pharmakologie und Neurowissenschaften.

Der in dieser Arbeit vorgestellte MEA-Chip ist 6.5 x 6.5 mm^2 gross und umfasst 128 Elektroden, die jeweils in beliebiger Konfiguration individuell zur Stimulation und Signalaufzeichnung herangezogen werden können. Der Chip wurde mit Hilfe eines kommerziellen CMOS-Prozesses hergestellt; zusätzliche Nachbearbeitungsschritte zur Realisierung von biokompatiblen Elektroden und zur Abdichtung der Chip-Oberfläche erlauben den Einsatz in physiologischer Umgebung. Der Chip benötigt ein spezielles Packaging, um die elektrischen Anschlüsse vor Flüssigkeit zu schützen und um ein Nährstoff-Reservoir für die Zellkulturen zu haben. Die Verwendung von CMOS-Technologie ermöglicht es, eine grosse Anzahl von Elektroden zu realisieren, da dank der verfügbaren Multiplexer nur wenige elektrische Verbindungen zum Chip benötigt werden. Dadurch wird eine der grössten Beschränkungen von derzeit verfügbaren bidirektionalen MEAs eliminiert. Der MEA Chip umfasst alle nötigen elektronischen Kontrolleinheiten sowie Analog-Digital-Wandler, so dass eine rein digitale Kommunikation mit dem Chip möglich wird. Das MEA ist in einem modularen Aufbau realisiert, d.h. jede einzelne Elektrode ist mit Schaltung zur Stimulation und Signalverarbeitung ausgestattet. Diese Architektur hat im Vergleich zu

anderen publizierten MEAs einige wichtige Vorteile (unter anderem grösserer Rauschabstand), welche im Text näher erläutert werden.

Das Elektronikdesign ermöglicht die gleichzeitige Signalaufzeichnung von allen Elektroden mit einer Abtastrate von 20 kHz/Elektrode und einer Verstärkung von 1000 oder 3000. Das Eingangsrauschen beläuft sich auf 8.9 μV_{RMS} im Bereich von 1 Hz bis 100 kHz. Beliebige Stimulationssignale können mit einer Abtastrate von 60 kHz an eine beliebige Auswahl von Elektroden gesandt werden. Jede Elektrode enthält einen reset-Mechanismus um die Auslese-Schaltung im Falle einer durch Stimulationspulse ausgelösten Übersteuerung schnell wieder in den Arbeitsbereich zurückzubringen. Zudem enthält der Chip einen integrierten Temperatursensor.

Das spektrale Rausch- und Impedanzverhalten der Mikroelektroden wurde ebenfalls im Detail analysiert. Die Kapazität blanker Pt-Elektroden beträgt 2 - 5 F/m^2, diejenige platinierter Elektroden mit grösserer Oberflächenrauhigkeit 150 - 300 F/m^2. Die spektrale Rauschleistungsdichte weist bei niedrigen Frequenzen ein Plateau auf und fällt dann zu höheren Frequenzen hin mit 40 dB/Dekade ab, so dass eine AC-Koppelung der mit Metallelektroden zu messenden biologischen Signale notwendig ist.

Elektrophysiologische Messungen wurden mit Neuronen und Herzzellen durchgeführt. Die Messung spontaner Aktivität in einer Kultur von Hühnerneuronen lieferte Amplituden bis 700 μV_{PP}. Diese Signale stammen von Zellen, die 56 Tage auf dem Chip kultiviert wurden, was die Biokompatibilität des Designs unterstreicht. Messungen an Herzzellen nach 5 Tagen in vitro zeigten Amplituden von 1.8 mV_{PP}. Aktivität in Herzzellkulturen konnte auch mittels auf dem Chip generierter Stimulationssignale ausgelöst werden.

Chapter 1

Introduction

This thesis deals with the design of a microelectrode array (MEA) as a bio-electric device for recording from and stimulation of electrogenic cell cultures. Electrogenic cells (e.g. neurons, heart cells, retina cells, or muscle cells) are cells that have the ability to produce or undergo transient transmembrane voltage changes, which are called action potentials [1]. The study of electrogenic cells opens a wide area of applications since a myriad of biochemical processes in vertebrates are based on the activity of these cells. Furthermore, diseases based on malfunction of electrogenic cells are among the most serious health problems. The cell activity can be measured extracellularly by using a microelectrode, which is generally a metallic electrode with similar diameter as the cell. In a MEA, numerous electrodes are arranged in an array on a planar substrate. MEAs fabricated in complementary metal oxide semiconductor (CMOS[1]) technology have several advantages as compared to traditional technologies.

1.1 Motivation

MEAs have become an important tool in the fields of neuroscience and biosensing. Many groups have shown that neural networks show a specific answer to external stimulation [2–7]. Additionally, cell cultures are very sensitive to their chemical environment and allow for the detection of biochemically active agents. Cell cultures on MEAs are, therefore, suitable for the development of hybrid bioelectric sensor systems for:

---

[1]CMOS stands for "complementary metal oxide semiconductor" and is the standard technology for application-specific integrated circuits (ASICs) and digital chip design, such as microprocessors.

1

- studying fundamentals in learning processes, aging and mental diseases on a small and defined neuronal network [3,4],

- drug development through screening of pharmacological effects of compounds complementary to high throughput screening and animal testing [2,8–11],

- environmental monitoring for the detection of toxic substances, e.g. biohazard detection [12],

- studying the cellular effects of mixtures of compounds and dosing sequences.

The use of CMOS electronics overcomes the drawbacks of traditional MEAs. Traditionally, MEAs encompass a passive MEA chip with external signal conditioning electronics and a system control that is realized by discrete off-chip components (table 1.1). Each individual electrode needs to be wired to the external electronics, which limits the size of the array. CMOS electronics offer on-chip multiplexers, which enable the integration of a large number of electrodes, so that chips with up to 128x128 electrodes have been presented in the literature [13, 14]. Another advantage of CMOS is the availability of MOS switches, which allow to use the electrode for both, recording and stimulation.

In vitro^2 cultured cells have several advantages over intact organisms. First, most animal and plant tissues comprise a variety of different types of cells, whereas cells of a specific type can be grown in culture. Thus cultured cells are more homogeneous in their properties than in vivo^3 cells in tissues. Second, experimental conditions can be controlled much more rigorously in culture than in an organism. A disadvantage of in vitro studies is that the results may not be representative for in vivo. Nevertheless, it is envisioned that biosensors based on cells or cell cultures will at least partly replace animals in toxicology studies [15].

1.2 Applications

The MEA finds a multitude of applications in both applied and pure science. In pure science it offers a platform with which the fundamentals of neuronal

---

^{2}In vitro (Latin: "within glass"), means outside a living organis,. e.g., cells on a glass substrate.

^{3}In vivo (Latin: "within the living". In vivo is used to indicate the location of the cells in a whole/living organism.

networks may be investigated; in applied science, chemical and biological compounds can be detected using MEAs as cell-based biosensors where the cell acts as the primary transducer. A brief introduction of the use of MEAs in these two application areas is given in this section.

Pure science: Neuroscience and computing

A high degree of parallel connectivity and the coordinated electrical activity of neural networks is believed to be the reason that the brain is capable of highly sophisticated information processing. In order to understand this complex neural processing, high spatio-temporal resolution techniques to monitor the electrical activity are required. A device featuring a large number of bidirectional (stimulation and recording) contacts to such networks could disclose the secrets of how information is processed and stored in our brain. Two approaches exist to study the activity of neuronal networks: *in vivo* with whole animals or humans and *in vitro* using neural cell cultures.

For in vivo studies of neural signal processing several well-established and non-invasive techniques, such as electroencephalography (EEG) [16], positron emission tomography (PET) and functional magnetic resonance imaging (fMRI) [17] are available today. However, to date, real-time recordings at a temporal resolution of milliseconds from hundreds of neurons can only be attained by means of invasive multichannel recording techniques using implanted micro-electrode fibers in awake or anesthetized animals [18,19].

In vitro natural neural networks show most of the self-organizing phenomena and plasticity that can be identified in vivo. Despite their limited sizes, in vitro networks are capable of establishing robust information processing functionalities once they are exposed to stimuli in a closed-loop feedback scenario [3,4,20-23]. In vitro networks of neurons provide a unique view into learning and memory in networks, with high spatio-temporal resolution.

Applied science: Pharmacological and medical applications

MEA-based biosensors are promising tools for the detection of chemical and biological toxins or for the screening of pharmacologically active compounds [2,24-29]. Diseases based on electrogenic cells are among the most serious

health problems, such as cardiac or mental diseases[4]. Another interesting field is the use of MEAs in neural prosthetic devices.

Cardiac and non-cardiac drugs affect the functioning of the heart. One possible effect is delayed ventricular repolarization (QT prolongation), which can lead to arrhythmias. Electrophysiological studies have to be included in cardiac safety pharmacology for assessing the potential of pharmaceuticals for QT prolongation (ICH S7B Document, [30]) [10]. For example, Meyer et al. demonstrated that drug-induced QT prolongation can be observed in cardiac cell cultures [11]. Another example for cardiac cell cultures as biochemical sensors has been presented by the group of G. T. A. Kovacs, Stanford University. They developed a field-portable systems using cardiomyocytes for warfare agent monitoring, especially for the detection of toxins [31–33].

Neural networks on MEAs in culture provide a highly stable system for long-term monitoring of spontaneous or evoked electrophysiological activity. In the absence of the homeostatic control mechanisms of the central nervous system, these networks show remarkable sensitivities to minute chemical changes and mimic some of the properties of sensory tissue. These sensitivities could be enhanced by using engineered cells with altered receptor expression. The change in spontaneous or evoked network activity can be used to detect chemical substances. In the group of G. W. Gross, University of North Texas, neuronal-network-based biosensors have been used to demonstrate that in vitro cultures retain tissue-specific properties. Moreover, findings corroborate well with whole-animal in vivo studies [2, 27, 28]. In the group of S. Martinoia, University of Genova, dissociated spinal cord neurons from chicken embryos have been used to analyze changes in activity patterns induced by exposing the culture to drugs that act on the glutamate receptors (NMDA and non-NMDA) [5]. Changes in burst duration, inter-burst intervals, burst amplitudes, as well as inter-spike intervals were used to characterize the effects of drug exposure. The same receptors were also analyzed by the group of G. W. Gross [34].

In neural prosthetics research, microdevices might become a new approach to recover skeletal muscle function [18, 35], visual perception [36] or the auditory system [37, 38]. The design and realization of devices with electrodes for electrical coupling of nerves within regeneration studies is under research for more than 25 years. The concept was first investigated on amphibians in 1974 [39]

---

[4]Two examples: deaths in USA caused by cardiovascular disease: 47.3% male and 52.7% female, annual costs estimated at $286.5 billion. (Source: Statistics related to heart decease, University of Maryland, www.umm.edu/cardiac/stats.htm). About 4.5 million Americans have Alzheimer's disease, this number has doubled since 1980. (Source: Alzheimer's Association, http://www.alz.org/AboutAD/statistics.asp)

Company	System	Array size	Material	Substrate
Multi Channel Systems	MEA 1060 AMP	60	TiN, Au	Glass
Panasonic	MED64	64	ITO, Pt	Glass
Plexon Inc.	MEA Workstation	64	-	-
Bionas	Neuro Chip SC1000N	54	Pd/Pt	Silicon

Table 1.1: Commercially available MEA systems.

with epoxy-based devices including silver wires as electrodes. The devices became smaller by using micromachining technology [35,40–42]. Monolithic integration based on silicon electronics has also been reported [19,43,44]. The most successful microelectrode-based biohybrid device is the cochlea implant. Since more than 20 years these prosthetic devices are implanted in the inner ear and can restore partial hearing to profoundly deaf people [37,38]. Other devices using electrodes that are regularly implanted are cardiac pacemakers, and electrodes in the brain for deep brain stimulation as an effective therapy for Parkinson's disease and epilepsy.

1.3 State of the Art

Several laboratories have established the capability to perform extracellular recordings from neuronal or cardiac cells cultured on MEAs [2–6, 12, 25, 32, 33,45–56]. Such MEAs have been used to study the effects of pharmacological agents on neuronal net activity [2] to detect neurotoxicants [28], or for investigating neural network dynamics [3,4,51,56]. Commercially available systems are provided by several companies[5], an overview is given in table 1.1. In all these commercial systems, each electrode needs to be wired to the external electronics. This adds parasitic capacitance, which attenuates the weak electric signals and limits the array size.

Silicon MEAs based on open-gate field-effect transistors (OGFETs) as electrodes are currently developed by the group of P. Fromherz, MPI Munich, [7, 58–60] and also by Offenhaeuser et al. [61,62]. Another CMOS microelectrode

---

[5]Multi Channel Systems GmbH, Germany, www.multichannelsystems.com [57]; Panasonic, Japan, www.med64.com; Plexon Inc., USA, www.plexoninc.com; Bionas, Germany, www.bionas.de.

approach with palladium (Pd) electrodes but yet without on-chip electronics has been reported by Baumann et al. [54]. None of these devices exhibits any on-chip circuitry or electronic components other than the transducers (electrodes, FETs) themselves. The use of on-chip microelectronics is imperative for larger MEAs with stimulation and recording capabilities. A MEA with integrated multiplexers and in-pixel amplifiers, which can simultaneously record from 4096 electrodes with a 20 μm pitch was presented by Berdondini et al. [63]; a design with 16384 electrodes with 7.8 μm pitch was presented by Eversmann et al. [13, 64–66]. These high-density arrays exhibit high noise levels due to the limited area for in-pixel amplifiers. What is more, stimulation capability is not included. Electrical stimulation is necessary to study connectivity in neuronal networks. A CMOS chip with on-chip stimulation using an integrated stimulation electrode located close to the microelectrode array has been presented by the group of G. T. A. Kovacs at Stanford [12, 32, 33]. For in vivo applications, separate stimulation and recording probes, each featuring 64 electrodes and 8 channels, have been incorporated in a 3D-electrode array by K. Wise and K. Najafi [19]. Jimbo and co-workers have presented a passive MEA where electrodes can be switched between recording and stimulation [55]. This design is based on discrete off-chip components and, therefore, the array size is limited and signals are attenuated due to interconnection of electrodes to external electronics, as mentioned previously.

1.4 Scope of the Thesis

This thesis aims at designing a MEA-based biohybrid device to *bidirectionally* connect to neuronal and cardiac networks in vitro. One scientific objective is to develop a device that can be used to interconnect cortical neural networks in vitro to study stimulus-induced information processing in neural networks. Such a device is targeted at gaining a better understanding of elementary neural information processing and coding schemes in learning, memory formation, and memory retrieval. A second objective is to use this device to study neural and cardiac network response upon exposure to a chemical agent.

Standard CMOS technology has been chosen to fabricate the MEA in order to use on-chip multiplexing to overcome the connectivity problem of traditional passive MEAs. This technology additionally allows the integration of on-chip electronics to potentially improve the signal-to-noise characteristics. Additionally, the physical dimensions of such a system can be drastically reduced by monolithic integration of the electrode array together with all the necessary

electronics on the same substrate.

The thesis is organized in five major chapters.

Chapter 2 explains the basics of action potential generation in electrogenic cells. Additionally, the principle of extracellular recording of an action potential is explained.

Chapter 3 presents impedance and noise measurements of microelectrodes. The parameters have been extracted employing a commonly used equivalent-circuit model for the microelectrode. Additionally, an equivalent-circuit model for the cell-electrode system will be described and a sensitivity analysis of the important parameters will be presented.

The overall system architecture of a monolithic 128-electrode CMOS MEA (termed "MEA128") is presented in chapter 4. Design, modeling and fabrication will be described in detail. In section 4.2 the post-processing and packaging to ensure biocompatibility of the design are laid out. A predecessor design (termed "MEA16") will be briefly introduced in section 4.3 and compared with the MEA128. Finally, an outlook and possible improvements are discussed in section 4.4.

Measurement results are presented in chapter 5. Electrical characterization of the MEA128 will be given in the first section of this chapter. The second section will present measurements from neuronal and cardiac cell cultures.

Finally, a conclusion and a outlook will be given in chapter 6.

1.5   Major Results

Monolithic CMOS MEA with 128 electrodes

A CMOS metal-electrode-based micro system for bidirectional communication with electrogenic cells in vitro has been developed. The 6.5 mm by 6.5 mm chip shown in Figure 1.1 has been fabricated in an industrial 0.6 μm CMOS-technology with several post-CMOS processing steps to realize biocompatible electrodes and to ensure chip stability under physiological conditions.
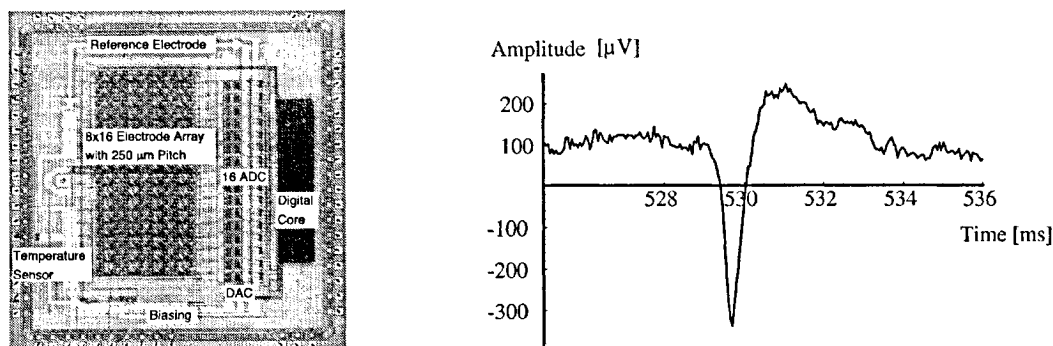
Figure 1.1: Micrograph of the monolithic CMOS MEA (left). Neural spike recorded using the CMOS MEA: peak-to-peak amplitudes of up to 700 μV have been recorded (right).

The system comprises all necessary control circuitry and on-chip A/D and D/A conversion. A modular architecture has been implemented, in which individual stimulation- and signal-conditioning circuitry units have been associated with each electrode. This approach offers important advantages in comparison to other CMOS MEAs published previously [12–14,19,44]: (i) The signal is amplified and filtered in close proximity of the electrodes, which makes the design less sensitive to noise and interference picked up along connection lines; (ii) a buffer per electrode renders the stimulation signal independent of the number of activated electrodes; (iii) the high-pass filter removes offset and drift of the biochemical signals and, therefore, the signal can be amplified before it is multiplexed; (vi) the low-pass filter limits the noise bandwidth and works as an anti-aliasing filter for the multiplexing and for subsequent A/D-conversion.

Recordings of neuronal cultures after 56 DIV

Neural networks were successfully cultured on the chip. Figure 1.1 shows a recording from the spontaneously active cells after 56 DIV (days in vitro). The signals recorded from 30-μm-diameter electrodes showed signal amplitudes between 500 μV and 700 μV, the signals from 40-μm-diameter electrodes were in a range between 200 μV and 300 μV. The signal amplitudes are seemingly inversely proportional to the area of the electrodes, which is in agreement with the models used for electrogenic cells on microelectrodes as described in chapter 3 and in the literature [67,68].

Equivalent-circuit model
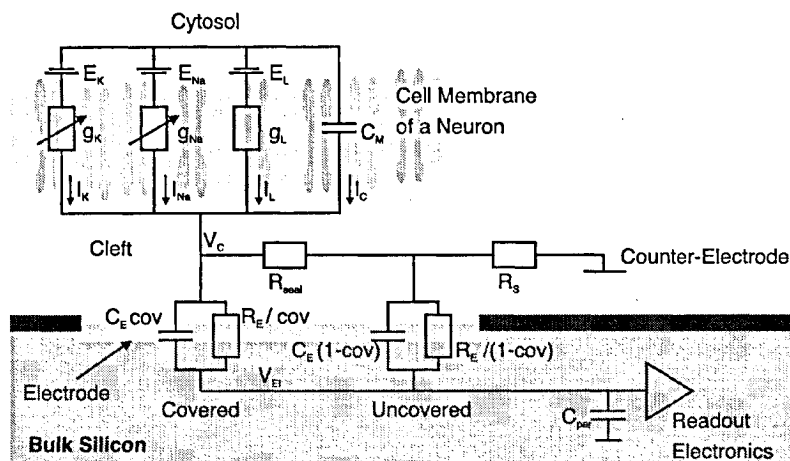
Figure 1.3: Equivalent circuit model of the electrode-neuron interface.

The equivalent-circuit model shown in Figure 1.3 of the neuron-electrode system is analyzed. The model assumes that the metal electrode is only partly covered by the electrogenic cell. A sensitivity analysis with regard to changing important parameters is given.

Packaging of CMOS MEAs

Packaging and post-CMOS processing [69] constitute key-issues when living cells have to survive several months on the surface of a silicon chip. Our approach led to culture periods of several months. Signals were recorded at 56 DIV.

Stimulation and recording of cardiac cell cultures

Primary neonatal rat cardiomyocytes were successfully cultured on the chip. Figure 1.2 illustrates the stimulation and recording of a cardiac cell culture after 4 DIV. In this example, the cells beat at a rate of about 1 Hz. A stimulation pulse (arrows) realized by the on-chip circuitry stimulates the culture and induces a new sequence of action potentials.
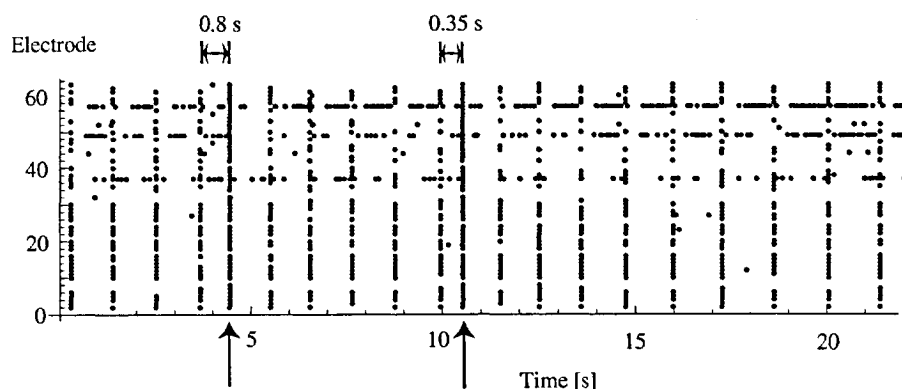
Figure 1.2: Stimulation of and recording from a cardiac cell culture on an array of 8-x-8 electrodes. The y-axis represents the electrode number. Stimulation pulses are indicated by the arrows.

Electrode characterization

The noise and impedance spectra of blank-Pt and Pt-black microelectrodes has been measured. The impedance data has been fitted to an commonly used equivalent circuit model. The electrodes show a charge storage capacity of about 2 - 5 F/m^2 for bright-Pt and 150 - 300 F/m^2 for Pt-black. The noise power-spectral density is smaller for larger electrodes. The noise at low-frequencies shows a plateau with a $1/f^2$ roll-off, this substantiates the nead for AC-coupling of biological signals measured with metal electrodes.

Chapter 2

Fundamentals of Extracellular Recording

2.1 Biology of Electrogenic Cells

Many cells in the body have the ability to undergo a transient depolarization and repolarization that is either triggered by external mechanisms (e.g., motor nerve stimulation of skeletal muscle or cell-to-cell depolarization in the heart) or by intracellular, spontaneous mechanisms (e.g., cardiac pacemaker cells). Cells that exhibit the ability to become electrically active are called electrogenic cells. The biology of these electrogenic cells is rather complex because many cross-linked electrical, electro-physiological and biochemical processes are involved.

A brief description of the biology of electrogenic cells is given in this chapter. The mechanism of voltage-gated ion channels, action potentials and the conduction of action potentials through a cellular network will be described for neurons. Further introduced is the action potential generation in cardiac cells. Many of the underlying mechanisms are similar for neurons and cardiac cells, e.g., voltage gated ion channels. For a more detailed explanation about the functioning of electrogenic cells, the reader is directed to various books on this topic, e. g., [70–72].

2.1.1 The Neuron

The nervous system regulates all aspects of body functions and is staggering in its complexity. The human brain contains about 10^{12} neurons (nerve cells),

each forming as many as a thousand connections to other neurons. The nervous system also contains glial cells that occupy the spaces between neurons and modulate their function. They surround the soma and axons of the neurons and are metabolically coupled to the neurons. The output of a nervous system is the result of its circuit properties, that is, the wiring or interconnections (synapses) between neurons, and the strength of these interconnections. These synaptic connections between neurons can be reorganized, which is known as synaptic plasticity, and is believed to be the mechanism of learning in our brain.

Basically, three different types of neurons can be distinguished by their physiology and function in the body (Figure 2.1).

- **interneurons**, neurons in contact with other neurons (most of the interneurons are located in the brain)

- **motor neurons**, neurons which control the actions of the organism mainly via contact with muscle cells

- **sensor neurons**, neurons which receive stimuli from the external environment, such as the retina,

The neuron contains four distinct regions with different functions: the cell body, the dendrites, the axon and the axon terminals (Figure 2.1).

1. The **cell body** with a diameter of 10 to 50 µm contains the nucleus and is the production site of most neuronal proteins. Some proteins are synthesized in the dendrites, but no proteins are made in axons, since they do not contain ribosomes. Proteins that are required in the axon are synthesized in the cell body and transported along microtubules down the length of the axon by a process called *anterograde transport*.

2. Almost every neuron has a single **axon**, whose diameter varies from a micrometer in the human brain to a millimeter in the giant squid. Axons are specialized for the conduction of electrical pulses, termed "action potentials" [1], away from the cell body toward the axon terminus. The point, where the axon is connected to the cell body, is called the axon hillock. Whenever the membrane is depolarized at the axon hillock, an action potential starts propagating along the axon. Action potentials move rapidly, at speeds up to 100 m/s. In humans, axons may be more than a meter long, yet it takes only a few milliseconds for an action potential to move along their length. The reason for this lies in the myelination (see page 16).
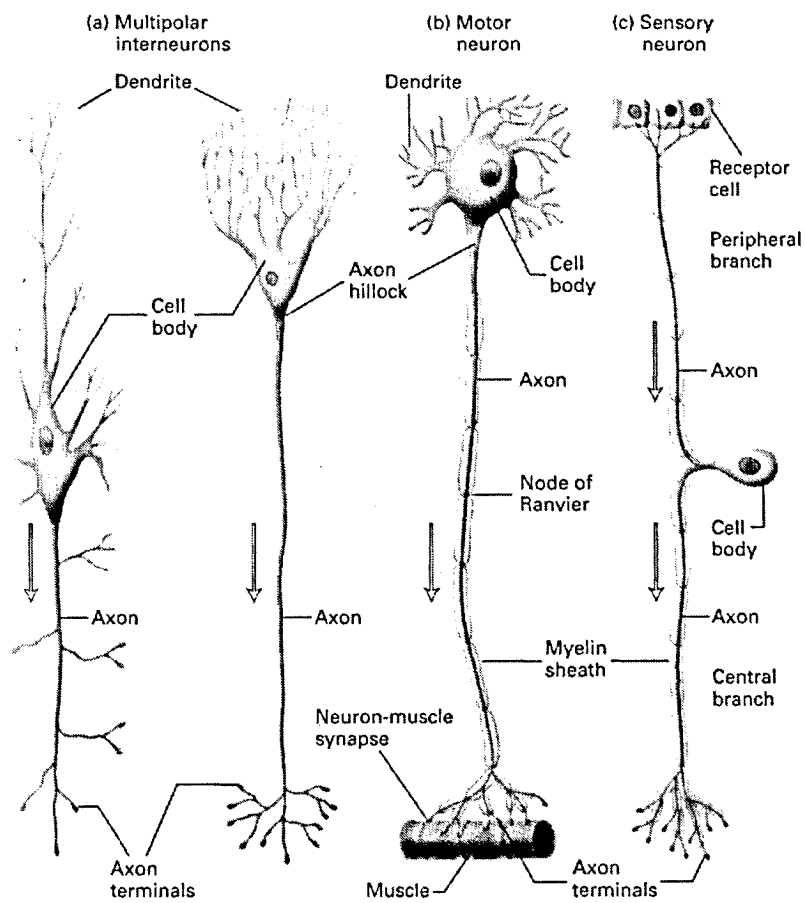
Figure 2.1: Structures of typical mammalian neurons. Arrows indicate the direction of the action potential conduction in the axons. Adapted from [72].
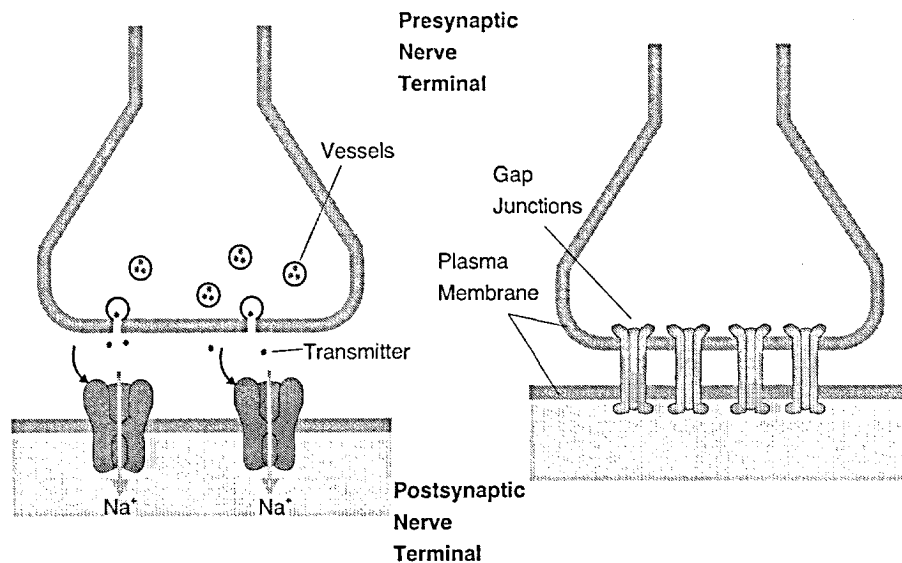
Figure 2.2: Chemical (left) and Electrical (right) Synapse.

3. Most neurons have multiple **dendrites**, which extend outward from the cell body and are specialized to receive chemical or electrical signals from the axon terminals of other neurons via the synapses. Dendrites convert these signals into small electric impulses and transmit them towards of the cell body. Particularly in the central nervous system, neurons have extremely long dendrites exhibiting complex branching. This allows them to receive signals from a large number of other neurons, on average a thousand in the human brain. The signals from all dendritic inputs are integrated in the cell body, which leads to an increase in the intracellular voltage, and if this disturbance is large enough, an action potential will originate and will be actively conducted down the axon.

4. Neurons have up to 1000 **presynaptic terminals** or **axon terminals**. These terminals at the axon endings transfer information to the dendrites or somata of other neurons, or to other target cells such as muscle fibers, either chemically by means of neurotransmitters, or, less often, electrically through direct contact of the terminals with the target cell.

Synapses

Neurons communicate with one another through specialized contact zones, which are called synapses. There are about 10^{15} synapses in a human brain. Synapses generally transmit signals in only one direction, from the axon terminal of the

presynaptic cell to the dendrites (axodendritic), or less often to the cell body (axosomatic) or a different axon (axoaxonic) of the postsynaptic cell. Synapses can be either electrical or chemical (Figure 2.2). In electrical synapses, the signal travels directly via the gap junctions from one cell to the other without the involvement of any transmitter substance. These gap junctions consist of specialized proteins that form channels bridging the interior of two neurons and allow for direct current flow from one neuron to the other. In the chemical synapse, the axon terminal of the presynaptic cell contains vesicles filled with a particular neurotransmitter, e.g., acetylcholine, glutamate, dopamine. When an action potential in the presynaptic cell reaches an axon terminal, some of the vesicles fuse with the plasma membrane releasing their contents into the synaptic cleft, the narrow space between the cells. The neurotransmitters diffuse across the synaptic cleft and bind to receptors of the postsynaptic cell. This binding triggers changes in the ion permeability in the postsynaptic plasma membrane, which, in turn, changes the membrane's electric potential. Chemical synapses have two important advantages over electric ones in the transmission of impulses from a presynaptic cell. The first is signal amplification, which is common at nerve-muscle synapses. A single motor neuron can cause a contraction of multiple muscle cells because the release of relatively few signaling molecules is required at the synapse to stimulate contractions. The second advantage is signal computation, which is common at synapses involving interneurons. A single neuron can be affected simultaneously by signals received at multiple excitatory, inhibitory and also electrical synapses. The neuron averages these signals continuously and determines whether or not to generate an action potential. The connection between two neurons is therefore weighted by the property of the synapse, which connects the two neurons. This is the basis of the ability of neural networks to perform computation.

Glial cells

There are two main classes of cells in the nervous system: nerve cells (neurons) and glial cells (glia, Greek: glue). Glial cells (see Figure 2.3) are about 10 to 50 times larger in number than neurons. Three different types of glial cells can be distinguished by their form and function: astrocytes and oligodendrocytes in the central nervous system and Schwann cells in the peripheral nervous system. As far as is known, glia are not directly involved in information processing, but they have many vital roles. They surround the soma and axons of the neurons and are metabolically coupled to the neurons [73]. Oligodendrocytes and Schwann cells produce myelin, which is used to insulate nerve cell axons as
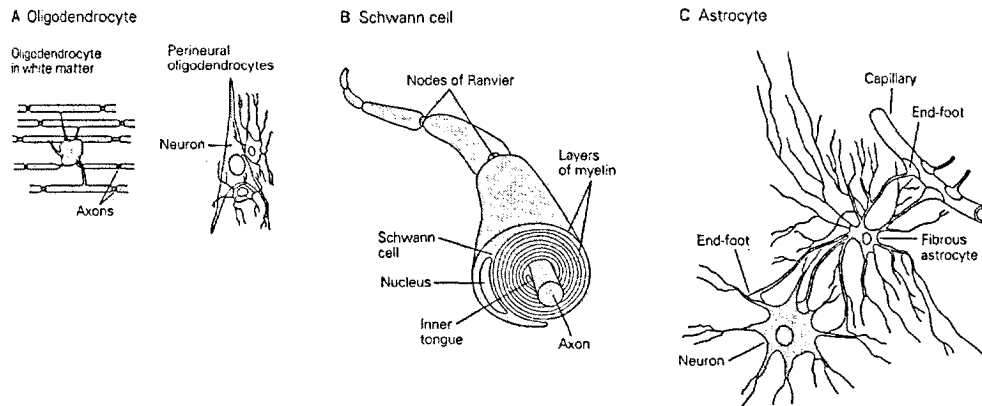
Figure 2.3: The principal types of glial cells in the central nervous system include astrocytes and oligodendrocytes, those in the peripheral nervous system are Schwann cells. Adapted from [71].

described below. Some glias guide neurons and axons during the brain's development. Finally, some glia act as mobile removers of cell debris. Nowadays, glia cells are becoming more important because many neurological diseases, such as multiple sclerosis, are connected to glia cells and not to neurons [74].

Myelination and Impulse Conduction

The axons are coated with a white 3 to 10 µm thick myelin sheath (Figure 2.3), which increases the velocity of the impulse conduction to up to 100 m/s as compared to about 1 m/s for unmyelinated axons. Without myelination the coordination of fast and complex movements such as running would be impossible. Myelin is a stack of specialized plasma membrane sheets produced by glial cells that wraps itself around the axon. In the peripheral nervous system, these glial cells are called Schwann cells, in the central nervous system, they are called oligodendrocytes. Often several axons are surrounded by a single glial cell. Several axons can be surrounded by a single glial cell, as it is the case for oligodendrocytes.

Myelination has two effects. The axon is isolated from the exoplasm, so that the excess cytosolic ions spread passively through the axonal cytosol to the next node with very little loss or attenuation. Second, the myelination reduces the capacitance of the axon membrane against the extracellular medium. Both effects result in an increased conduction velocity.

Each region of myelin formed by an individual glial cell is separated from the next myelinated region by an unmyelinated area called the node of Ranvier

(Figure 2.1 and 2.3). Because the myelin sheath prevents the transfer of ions between the axonal cytosol and the extracellular fluids, all electric activity in axons is confined to the nodes of Ranvier, where ions can flow across the axonal membrane. Such locally restricted electric activity results in the so-called *saltatory conduction*. Electrical impulse conduction in axons or dendrites can be modeled using the concepts developed in cable theory and by incorporating the active plasma membrane.

Cell-substrate Adhesion, Cell-Cell Coupling

Animal cells grown in culture must be supplied with a rich medium[1] and typically grow only when attached to a specifically coated surface. Unlike bacterial and yeast cells, which can be grown in suspension, most cultured animal cells require a surface to grow on. Cells prefer to adhere to positively charged surfaces (at physiological conditions), whereas negatively charged surfaces tend to be repulsive and, therefore, have anti-adhesive properties. Traditionally, glass was used as the substrate for cell cultures because of its optical properties and because it carries the correct charge for cells to adhere and grow. Today, the use of glass has been largely superseeded by the use of plastic. All tissue-cultures plastics are treated to produce a charged surface which is wettable [75].

The tendency of animal cells to interact in vivo with one another and with the surrounding extracellular matrix (ECM) is mimicked in culture. Three main units are involved in the adhesion of a cell to a substrate: the cytoskeleton, transmembrane cell-adhesion molecules (CAMs), and the ECM (Figure 2.4). The cytoskeleton consists of three types of cytosolic fibers: microfilaments, intermediate filaments and microtubules. These cytoskeletal fibers are well organized polymers built from small protein subunits held together by covalent bonds. The cytoskeleton plays a structural role by supporting the cell membrane and by forming tracks along which organelles and other elements can move in the cytosol. The cytoskeleton undergoes permanent rearrangement which can produce movements.

Various integral membrane proteins, collectively termed cell-adhesion molecules (CAMs, see Figure 2.5), enable many animal cells to adhere tightly and

---

[1]Animal cells grown in culture must by supplied with a rich medium containing various amino acids (especially the essential amino acids that cannot be synthesized by the cells), vitamins, salts, glucose and serum. Serum is an important component in media for growing animal cells and contains most, if not all, of the growth factors and hormones that cells require for their growth. Typical examples are foetal bovine, newborn calf, donor calf, horse, chicken and human serum
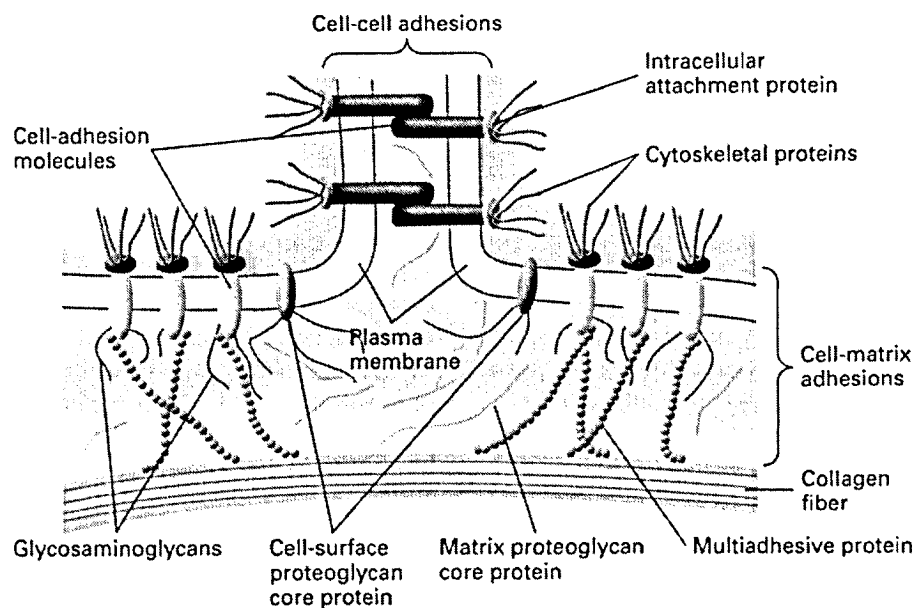
Figure 2.4: Schematic overview of the types of molecules that bind cells to each other and to the extracellular matrix (ECM). Cell-adhesion molecules (CAMs) are integral membrane proteins. Some interact with similar molecules of other cells. Other CAMs form connections with components of the extracellular matrix. These interactions allow cells to adhere to one another, interconnect the cytoskeletons of adjacent cells, and give tissues their strength and resistance to shear and tensile forces. Adapted from [72].
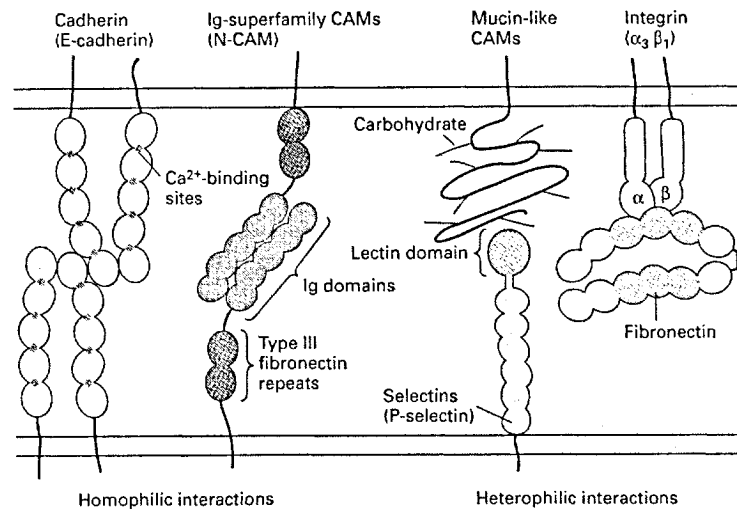
Figure 2.5: Major families of cell-adhesion molecules (CAMs). Cadherin and the immunoglobulin (Ig) superfamily of CAMs mediate homophilic cell-cell adhesion. The major cell-matrix adhesion molecule, integrin, is a heterodimer of α- and β-subunits. They bind to the cell-binding domain of fibronectin, laminin, or other matrix molecules. Adapted from [72].

specifically to cells of the same or similar type; these interactions allow populations of cells to segregate into distinct tissue. Most CAMs are uniformly distributed along the regions of plasma membranes that contact other cells, and the cytosol-facing domains of these proteins are usually connected to the cytoskeleton. The major cell-matrix adhesion molecule, integrin, is a heterodimer of α- and β-subunits. Integrins bind to the cell-binding domain of fibronectin, laminin[2], collagen or other matrix molecules. Focal adhesion and hemidesmosomes are integrin-containing junctions that attach cells to fibronectin, an element of the basal lamina in the ECM.

The cells also contact the ECM, a complex network of secreted proteins and carbohydrates that fill the spaces between cells. The ECM, whose constituents are secreted by cells themselves, helps binding the cells in tissues together and also provides a lattice, through which cells can move. The ECM consists of fibrous collagen proteins, hyaluronan, and covalently linked polysaccharides

---

[2]Besides other cell adhesion molecules, much attention has been directed to laminin in the literature. Laminin supports cell adhesion of almost all cells in the body and, therefore, can be found in all regions of the body. Laminin is a heterotrimeric, multiadhesive protein consisting of three chain-like subunits, α, β_1 and β_2 with globular domains in each. The different regions bind to cell-surface receptors and various ECM components. Laminin has also been used for the cultivation of cardiac cells and neurons on the MEA128 described in chapter 4 and 5.

Exterior   4 mM K⁺   150 mM Na⁺   120 mM Cl⁻

Cytosol   140 mM K⁺   12 mM Na⁺   4 mM Cl⁻
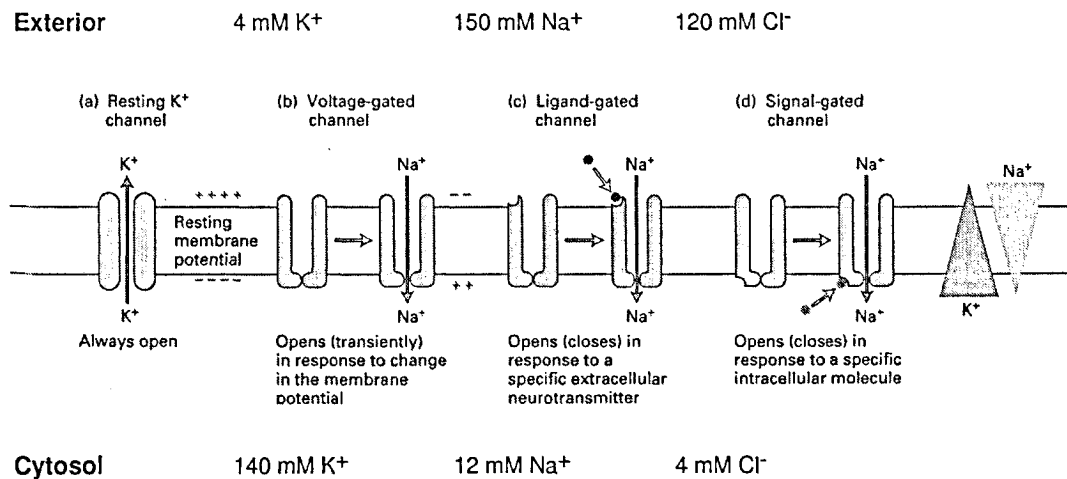
Figure 2.6: Neural ion channel proteins. Each type of channel protein has a specific function in the electrical activity of neurons. Adapted from [72].

and proteins.

2.1.2 Voltage-Gated Ion Channels and the Neural Action Potential

Different ion concentrations inside and outside the cell lead to an electric potential across the plasma membrane of cells. In virtually all cases the inside of the cell membrane is negatively charged relative to the outside. Typical membrane potentials are between -30 mV and -70 mV. The membrane potential of most animal cells generally does not vary with time. In contrast, neurons and muscle cells, the principle types of electrically active cells, undergo controlled change in their membrane potential which is called an action potential. The concentration of K^+ ions inside typical metazoan cells is about 10 times larger than that in the extracellular fluid, whereas the concentrations of Na^+ and Cl^- ions are much higher outside the cell than inside. These concentration gradients are maintained by membrane proteins that are capable of pumping ions from one side of the membrane to the other, often against their concentration gradients. The action of these proteins consumes energy, which is generated by the hydrolysis of ATP molecules. Therefore, these protein pumps are also named ATPases. For example the Na^+-K^+ pump transports three Na^+ out for every two K^+ pumped in. Thus the net exchange of ions is one cation out per pump turnover.

The resting potential

The resting potential is determined mainly by the movement of K^+ ions. The plasma membrane contains *resting K^+ ion channels* which are open in the resting state and allow the passage of only K^+ ions. The K^+ ions move across the membrane down their concentration gradient according to the Nernst equation (equation 2.1), which leaves an excess negative charge on the cytosolic face and deposits positive charge on the exoplasmic face. In a redox reaction, the energy released due to movement of charged particles gives rise to a potential difference. The *Nernst equation* allows us to calculate the maximum potential difference (called the electromotive force), E, for any concentrations. E is given by the product of the thermal voltage kT/q and the concentration difference.

$$E = \frac{kT}{q} ln \frac{[C_o]}{[C_i]} \qquad (2.1)$$

Quantitatively, the resting potential is about -60 mV and is close to E_K(-91 mV), the potassium equilibrium potential, calculated from the Nernst equation applying the typical cytosolic and exoplasmic concentrations. However, the situation is more complex, since some open Na^+ and Cl^- channels exist as well. Additionally, there are more types of ion-channels involved, but the membrane potential of electrically active cells is primarily affected by the opening and closing of ion channels for K^+, Na^+ and Cl^-.

The electric potential, E, across a cell surface membrane is given by a more complex version of the Nernst equation, the GHK (Goldman-Hodgkin-Katz) voltage equation (equation 2.2), in which the concentrations of the ions are weighted in proportion to the magnitudes of their permeability constants P. In equation 2.2 "i" and "o" subscripts denote the ion concentration inside and outside the cell respectively. P is a measure of the ease, with which an ion can cross a unit area of a membrane driven by 1 M difference in concentration; it is proportional to the number of open ion channels and the number of ions that each channel can conduct per second. Thus, P_{Na}, P_K and P_{Cl} are measures of the "leakiness" of a unit area of the membrane to these ions. Note that only the ratios of the permeability constants is important not their absolute values. This can easily be seen when the numerator and the denominator are divided by, e. g., P_K.

$$E = \frac{kT}{q} ln \frac{[K_o]P_K + [Na_o]P_{Na} + [Cl_i]P_{Cl}}{[K_i]P_K + [Na_i]P_{Na} + [Cl_o]P_{Cl}} \qquad (2.2)$$

In resting neurons the ion concentrations are typically those shown in Figure 2.6. The permeability of the membrane to Na^+ and Cl^- ions is about one tenth of that for K^+, since there are about ten times more open K^+ channels than open channels for Na^+ or Cl^-. By inserting the typical ion concentrations into equation 2.2, the potential of the resting membrane is -52.9 mV.

Voltage-gated ion channels

Ion channels are embedded transmembrane proteins and allow for the formation of a concentration gradient between extracellular and intracellular space. These ion channels are termed "gated" if they can be opened or closed. There are three types of gated ion channels: ligand-gated, mechanically gated and voltage-gated.

Ligand-gated channels open or close in response to the binding of a small signaling molecule or *ligand*. These ligands can be extracellular or intracellular signal molecules. *Mechanically gated* channels open due to deformation and lead to the triggering of nerve impulses. One example are the hair cells in the inner ear, which produce nerve impulses that the brain interprets as sound. *Voltage-gated* channels are found in electrogenic cells. They open or close in response to changes in the voltage across the plasma membrane (Figure 2.6). The channel proteins of voltage-gated channels contain four voltage-sensing α helices, which have positively charged side chains. The attraction of these charges to the negative interior of resting cells helps to keep the channel closed. When the membrane depolarizes, the voltage-sensitive helices move toward the outer membrane surface, causing a conformational change in the channel protein, and the channel opens for the influx of Na^+ ions. When a region of the plasma membrane is slightly depolarized, the plasma membrane becomes 500 times more permeable for sodium cations for about one millisecond (Figure 2.7). The influx of the Na^+ ions causes a sudden transient depolarization associated with an action potential. The membrane potential becomes more positive, approaching the value of E_{Na} (~64 mV) and causing the voltage-gated K^+ ion channels to open. The opening of the voltage-gated K^+ ion channels results in an efflux of K^+ ions, which causes the membrane potential to become negative again and even hyperpolarizes by approximately 10 mV for a brief period, approximately two milliseconds. The total transmembrane peak-to-peak voltage amounts to around 100 mV. With the restitution of the original potential gradient after a total duration of the action potential of approximately 1 ms to 4 ms, the neuron cannot be stimulated for a period of usually another millisecond, which is called the refractory period (see also page 25). The transmembrane voltage can
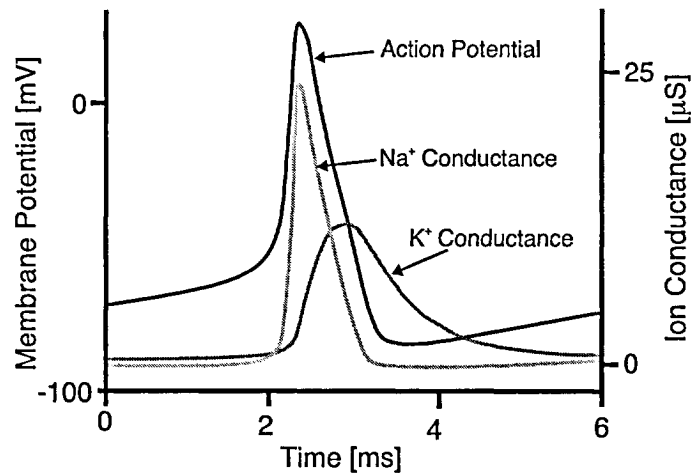
Figure 2.7: Actionpotential of the neuron and the transmembrane ion conductances of K^+ and Na^+, the most important ions involved in the actionpotential generation.

be measured by a microelectrode inserted into the cell, as is described in section 2.2.1. The transient behavior of these voltage-gated ion channels and the generation of the action potential were first described by Hodgkin and Huxley examining the giant squid axon [1].

The Hodgkin-Huxley Model

Most biological membranes, and especially, excitable membranes have a nonlinear I-V relation. The best studied model for the mechanisms in excitable membranes is the squid giant axon, and the analytical tool is the *gate model* of Hodgkin and Huxley. This model will be briefly introduced here, for more information the interested reader is directed to numerous books, such as [70] or the original paper [1].

Figure 2.8: Hodgkin-Huxley model of the squid axon. g_K and g_{Na} are voltage- and time-dependent, and g_L is constant. The total membrane current is described by equation 2.3.

Table 2.1: Important parameters of the Hodgkin-Huxley model of the squid axon.

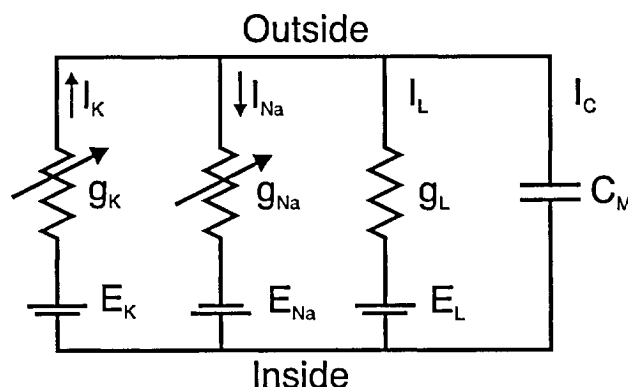| Parameter	Description	Value
g_{Na^+}	Na$^+$ channel conductance	12 S/m^2
g_{K^+}	K$^+$ channel conductance	3.6 S/m^2
g_L	Leakage channel conductance	0.5 S/m^2
C_M	Membrane capacitance	100 fF/μm^2
E_{Na^+}	Na$^+$ equilibrium potential	45 mV
E_{K^+}	K$^+$ equilibrium potential	-82 mV
E_L	Leakage equilibrium potential	-70 mV

Hodgkin and Huxley used the model shown in Figure 2.8 to describe the major ionic currents. The sodium and potassium currents flow through specific channels, whose conductance values are time- and voltage-dependent, whereas the value of the leakage ion conductance is considered constant. Hodgkin and Huxley analyzed the behavior of these channels using the patch-clamp method (section 2.2.1) and summarized their extensive experimental studies on the giant axon of the squid in four differential equations. A first and fundamental equation describes the conservation of electric currents.

$$I_M = C_M \frac{dV_M}{dt} + \bar{g}_K n^4 (V - E_K) + \bar{g}_{Na} m^3 h (V - E_{Na}) + g_L (V - E_L) \qquad (2.3)$$

I_M represents the total membrane current, and V is the voltage across the membrane. The K-channel state, e.g., is described by a maximum channel conduc-

tance $\overline{g}_K$ and a gate variable n which describes the voltage- and time-dependence of the channel. The variables used in equation 2.3 are described in table 2.1 and equation 2.4. Then, there are three more differential equations (equation 2.4), which describe the dynamics of the gate variables n, m, h and, therefore, the opening and closing of Na^+ and K^+ion channels.

$$\frac{dm}{dt} = \alpha_m(1-m) - \beta_m m$$

$$\frac{dh}{dt} = \alpha_h(1-h) - \beta_h h$$

$$\frac{dn}{dt} = \alpha_n(1-n) - \beta_n n \qquad (2.4)$$

These variables describe the reaction between open and closed state of the channels and are first-order reactions, which is a basic assumption of the model. The functions n, m, h transform then to power functions, as for example n^4 in equation 2.3, when more than one identical gating particle is involved in the channel activation (four in this example). n and m open the channel when the membrane depolarizes, h closes the channel. The set of equations is complete with the so-called kinetic parameters α and β in equation 2.5.

$$\alpha_n(V) = 0.01(-V+10)/(e^{\frac{-V+10}{10}} - 1)$$

$$\beta_n(V) = 0.125 e^{\frac{-V}{80}}$$

$$\alpha_m(V) = 0.1(-V+25)/(e^{\frac{-V+25}{10}} - 1)$$

$$\beta_m(V) = 4 e^{\frac{-V}{18}}$$

$$\alpha_h(V) = 0.07 e^{\frac{-V}{20}}$$

$$\beta_h(V) = 1/(e^{\frac{-V}{18}} + 1) \qquad (2.5)$$

These are empirical terms, which fit the measurements obtained by Hodgkin and Huxley with the patch clamp method. Using numerical methods, Hodgkin and Huxley solved equation 2.3 and obtained remarkable fit quality of the recorded and the calculated action potentials.

Unidirectional Propagation of the Action Potential

Voltage-gated Na^+ channels remain inactive for several milliseconds after opening, this time span is called the refractory period. The spread of the ions is
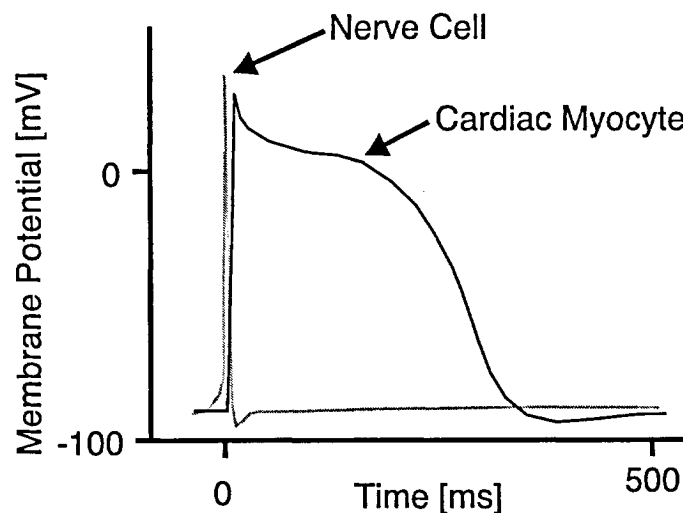
Figure 2.9: Cardiac and neural action potential. A cardiac action potential typically lasts about 300 ms, whereas a neural action potential lasts 2 to 4 ms. Note, that these values can significantly change for different cells from different animals.

passive, when membrane depolarization takes place at a node of Ranvier, and, therefore, ions spread in both directions along the axon. But, the Na^+ channels immediately behind the action potential cannot reopen even though the potential in this segment is depolarized due to this passive spread. The inability of Na^+ channels to re-open during the refractory period ensures that action potentials are propagated unidirectionally from the soma to the axon terminal, and limits the number of action potentials per second that a neuron can conduct.

2.1.3 The Cardiac Action Potential

There are two general types of cardiac action potentials, those originating from non-pacemaker cells and those from pacemaker cells. Non-pacemaker action potentials, also called "fast-response" action potentials because of their rapid depolarization, are found throughout the heart. The pacemaker cells generate spontaneous action potentials that are also termed "slow-response" action potentials because of their slower rate of depolarization. These are found in the sinoatrial and atrioventricular nodes of the heart.

Both types of action potentials in the heart differ considerably from action potentials found in neural cells or skeletal muscle cells. One major difference is in the duration of the action potentials. In a typical nerve, the action potential duration is about 1 ms. In skeletal muscle cells, the action potential duration

is approximately 2-5 ms. In contrast, the duration of a cardiac action potential ranges from 200 to 400 ms (see Figure 2.9). Another difference between cardiac, nerve and muscle action potentials is the role of calcium ions during depolarization. In nerve and muscle cells, the depolarization phase of the action potential is caused by an opening of sodium channels. This also occurs in non-pacemaker cardiac cells. However, in cardiac pacemaker cells, calcium ions are involved in the initial depolarization phase of the action potential.

Unlike pacemaker cells, *non-pacemaker cells* have a true resting membrane potential (phase 4, Figure 2.10 A) that remains near to the equilibrium potential for K^+ (E_K). When these cells are rapidly depolarized to a threshold voltage of about -70 mV (e.g., by another conducted action potential), there is a rapid depolarization (phase 0) that is caused by a transient increase in fast Na^+-channel conductance. At the same time, the K^+ conductance (g_K) falls. These two conductance changes move the membrane potential away from E_{Rest} and closer toward E_{Na}. Phase 1 represents an initial repolarization that is caused by the opening of a special type of K^+ channel (not shown in the Figure). However, because of the large increase in slow inward Ca^{++} current, the repolarization is delayed and there is a plateau phase in the action potential (phase 2). This inward calcium movement is through long-lasting (L-type) calcium channels that open up when the membrane potential depolarizes to about -40 mV. Repolarization (phase 3) occurs when g_K increases and g_{Ca} decreases. Therefore, the action potential in non-pacemaker cells is primarily determined by changes in fast Na^+, slow Ca^{++} and K^+ conductances. During phases 0, 1, 2, and a part of phase 3, the cell is refractory to the initiation of new action potentials. During this refractory period, stimulation of the cell does not produce new, propagating action potentials.

Pacemaker cells are characterized as having no true resting potential, but instead generate regular, spontaneous action potentials. Unlike most other cells that elicit action potentials (e.g., nerve cells, muscle cells), the depolarizing current is carried primarily by relatively slow, inward Ca^{++} currents instead of by fast Na^+ currents (as illustrated in Figure 2.10 B and C). There are, in fact, no fast Na^+ currents operating in pacemaker cells. At phase 0 the depolarization is primarily due to increased g_{Ca}. Because the movement (or conductance) of Ca^{++} through the channels is not rapid (hence, the term "slow inward Ca^{++} channels"), the rate of depolarization (slope of Phase 0) is much slower than found in other cardiac cells. Repolarization occurs (Phase 3) as g_K increases and g_{Ca} decreases. Spontaneous depolarization (Phase 4) is due to a fall in g_K and a small increase in g_{Ca}. A slow inward Na^+ current also contributes to Phase 4, and is thought to be responsible for what is termed the pacemaker
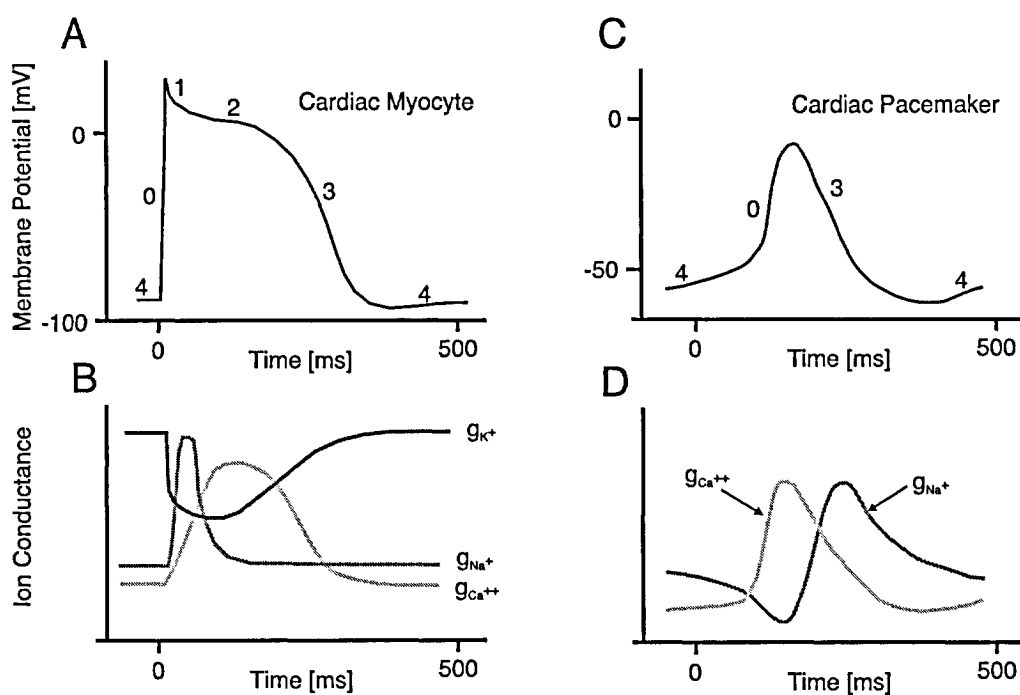
Figure 2.10: Cardiac action potential with associated channel conductances (left). Action potential of cardiac pacemaker cells and their channel conductances (right).

or "funny" current (I_F). Once this spontaneous depolarization reaches threshold (about -40 mV), a new action potential is triggered. Although pacemaker activity is spontaneously generated, the rate of this activity can be modified significantly by external factors such as autonomic nerves, hormones, ions, and ischemia/hypoxia.

Arrhythmia

The rhythm of the heart is normally generated and regulated by pacemaker cells within the sinoatrial (SA) node, which is located within the wall of the right atrium. SA nodal pacemaker activity normally governs the rhythm of the atria and ventricles. When this rhythm becomes irregular, too fast (tachycardia) or too slow (bradycardia), or the frequency of the atrial and ventricular beats are different, then this is called an arrhythmia. Arrhythmias can develop from either altered impulse formation or altered impulse conduction. The former concerns changes in rhythm that are caused by changes in the automaticity of the pacemaker cells or by abnormal generation of action potentials at sites other than the SA node. Altered impulse conduction is usually associated with a complete or partial block of electrical conduction within the heart. Altered impulse conduction commonly results in reentry, which can lead to tachyarrhythmias. Many origins of arrhythmia, e.g. QT-prolongation [11], can be observed in cell cultures, this opens a large field of applications for MEAs in the pharmaceutical industry.

2.2 Recording of the Action Potential

The action potential of an electrogenic cell can eighter be measured using fluorescence methods, e.g., voltage sensitive dyes, or directly using electrical recording techniques. Standard tools that electrically measure the activity of electrogenic cells are based on two different techniques: transmembrane measurements of the action potential using the patch-clamp technique and extracellular recordings by planar microelectrodes.

2.2.1 Patch Clamp

The patch-clamp technique [76] yields high-accuracy information about the electrophysiological properties of the cell and, indeed, played a key role in un-
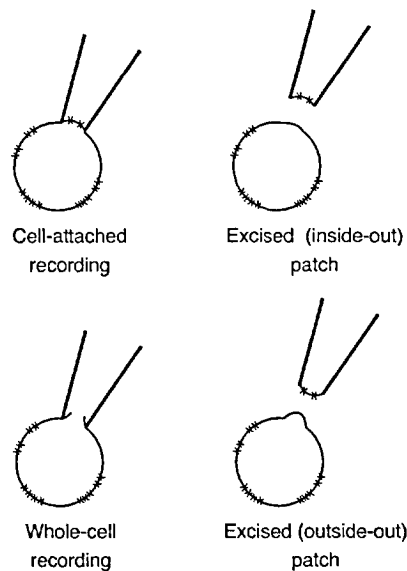
Figure 2.11: Configurations of patch clamping. (Adapted from [70])

derstanding the underlying mechanisms of the action potential. The recording from entire cells, or alternatively currents flowing through single ion-channels, can be measured. It is an invasive method; a glass pipette is used as an electrode to penetrate the cell membrane thereby gaining access to the intracellular medium. While this method is rich in information it is limited by the number of cells that can be simultaneously monitored and by short-term cell viability (of usually hours). The various configurations of patch clamping are given in Figure 2.11. The four recording configurations are: cell-attached, whole-cell recording, outside-out patch, and inside-out patch. The upper left diagram is the configuration of a pipette in simple mechanical contact with a cell, as used for single-channel recording [76]. With slight suction, the seal between the membrane and the pipette increases in resistance forming a cell-attached patch. This leads to two different cell-free recording configurations (outside-out and inside-out patches).

Voltage-clamp currents from whole cells can be recorded after disruption and penetration of the patch membrane. Voltage-clamp experiments usually involve inserting two electrodes [77] into the cell or axon, one for recording the transmembrane voltage and the other for passing current into the axon to keep the transmembrane voltage constant (or clamped). The main advantages of voltage-clamping the membrane are: By keeping the voltage constant, one can eliminate the capacitive current and one can measure the time-dependence of ion conductance without the influence of voltage-dependent parameters (such as voltage gated ion channels).
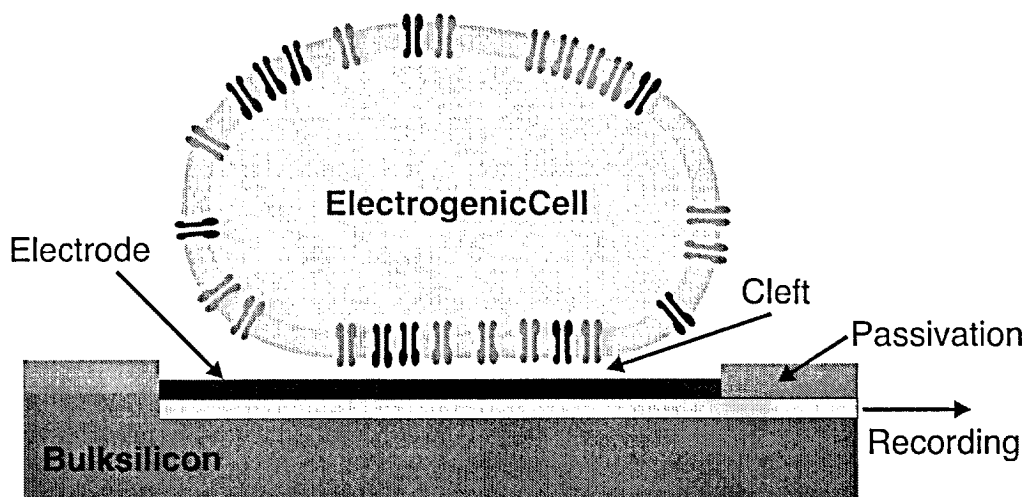
Figure 2.12: Electrogenic cell on an electrode. An equivalent circuit model for this configuration is given in section 3.2.

2.2.2 Extracellular Recording of the Action Potential

Recording electrical oscillations in the brain began in 1875, when Richard Caton discovered that currents could be recorded from deep inside the brain [78]. First extracellular recordings using an MEA dates back to the 1970s [79, 80]. The functional principle of extracellular recordings of a cell attached to an electrode is briefly described here. More details on the modeling of extracellularly recorded action potentials will be given in chapter 3.

For extracellular recordings, cells are cultured directly on top of a transducing element, which is generally either a metallic electrode [2] or an open-gate transistor [7]. When an action potential occurs in a cell, the local flow of ions in and out of the cell causes the membrane to become non-uniformly polarized (see Figure 2.12). This establishes an electric field, which induces electrical charge in the underlying transducer. It is this charge that leads to the recorded signal. Extracellular recordings have several advantages over patch- and voltage-clamping such as non-invasiveness, which facilitates long measurement periods (months), and multi-site measurement capabilities.

The magnitude of this extracellular signal depends on the membrane currents and on the cleft resistance (Figure 2.12). The transmembrane currents depend on type and number of contributing ion channels, which are a function of the size of the cell and of the spatial distribution of the ion channels. The cleft resistance is a function of the contact area, of the thickness of the cleft, and of the resistance of the electrolyte. The transmembrane peak-to-peak value of an

action potential is about 100 mV. The action potential-induced cleft voltage is in the order of 100 μV to 5 mV, which is also the signal that can be measured on the electrode. Further investigation on the modeling of the cell-electrode system is given in chapter 3.

Electrode Impedance

Metal electrodes are widely in use in biological and medical research. They have specific advantages over glass microelectrodes for the recording of rapid signals, as their high-frequency impedance is low. However, they are not at all suitable for the measurement of dc-potentials [81]. The impedance of the microelectrode is an important parameter for extracellular recording, since it determines the noise of the electrode and the signal attenuation. The impedance and the noise level of a microelectrode is in first order inversively proportional to its area (chapter 3). Therfore, area-increasing methods and special materials are used to reduce the impedance, e.g., Pt-black [14,26] and section 4.2.1, TiN [53], ITO [2], Palladium [54], TiN or IrO [82]. Further details and the modeling of the phenomenas at the electrode-electrolyte interface and measurements are given in chapter 3.

Chapter 3

Characterization of the Neuron-Electrode Interface

In this chapter, the characteristics of the neuron-electrode interface are analyzed by means of equivalent circuit modeling. First, a model of the electrode impedance is given, and parameters are extracted from measurements. The noise spectral density of the electrode-electrolyte interface is also measured and analyzed. The electrode exhibits very large offsets and measurements indicate that this offset is influenced by the switch, which connects the stimulation circuitry to the electrode. In the second part a neuron-electrode model will be introduced. The model predicts signals with a peak-to-peak amplitude of around 200 μV, which coincides with measurements and simulations reported in the literature [68, 83–85]. A sensitivity analysis gives a qualitative insight on how the model parameters influence the neuron-electrode transfer function and thus the extracellularly measured signal.

3.1 Electrode Characterization

This section is focused on the main characteristics of the electrode-electrolyte interface: Impedance, noise and electrode offset. These characteristics have been considered for the design of the readout and stimulation circuitry.

3.1.1 Electrode-Electrolyte Interface

Two types of processes can occur at electrode-electrolyte interfaces. One of them comprises reactions, in which charged particles such as electrons cannot

33

pass the interface barrier. These interfaces, generally called *non-faradaic*, do not feature any charge-transfer reaction since such processes are thermodynamically unfavorable. In the non-faradaic case the electrode is typically highly polarized and behaves almost as an ideal capacitor. The second type of electrode is called faradaic. For any electrode-electrolyte interface there is a range of potentials, in which charged particles such as electrons are able to pass across the interface. Charge transfer typically implies oxidation or reduction.

Pt-electrodes in physiological saline are generally modeled using both faradaic and non-faradaic processes. Figure 3.1 shows the commonly used equivalent-circuit model for the electrode-electrolyte interface [86–88]. The model consists of a constant-phase-angle impedance, Z_{CPA}, a charge-transfer resistance, R_{CT}, the Warburg impedance, Z_W, and a serial resistance, R_S. These elements will be introduced now.

The immersion of a metal in an electrolyte results in the formation of space charge layers near the electrode. These layers form a capacitance, since they store charge. One layer of charge is located at the metal surface and consists of water-molecules (hydration sheath), it is termed, the "Inner Helmholtz-Plane". The second layer of opposite charge, in this case the counter ions and their hydration sphere, is located just inside the electrolyte, it is termed the "Outer Helmholtz-Plane" [86, 89, 90]. The value of the capacitance can be approximated by $C_H = \varepsilon A/d$, where ε is the permittivity of the medium (for example water ε=78.5), A is the electrode area and d the distance between the planes. Assuming a distance of 0.5 nm, we get a capacitance of 0.11 F/m^2. A more accurate model can be derived, if the distribution of charge within a certain distance from the electrode is taken into account, as it is done in the Gouy-Chapman model [88–90].

Using a constant-phase-angle impedance, Z_{CPA}, instead of a capacitance results in a better agreement of the model with the measurements [87, 91, 92]. The empirical non-faradaic constant phase-angle-impedance is given by: $Z_{CPA} = K \cdot (I\omega)^{-\beta}$ where K is a measure of the magnitude and β is a measure of the deviation from purely capacitive behavior (β=1). Typically, β is between 0.7 and 0.9. The two most likely causes for the observed frequency dependence of Z_{CPA} are specific adsorption and surface roughness effects [87, 90].

R_{CT} is the charge transfer resistance and can be be derived by a linearization of the Butler-Volmer equation

$$I = j_0(e^{(1-\alpha)f\eta} - e^{\alpha f\eta}), \tag{3.1}$$

where j_0 is the exchange current density, α the charge-transfer coefficient, f
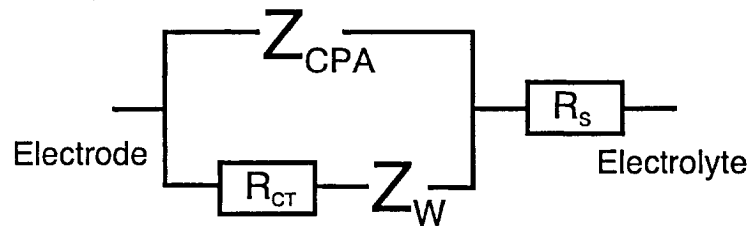
Figure 3.1: Commonly used equivalent circuit model of a noble-metal electrode in solution.

is a constant and η the overpotential. For small voltages such as extracellular potentials, equation 3.1 can be linearized. The resulting current is $I = j_0 f \eta$, and shows ohmic behavior. A typical value for Pt is $j_0 = 7.9 A/m^2$ and $f = F/RT = 37.43$ at room temperature [89]. The corresponding charge-transfer resistance is 3.75 MΩ for a microelectrode of 30x30 μm^2 area. Measured values are about 100 MΩ (see Table 3.2), which is orders of magnitudes larger. Possible reasons will be discussed in the measurement section 3.1.2 below.

The Warburg impedance, denoted Z_W, takes into account that ions, produced on the surface of the electrode, need to diffuse away. This impedance is negligible for frequencies higher than 1 Hz and for large charge-transfer resistances, which produce only small faradaic currents [87]. The charge-transfer resistance is, in our case, larger than 100 $M\Omega$, and the interface impedance is well modeled neglecting Z_W.

R_S is the electrical resistance between the electrode and counter electrode. Without cells on top of the electrode, R_S is given by the spreading resistance, the resistance encountered by a current spreading from the electrode out into the solution. For square-shape electrodes the spreading resistance is given by:

$$R_{Spread} = \frac{\rho \ln 4}{\pi l} \qquad (3.2)$$

where ρ is the solution resistivity (72 Ωcm for physiological saline [93]), and l is the electrode side length. R_{Spread} is only depending on the geometric electrode area, whereas C_E and R_{CT} depend on the total area. The geometric area of the electrode is defined by the electrode geometry and given by the electrode processing. The total area is computed by integrating the exposed surface with all its undulations and asperities. The total area is, of course, always larger than the geometric area. Cell growth might significantly increase R_S, since the carpet of cells seals the electrode from the environment. This topic will be addressed in the following section.

3.1.2   Impedance, Noise and Offset Measurements

Electrode Processing

The electrodes used in these measurements were produced in-house according to the following procedure. A bare p-type Si wafer was electrically isolated with 100 nm SiO_2 followed by 500 nm of Si_3N_4 deposited using plasma-enhanced chemical vapor deposition (PECVD). Sputter deposition was used to coat the substrate with 50 nm of TiW, an adhesion promoter, followed by 200 nm of Pt. The microelectrodes with leads and bond pads were structured in a lift-off process. The wafer was passivated with 500 nm Si_3N_4. A reactive-ion etch (RIE) was used to open the electrodes, thereby defining their size and shape.

Each chip comprises a counter electrode and four pairs of square electrodes of the sizes of 10x10 μm^2, 40x40 μm^2, 70x70 μm^2 and 90x90 μm^2. The size of the counter electrode is 2 mm^2 and is large in comparison to the measurement electrodes. One electrode of each pair and also the counter electrode were covered with Pt-black resulting in a chip comprising eight different microelectrodes for impedance and noise tests. The Pt-black was electrochemically deposited on the electrode using a current density of 0.25 $nA/\mu m^2$ in a solution containing 7 mM hexachloroplatinic acid, 0.3 mM lead acetate and hydrochloric acid to adjust the solution pH to 1.0. The wafer was then diced and cleaned. The bond wires of the packaged chips were encapsulated in a medical epoxy (EPOTEK 353 ND) for electrical isolation.

Measurement Setup

Impedance and noise measurements of bright-Pt and Pt-black electrodes of different sizes have been performed. The impedance-measurement setup is depicted in Figure 3.2A. The counter electrode is modulated using a 60 mV_{PP} sine wave from the output of a dynamic signal analyzer (HP 3562A). The resulting current through the microelectrode is then sensed by a low-impedance input using an opamp with a resistor in the feedback. An opamp (AD8627) with junction field-effect transistor (JFET) inputs has been used, JFETs have a very small input biasing current, which is necessary to detect currents below 1 nA. The signal is further amplified by a differential amplifier (Tektronics AM502) and then fed back to the dynamic signal analyzer. The impedance can be calculated from the measured spectrum using the following equation:
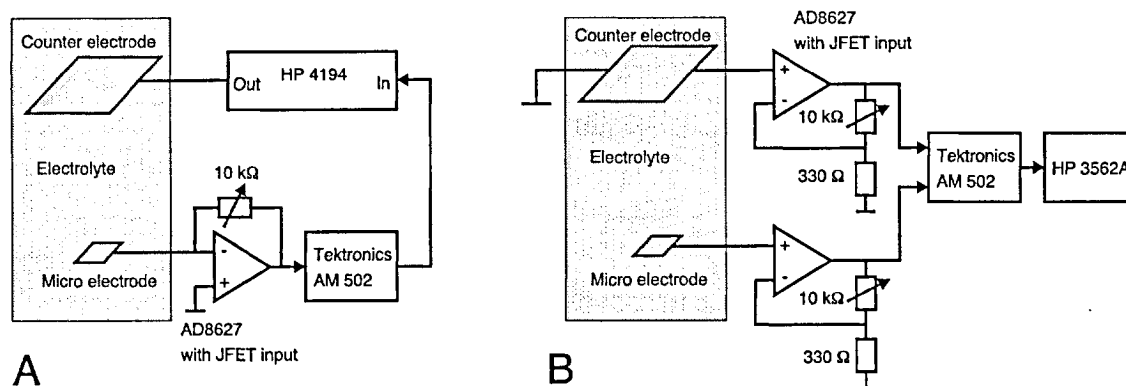
Figure 3.2: Measurement setup for (A) the impedance and (B) the noise measurements. An amplifier with low-noise, high-impedance inputs is required in both cases, so that an operational amplifier with JFET input transistors has been chosen.

$$Z = R \cdot gain \cdot \left(\frac{V_{In}}{V_{Out}} \right)^{-1}$$

R is the resistance used in the feedback of the opamp, *gain* is the amplification factor of the Tektronics amplifier, and V_{in}/V_{out} is the measurement result from the dynamic signal analyzer.

The noise measurements have been performed using the setup shown in Figure 3.2B. The electrode is directly connected to the high-impedance input of the opamp. The same opamp AD8627 with JFET inputs has been used since JFETs exhibit smaller low-frequency noise than MOSFETs. A resistive divider in the feedback of the opamp amplifies the signal. The signal is then AC-coupled with a cut-off frequency at 0.1 Hz and is further amplified by the Tektronics amplifier. The AC-coupling is filtered out in the data post-processing. A total amplification of 10'000 has been chosen for these measurements. The spectral information is then recorded using a dynamic signal analyzer (HP 3562A). The whole measurement path is differential in order to suppress distortion and especially to suppress 50 Hz signals. Furthermore, the measurement has been performed in a Faraday cage.

Impedance Measurements

The impedance modulus of the blank-Pt and the Pt-black electrodes are presented in Figure 3.3, the fitted parameter values are given in Table 3.1. Blank-Pt electrodes show a plateau at lower frequencies, this plateau originates from

the charge-transfer resistance, R_{CT}. The current in this region is dominated by faradaic currents, which can be seen in the phase in Figure 3.4. The phase goes towards zero with decreasing frequency, therefore the interface behaves as a resistor. Pt-black electrodes would also show this plateau, but measurements below 10 mHz are needed to clearly see this. The value of R_{CT} is in the range of 0.5 to 1 GΩ and is much larger than the 3.75 MΩ arising from a typical value of 7.9 A/m^2 [89] for the exchange current density. The reason may be as follows. Typical R_{CT} values are based on the standard hydrogen electrode, where the Pt is surrounded by bubbles of hydrogen, which allows oxidation and reduction of hydrogen on the Pt. Franks et al. propose that for Pt electrodes in physiological saline the oxidation of hydrogen is favored over a redox reaction due to a shift in the open-circuit potential of the Pt-electrodes compared to a standard hydrogen electrode [88]. The resulting exchange current density is very small due to the limited amount of hydrogen gas available in the solution. It is assumed that the O_2 redox reaction and charge transfer via contaminations at the interface are mainly responsible for the faradaic current.

The constant-phase angle impedance Z_{CPA}, causes the roll-off of the impedance. The measured values for bright-Pt correspond to a capacitance per area of about 2 - 5 F/m^2. For Pt-black the capacitance is about 150 - 300 F/m^2, which is roughly 100 times larger than for bright-Pt. Similar values can be found in the literature [51, 94]. It is worth noting that not only the total area but also the geometric area of the electrode grows during platinization by a mushroom-like outgrowth. Especially small electrodes can be significantly larger after this process. The magnitude β of Z_{CPA} is between 0.87 and 0.92. The β-values of the bright-Pt are slightly larger in average than the β-values of Pt-black, bright-Pt therefore behaves somewhat more like a capacitor. The phase is about - 80 degrees, which is close to capacitive behavior of the electrode. At higher frequencies the series resistance, R_S, starts dominating the impedance, and the phase returns to zero, as illustrated in Figure 3.4 in the lower graph. R_S is inversely proportional to the side length of the electrode, when no cells are grown on top [93], which is well supported by the measurements.

All absolute values presented here have to be handled with care, since it is well known that these values can drastically change over time [51, 88].
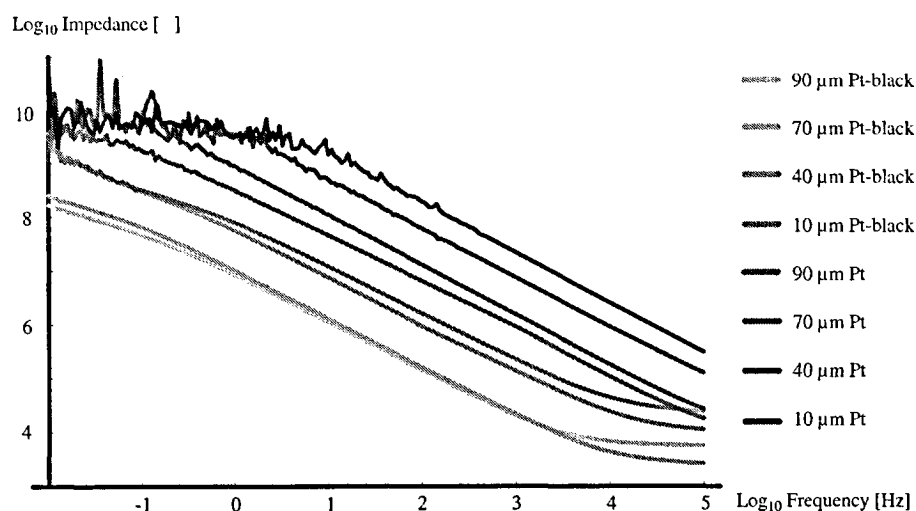
Figure 3.3: *Impedance spectra of blank-Pt and Pt-black electrodes of 10x10 μm² to 100x100 μm² area.*

Electrode	Material	K $[\Omega s^{-\beta}]$	$1/K$	β	R_{CT} $[\Omega]$	R_S $[\Omega]$
10x10 μm²	Pt	$2.2 \cdot 10^9$	$0.45 \cdot 10^{-9}$	0.93	$6.9 \cdot 10^8$	-
40x40 μm²	Pt	$2.4 \cdot 10^8$	$4.1 \cdot 10^{-9}$	0.9	$1.1 \cdot 10^9$	-
70x70 μm²	Pt	$9.3 \cdot 10^7$	$10.7 \cdot 10^{-9}$	0.92	$1.2 \cdot 10^9$	-
90x90 μm²	Pt	$3.3 \cdot 10^7$	$30.3 \cdot 10^{-9}$	0.87	$5.3 \cdot 10^8$	-
10x10 μm²	Pt-black	$9.9 \cdot 10^6$	$101 \cdot 10^{-9}$	0.87	-	2'470
40x40 μm²	Pt-black	$5.9 \cdot 10^6$	$169 \cdot 10^{-9}$	0.9	-	1'144
70x70 μm²	Pt-black	$1.1 \cdot 10^6$	$909 \cdot 10^{-9}$	0.9	-	579
90x90 μm²	Pt-black	$8.8 \cdot 10^5$	$1'140 \cdot 10^{-9}$	0.89	-	266

Table 3.1: *Characteristic parameters of the electrodes which have been extracted from the impedance and noise measurements.*

Noise Measurements

The power spectral density in the frequency range from 100 mHz to 100 kHz has been measured. The resulting noise spectral density for blank-Pt is shown in Figure 3.5. The RMS values of the noise are given in Table 3.2. The measurement included a linear frequency sweep in three different regions, which is the reason for the edges occurring at 10 Hz and 1 kHz. The plots show a
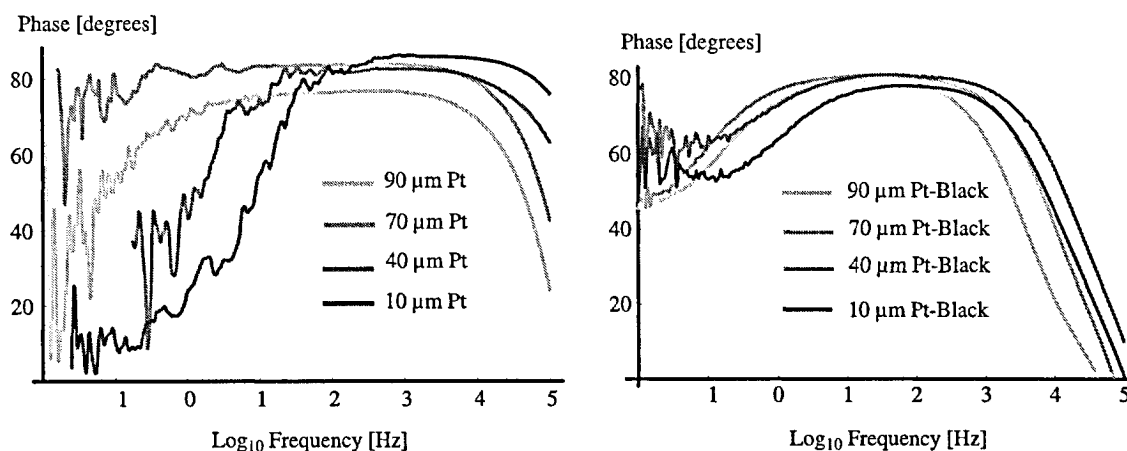
Figure 3.4: Phase spectra of blank-Pt and Pt-black electrodes from 10x10 μm^2 to 100x100 μm^2.

low-frequency plateau with a $1/f^2$ roll-off. The occurrence of this plateau is well known in the literature [95, 96]. The magnitude of the frequency roll-off is given by the operation of the electrode. Hassibi et al. [96] propose that a 20 dB/decade roll-off at observed in diffusion-controlled electrodes, and a 40 dB/decade roll-off at drift-dominated electrodes, which supports the findings in our noise measurements. Our electrodes are highly polarized with a very small amount of faradaic current and are, therefore, certainly not diffusion dominated. The region from 10 Hz to 1 kHz shows a transition from the $1/f^2$ behavior to thermal noise. The thermal noise of all electrodes is rather small as illustrated in Table 3.2. The high-frequency noise above 1 kHz mainly arises from the noise of the JFET amplifier of the measurement setup.

As expected, the noise increases with decreasing size of the electrode, and the noise is smaller for Pt-black electrodes as compared to bright-Pt electrodes of the same geometric area. The results in Table 3.2 and Figure 3.5 illustrate the importance of filtering, when using metal electrodes as transducers. The RMS noise of the electrodes is quite small in the bandwidth of 10 Hz to 100 kHz. The values drastically increase when lower frequencies are included. The large low-frequency noise of small bright-Pt electrodes coincides with the observation that small electrodes show large fluctuations and drift. In contrast, Pt-black electrodes or larger bright-Pt electrodes show a more stable potential when exposed to liquid. Electrodes as large as 1 cm^2 have also been used for material characterization [97, 98], and showed a very stable potential. It is worth mentioning that the noise of the electrodes above 10 Hz is rather small for both cases, for the Pt-black and the bright-Pt electrodes. In conclusion, platinization is necessary for stimulation and for small signal attenuation in recordings, but
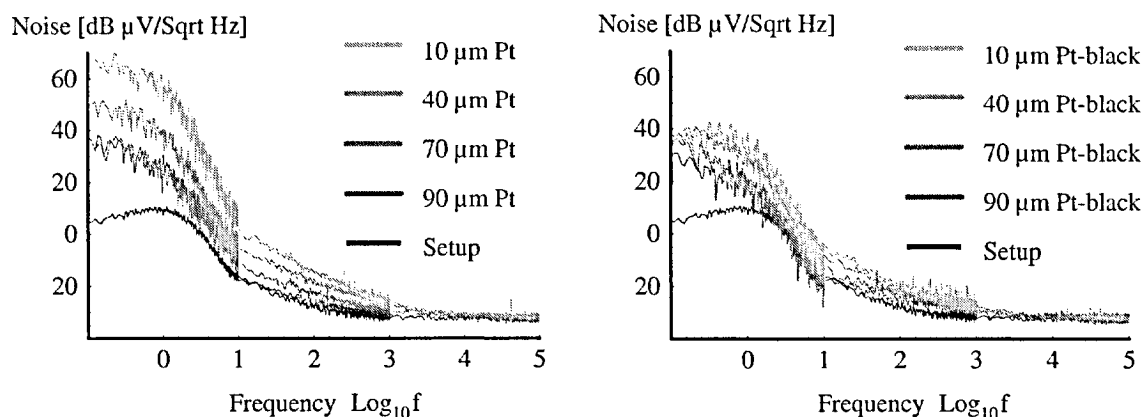
Figure 3.5: Left: noise-spectral density of bright-Pt electrodes. Right: noise-spectral density of Pt-black electrodes. The black curve in both graphs indicates the noise from the measurement setup.

is obviously not needed to improve the noise characteristics. This holds as long as the filtering efficiently suppresses the lower frequency components.

Electrode area	Material	V_{RMS} 100 mHz- 100kHz	V_{RMS} 10 Hz- 100kHz
10x10 μm^2	Pt	1368.5 μV_{RMS}	3.19 μV_{RMS}
40x40 μm^2	Pt	186.1 μV_{RMS}	2.16 μV_{RMS}
70x70 μm^2	Pt	40.8 μV_{RMS}	1.53 μV_{RMS}
90x90 μm^2	Pt	30.3 μV_{RMS}	0.95 μV_{RMS}
10x10 μm^2	Pt-black	-	-
40x40 μm^2	Pt-black	73.0 μV_{RMS}	2.02 μV_{RMS}
70x70 μm^2	Pt-black	18.5 μV_{RMS}	1.91 μV_{RMS}
90x90 μm^2	Pt-black	8.4 μV_{RMS}	1.61 μV_{RMS}

Table 3.2: Characteristic parameters of the electrodes, which have been extracted from the impedance and noise measurements.

Electrode-Offset

A large offset of the electrical potential of the electrode with respect to the counter electrode has been observed. Since both electrodes consist of platinum, a potential difference close to zero phase been expected. However, values of more than 1 V have been measured.

In the design of the MEA128, there are three possibilities for the voltage on the electrode to be altered, as is represented by the arrows in the Figure 3.6. First, electrochemical reactions at the surface can change the electrode potential, this is considered by the current I_{Sol}. Then, there are two leakage paths to the bulk, I_{Gate} and I_{Switch}. I_{Gate} is the leakage current through the input of the first readout stage connected to the electrode. Another leakage path is through the switch that connects the stimulation buffer to the electrode. Even if the switch is open there is a parasitic diode from the source to the bulk, through which the current, I_{Switch}, can flow. In order to measure the effects of these currents three different electrodes of 30 x 30 μm^2 area, have been integrated on a test chip. One electrode is floating, one is connected to a NMOS switch, and the third to a PMOS switch. If the switch influences the electrode potential it is expected that the electrode connected to the NMOS switch has a lower electrical potential than the electrode connected to the PMOS switch. The chip has been operated between 0 and 5 volts and the counter electrode has been fixed to 2.5 V. The floating electrode has been measured at 1.3 ±0.2 V, the electrode connected to the NMOS switch was measured at 0.7 ±0.2 V and the electrode connected to the PMOS switch was at 3.1 ±0.2 V. This is only a coarse measurement, but the result qualitatively shows that the leakage current through the switch has a large influence on the DC potential of the electrodes. The contribution of I_{Gate} should be minor according to the specifications of the CMOS process. It can therefore be assumed that the electrode potential at equilibrium is defined by the two currents I_{Switch} and I_{Sol}.
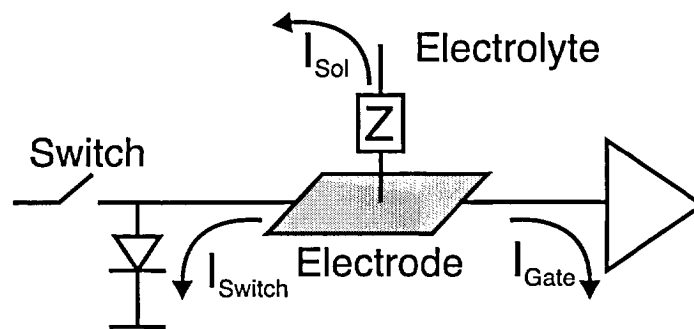

Figure 3.6: Three possible effects, which can define the electrode potential at equilibrium.

3.2   Neuron-Electrode Model

An equivalent-circuit model of the neuron-electrode system is presented in this section. In this model it is assumed that the metal electrode is only partially covered by the electrogenic cell, which results in a capacitive divider, that might attenuate the recorded action potential. The first section gives an overview of the model, and a sensitivity analysis is presented in the second section.

3.2.1   Model Overview

The model presented in this section includes four different parts (see Figure 3.7):

1. the *neuron*, as described by the Hodgkin-Huxley model (equation 2.3)

2. the *cleft* between the cell and the electrode. Good adhesion increases the resistance of the cleft called "sealing resistance", R_{Seal}

3. the *electrode* is analyzed using an equivalent circuit model, which has been simplified in comparison to that of Figure 3.1. Additionally, the electrode area is partially covered by the active cell, and the rest of the area is covered by electrolyte solution or neighboring cells.

4. the resistance between the electrode and the counter electrode

The equivalent-circuit model shown in Figure 3.7 includes the Hodgkin-Huxley model with the ionic currents of the cell, I_K, I_{Na}, I_L and I_C. The currents I_K, I_{Na} represent the transmembrane currents of potassium and sodium. Currents from other ions are summarized in a leakage current I_L, and capacitive currents are represented by I_C. Details on this membrane model are given in section 2.1.2. The potential underneath the cell is termed the cleft potential, V_C, and the potential on the electrode is termed V_{El}. The sealing resistance, R_{Seal}, represents the resistance between the cleft and the surrounding solution. Its value depends on the cell size and on the distance between cell and electrode. Values in the range between 1 MΩ and 10 MΩ can be found in the literature [7,67,99]. If an action potential occurs in the cell, ionic currents flow across the cell membrane. The total current has two possible paths from underneath the cell to the counter electrode. The current either flows through R_{Seal} or through the electrode and produces a voltage drop in the cleft, which can be measured on the electrode (Figure 3.8). The electrode model in Figure 3.1 includes a resistor, R_E, and a
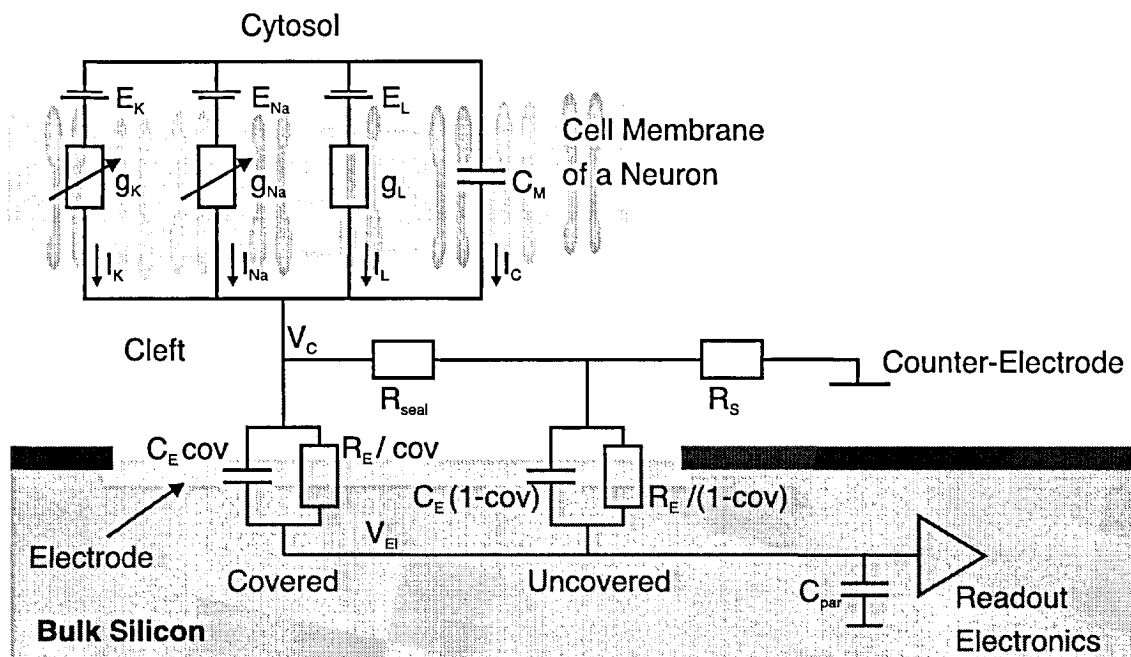
Figure 3.7: Model of the neuron-electrode system. The figure shows a neural cell membrane close to a planar electrode.

capacitor, C_E. R_E is the total charge transfer resistance and C_E is the capacitance of the entire electrode. Default values of 500 MΩ for R_E and 10 nF for C_E are chosen based on the measurement results in Table 3.1.

In many cases, the cell only partly covers the electrode, either because the cell is smaller than the electrode or because it is not centered on the electrode. This has been considered by splitting the electrode into a covered part and an uncovered part using a parameter *cov*. The parameter *cov* equals 1 for an entirely covered electrode and close to 0 for an almost uncovered electrodes. The resulting equations for the covered and the uncovered capacitance and resistance are given in the Figure 3.7. The input capacitance of the first stage is represented by C_{Par}, which includes also parasitic capacitances to the CMOS bulk. This parasitic capacitance C_{Par} leads to an attenuation of the electrode potential of $C_E/(C_{Par} + C_E)$. In our case, C_{Par} can be neglected because it is more than 1000 times smaller than C_E. R_S is the resistance between measuring electrode and counter electrode.

As an example, Figure 3.8 shows a transient simulation of the model. The transmembrane voltage amounts to about 120 mV_{PP}, and the resulting voltage on the electrode is 130 μV_{PP}. The signal shape does not perfectly match the measurements in Figure 5.7. A direct comparison is anyway difficult, since the signal

Amplitude [mV]

Amplitude [µV]
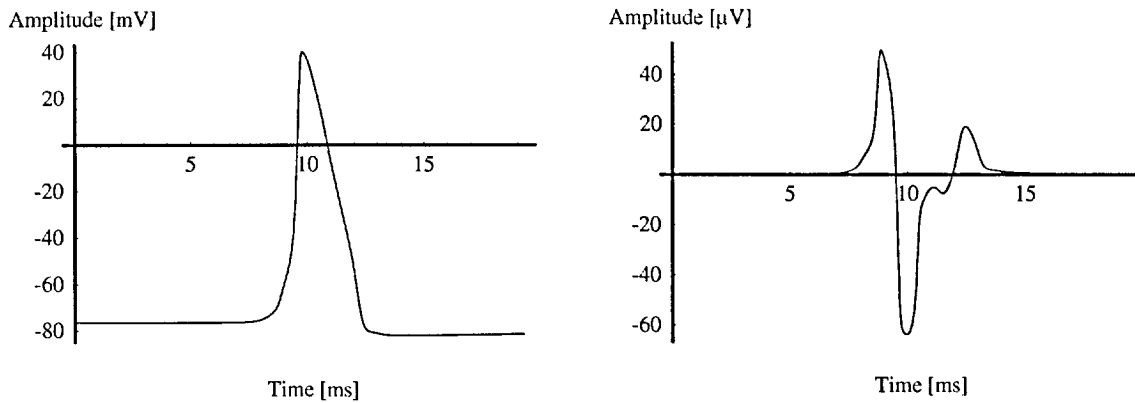
Figure 3.8: Simulation results. Left: Transmembrane voltage (left) from a spice simulation of the Hodgkin-Huxley model and resulting the electrode potential V_{El} (right). The following default parameters were used: $R_E = 500\,M\Omega$, $C_E = 10\,nF$, $C_{Par} = 2\,pF$, $R_{Seal} = 1\,M\Omega$, $R_S = 500\,k\Omega$, $cov = 0.3$, $I_M = 100\,pA$.

shape can drastically change in dependence of the measurement conditions. Additionally, the action potential in the simulations is based on measurements of snail-neuron axons [1, 70] and the measurements in Figure 5.7 are from chicken neurons.

3.2.2 Parameter-Sensitivity Analysis

A sensitivity analysis of the electrode voltage, V_{El}, upon variation of the model parameters is given in this section. The sensitivity analysis is applied to transient simulations using the model in Figure 3.7 and to spectral simulations using the model in Figure 3.9.

Analytical Results

For the spectral analysis, the model described in Figure 3.7 is reduced to the equivalent circuit shown in Figure 3.9. For the reduced equivalent circuit the Hodgkin-Huxley model is replaced by a current source, and C_{Par} is neglected. The voltage on the electrode, V_{El}, can then be described by the following equation:

$$V_{El}[s] = I_M \cdot R_{LF} \cdot \frac{1 - s/z}{1 - s/p} \qquad (3.3)$$
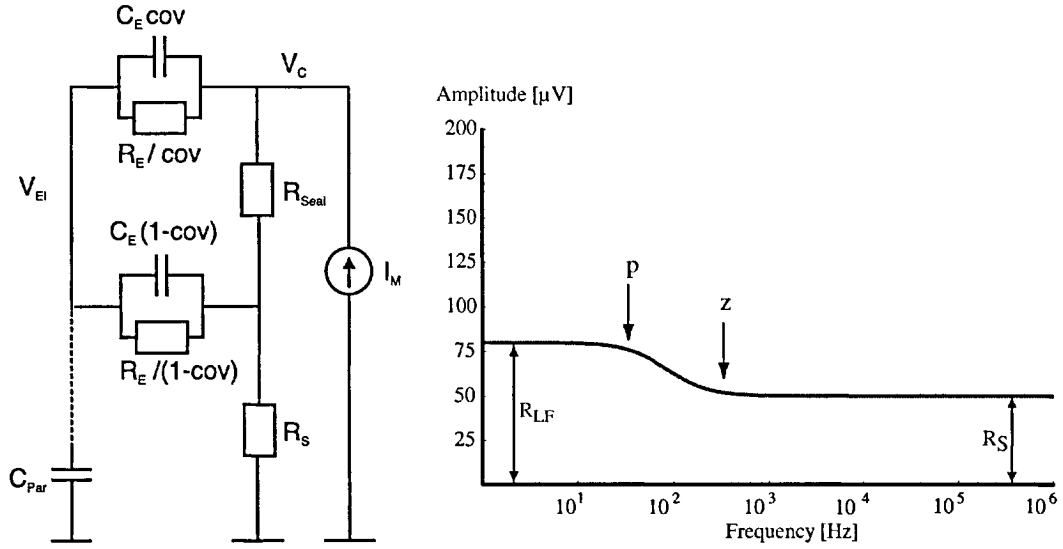
Figure 3.9: Model of the Neuron-Electrode System. $V_{EI}[s]$ has been calculated using the following settings: $R_E = 500\,M\Omega$, $C_E = 10\,nF$, $R_{Seal} = 1\,M\Omega$, $R_S = 500\,k\Omega$, $cov = 0.3$, $I_M = 100\,pA$. A current amplitude of 100 pA has been applied for I_M, which is approximately the transmembrane current flowing in the Hodgkin-Huxley model (10 µm cell diameter).

where R_{LF} is the resistance at low frequencies, z is a zero and p a pole. The function shows one pole at lower frequencies and one zero at higher frequencies. The pole is mainly depending on R_{Seal} and C_E and equals

$$p = \frac{R_E + cov\,R_{Seal} - cov^2 R_{Seal}}{(cov - 1)\,covC_E R_E R_{Seal}} \approx \frac{-1}{(cov - cov^2)\,R_{Seal}C_E}. \qquad (3.4)$$

The equation for the pole reduces to the term on the right side, when we assume that R_E is much larger than R_{Seal} and R_S, which is in line with the measurement results in Table 3.1. The pole heavily depends on the coverage. It shifts to large frequencies when cov is close to 0 or 1 and reaches the lowest frequency for $cov=0.5$. The zero is given by

$$z = \frac{R_E R_S + cov\,R_{Seal}(R_E + R_S) - cov^2 R_{Seal}R_S}{(cov - 1)\,covC_E R_E R_{Seal}R_S}, \qquad (3.5)$$

which can be simplified to

$$z \approx \frac{1}{cov(cov-1)R_{Seal}C_E} + \frac{1}{(cov-1)R_SC_E} \qquad (3.6)$$

using the same approximation. The zero behaves similar as the pole with respect to the parameter cov. The resistance at low frequencies, R_{LF}, is given by

$$
\begin{aligned}
R_{LF} &= \frac{R_ER_S + cov R_{Seal}(R_E + R_S) - cov^2 R_{Seal}R_S}{R_E + cov(1-cov)R_{Seal}} \qquad (3.7) \\
&\approx cov R_{Seal} + R_S,
\end{aligned}
$$

which can be simplified to $cov R_{Seal} + R_S$ using again the approximations mentioned above.

Figure 3.9 shows an example of the electrode potential, V_E, plotted versus frequency using the parameters given in the figure caption. At frequencies below the pole p $V_{El}[s]$ shows a plateau with a value of $I_M \cdot R_{LF}$. A second plateau is observed at frequencies above z. At higher frequencies, the current through R_{Seal} is small, and most of the current flows through the electrode. The signal on the electrode is then only depending on the series resistance, R_S, and given by $V_{El} \approx I_M R_S$.

Simulation Results

A sensitivity analysis of the electrode potential with respect to the variation of the parameters is now given. Four different variables are analyzed, the coverage cov, the electrode capacitance, C_E, the sealing resistance, R_{Seal}, and the series resistance, R_S. The resulting plots are shown in Figure 3.10. The spectral analysis for each parameter using the circuit in Figure 3.9 is given on the left and the corresponding transient analysis using the circuit in Figure 3.7 is shown on the right side. Starting from the default values given in Figure 3.8, each single parameter is varied and its influence on the electrode potential is analyzed. The black curve in each plot is based on the default values. The curve drawn in light gray corresponds to a value smaller than the default value, the dark-gray curve corresponds to a value larger than the default value. At the end, a few special cases are analyzed in the conclusion.

- Sealing resistance, R_{Seal}: The signal is amplified proportional to R_{Seal} at frequencies below p. Additionally, the pole is shifted to lower frequencies with a larger R_{Seal}. The influence at frequencies above z is small since

most of the current flows through the electrode. The transient simulation shows only small variations, since the signal bandwidth is above p.

- Series resistance R_S: All of the current ejected from the cell flows across R_S. An R_S value in the range of the value of R_{Seal} significantly raises the electrode potential. The influence of R_S also strongly depends on C_E and on cov.

- Electrode capacitance C_E: The limit for very large C_E leads to $V_{El} = I_M R_S$. In this case most of the current flows through the electrode, thus, the signal V_{El} gets smaller with increasing C_E. If the capacitance C_E is small, the electrode impedance increases, and the voltage drop is larger. Therefore, a smaller C_E is preferred in the case of uncovered electrodes. However,it has to be noted that the noise will also increase.

- Coverage cov: The parameter cov shifts the pole and the zero to higher frequencies when it approaches the value of 1. For a completely covered electrode ($cov \approx 1$), the electrode potential becomes large, and equation 3.3 can be reduced to $V_{El} = I_M (R_{Seal} + R_S)$. The electrode potential just follows the cleft voltage V_C only attenuated by $C_E/(C_E + C_{Par})$. For an incompletely covered electrode (e.g. cov=0.3) V_{El} is attenuated by the capacitive divider formed by the covered and the uncovered part of the electrode. This capacitive divider is defined by $C_{Uncovered}/(C_{Uncovered} + C_{Covered}) = cov$. The attenuation caused by this capacitive divider is equal to the parameter cov. V_{El} is evidently proportional to cov at frequencies below p and independent of cov above z.

Conclusion

A few special cases related to different measurement conditions based on the model results from above are discussed here. Especially, the difference between measuring a single cell as compared to measuring a carpet of cells is discussed.

- Small R_S / low-density cultures: A small R_S occurs when a single cell is on the electrode, and when the uncovered part of the electrode directly interfaces with the liquid medium. Two different situations can occur depending on C_E. If C_E is large, e.g., a Pt-black electrode, then the current flows mainly through the electrode and through R_S. The total impedance is approximately given by $\frac{1}{cov s C_E} + R_S$ and is minute. The total potential
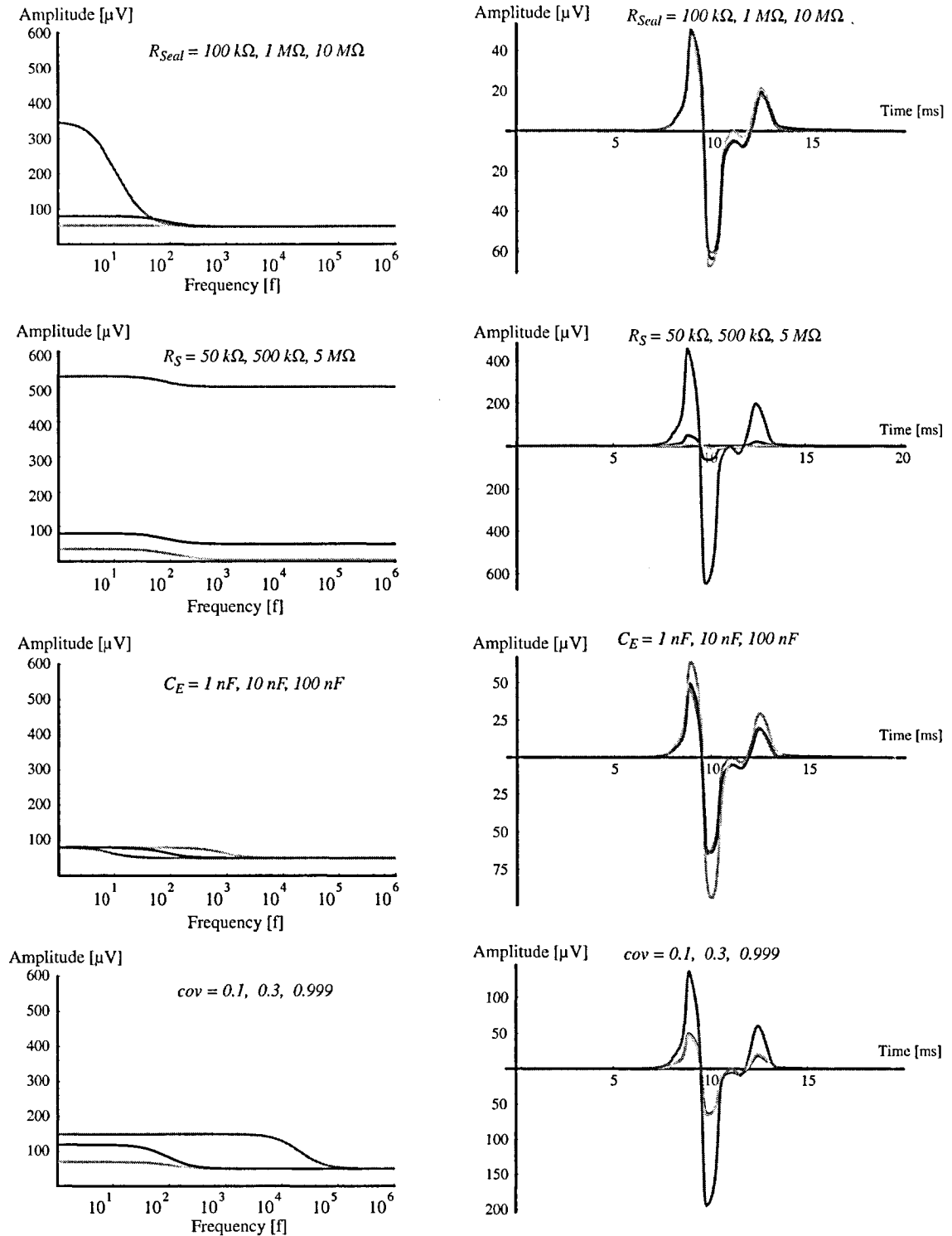
Figure 3.10: Sensitivity Analysis. The spectral analysis for each parameter is given on the left, and the corresponding transient analysis is shown on the right. Starting from the default values ($R_E = 500\,M\Omega$, $C_E = 10\,nF$, $R_{Seal} = 1\,M\Omega$, $R_S = 500\,k\Omega$, $cov = 0.3$, $I_M = 100\,pA$) each single parameter has been varied. The black curve in each plot represents the simulation results applying the default values. A smaller parameter value yields the light-gray curve and a larger value the dark-gray curve in each plot.

drop, and also V_{El} are therefore very small. It will be difficult to measure in this situation, except when the electrode is entirely covered by the cell. Secondly, when C_E is small, e.g. a small bright-Pt electrode or an open-gate FET (OGFET), then low-frequency signals flow through R_{Seal}, and high-frequency signals through the electrode. This entails that for lower-frequency signals the electrode potential is proportional to R_{Seal}, and for higher-frequency signals it is proportional to *cov*. The factor *cov* originates from the capacitive divider formed by the covered and the uncovered part of the electrode. In conclusion, for measurements from single cells a small C_E is favored. For example Fromherz et al. published many measurements from single cells on OGFETs [7,58]. OGFETs have smaller electrode-electrolyte capacitance than noble-metal electrodes. A low-impedance electrode can only be used if the cell is centered on the electrode and if it is assured that the electrode is completely covered.

- Large R_S / high-density cultures: A large R_S occurs when a carpet of cells lies on the electrode array. Even when the active cell does not cover an electrode entirely, neighboring cells and probably also glia cells seal the electrode. In this case the value of R_S is close to the value of R_{Seal}. The effect of the electrode capacitance C_E on V_{El} is small. A large capacitance might be favored because of the smaller noise and drift (see Table 3.2), which improves the signal to noise ratio.

Chapter 4

Monolithic CMOS MEA

The design considerations and the implementation of a CMOS MEA comprising 128 stimulation and recording electrodes (here termed as MEA128) are described in this chapter. The chip was fabricated in an industrial 0.6 µm CMOS process at XFAB, Germany. The monolithic system includes all necessary control circuitry and on-chip A/D and D/A converters. Stimulation signals of 8 bits resolution can be sent to any subset of electrodes at a sampling rate of 60 kHz, while all electrodes of the chip are continuously sampled at a rate of 20 kHz. Circuitry and system simulations and layouts have been realized using Cadence[1] design tools.

After a short system overview, a description of the complete system is given in section 4.1. Post-processing and packaging are then discussed in section 4.2. Die packaging is one of the most challenging and time consuming issues related to the integration of CMOS with biology. Further discussed in this chapter is a precursor design (termed as MEA16) of the MEA128, which comprises 16 bidirectional electrodes (section 4.3), and, finally, a discussion on possible improvements and future designs is given in the last section 4.4. The basic idea of the sections 4.3 and 4.4 is to summarize the main problems and workarounds found with the MEA128 and the precursor system MEA16.

System Overview

Fig 4.1 shows a micrograph of the monolithic CMOS microsystem. The 6.5 mm by 6.5 mm chip comprises 128 stimulation and recording-capable electrodes in
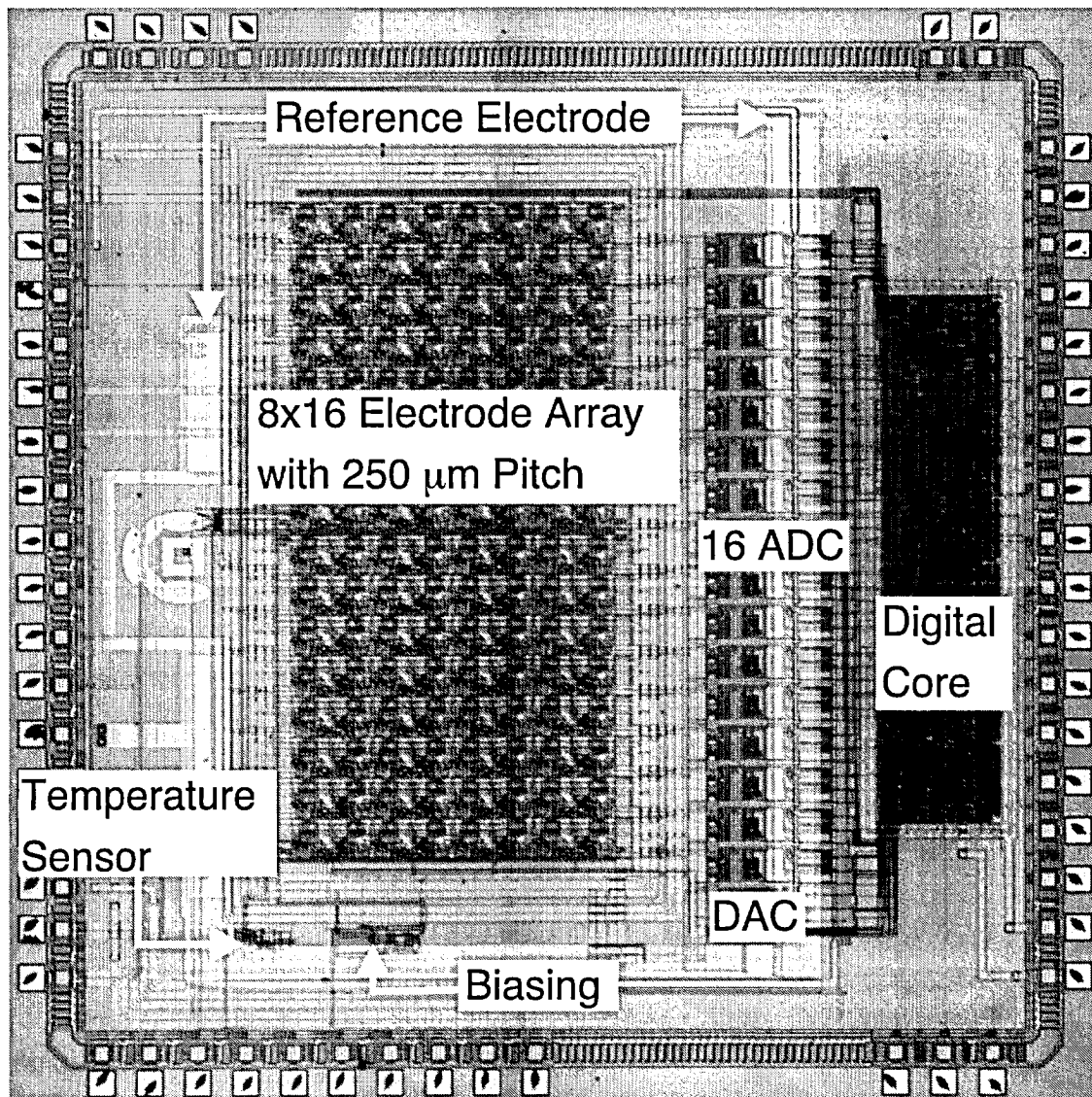
---

[1]Cadence Design Systems Inc., www.cadence.com.

Reference Electrode

8x16 Electrode Array
with 250 μm Pitch

16 ADC

Digital
Core

DAC

Temperature
Sensor

Biasing

Figure 4.1: Micrograph of the MEA128

Table 4.1: Summary of Device Characteristics of the MEA128.

Parameter	Value
Supply Voltage	5 V
Power Consumption	120 mW
Chip Size	6.5x6.5 mm^2
Process	0.6 μm CMOS with double poly, 3 metals, highly-resistive polysilicon
Number of Electrodes	128
Pixel-Pitch	250 μm
Electrode Sampling Rate	20'000 1/s
Data Rate (In)	0.4 MB/s
Data Rate (Out)	3.2 MB/s
Sensor Area	2x4 mm^2
Electrode Size	(depending on post-processing)
Electrode Pitch	(depending on post-processing)
Amplification	1000 or 3000

an 8x16 array, and an integrated reference electrode. The system is structured in a modular design (Figures 4.1 and 4.2). Each pixel of the micro-electrode array incorporates the signal transducing electrode, a fully differential band-pass filter for immediate signal conditioning, a mode storage and a buffer for stimulation. The pitch of the pixel unit is 250 μm. Electrode pitch, size and shape are very flexible, and the electrode material can be selected from a large variety, since the electrodes are realized during post-processing, as described in section 4.2.1. A digital control unit is integrated on the chip. It controls the multiplexing, the electrode selection for stimulation, the reset of single electrodes, and it contains the successive-approximation registers of the A/D converters and the interfaces to the outside world (see Section 4.1.1). Implementing filters and buffers at each electrode offers important advantages in comparison to other CMOS MEAs published in the literature [12, 13, 19, 44, 63]: (i) The signal is amplified and filtered in close proximity of the electrodes, which makes the design less sensitive to noise and interference picked up along connection lines; (ii) a buffer per electrode renders the stimulation signal independent of the number of activated electrodes; (iii) the high-pass filter removes offset and drift of the biochemical signals and, therefore, the signal can be amplified before it is multiplexed; (vi) the low-pass filter limits the noise bandwidth and works as an anti-aliasing filter for the multiplexing and for the subsequent A/D-conversion.

All in-pixel circuitry components are optimized for low noise and small area.
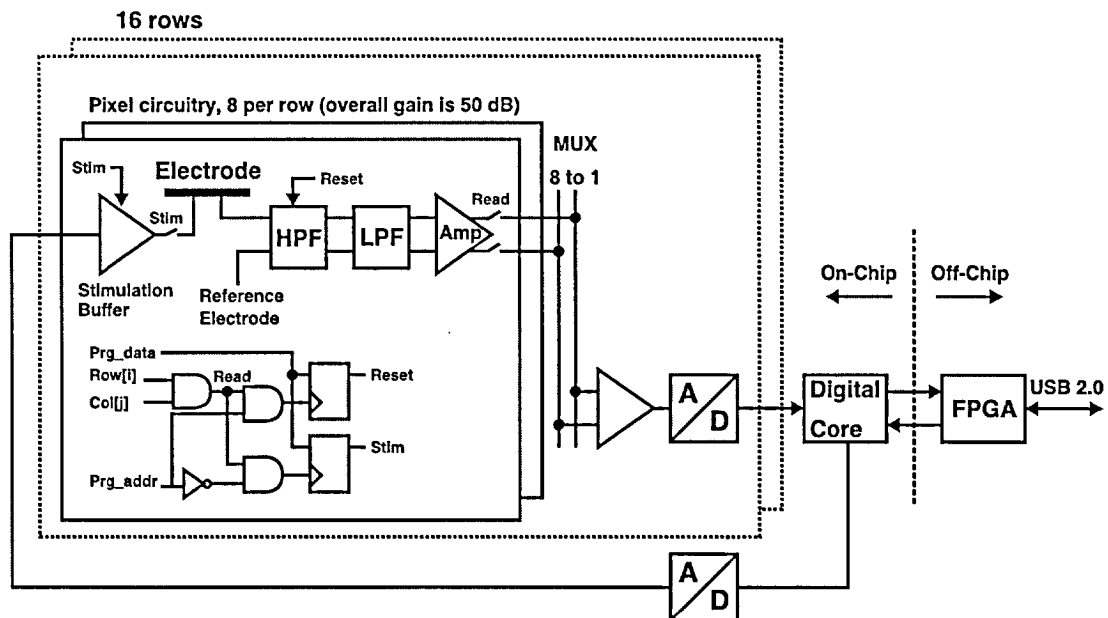
Figure 4.2: Block schematic of the overall system architecture

A total equivalent input noise of the pixel circuitry of 11.7 μV_{RMS} (0.1 Hz to 100 kHz) has been measured. The electrodes are continuously read out at a sampling rate of 20 kHz per electrode. A gain of 1000 or 3000 can be selected. The overall power consumption of the chip is 120 mW at 5 V supply, 20 mW of which are dissipated within the array. Electrogenic cells are very sensitive to temperature so that temperature changes may change cell activity and may even lead to cell death. An on-chip temperature sensor (see section 4.1.3) monitors the chip operating temperature. Operating the chip mounted on a ceramic package (Section 4.2.1) and with liquid on the surface leads to a temperature rise of less than 1°C with respect to ambient temperature, so that additional cooling of the system is not required. Circuits operating at low frequency (down to 1 Hz) might be sensitive to leakage currents, the effect of which has been reduced by the fully differential design of the in-pixel readout circuitry. Furthermore, electromagnetic coupling is also generally reduced in a fully differential architecture. The electrode units also provide stimulation capabilities. Any arbitrary stimulation pattern (with a maximum sampling rate of 60 kHz) can be applied to any subset of electrodes. The readout circuitry at each electrode can individually be reset to its operating point in order to suppress artifacts evoked by the stimulation pulses from the stimulated electrode itself or from neighboring electrodes. A summary of the main properties of the micro system is given in Table 4.1.

4.1 Design Considerations and Implementation

4.1.1 Readout Electronics

Specifications

The circuitry was designed to meet the specifications of extracellular capacitive recordings as described in chapter 2 and 3. When an action potential in an electrogenic cell occurs, ions flow across the cell membrane and induce charges on the metal electrode. The signal frequency range is from approximately 1 Hz to 5 kHz, and expected signal amplitudes are between 100 μV and 2 mV, depending on the cell type. Neuronal signals, for example, are in a frequency range from approximately 100 Hz to 5 kHz [3,32,100], whereas measurements with heart cells feature field potentials in a frequency range from approximately 1 Hz to 1 kHz [12,29]. The minimum Nyquist rate is therefore 10 kHz and a sampling frequency of 20 kHz per electrode has been chosen in order to achieve good resolution of the action or field potentials. A sampling rate of up to 160 kHz can be achieved when not recording from all electrodes of a row (details on page 4.1.1ff). This results in a higher temporal resolution or in noise reduction using oversampling techniques. Offset and drift that occur at the electrode can be significantly larger than the signal amplitude. As described in chapter 3, offsets of the electrode potential of up to 1 V and drifts of up to 100 mV within a few seconds have been measured. These low-frequency components need to be removed from the signal in order to be able to amplify the small signals without saturation of the subsequent circuitry. To this end, a high-pass filter has been used as the first read-out stage. The signals then pass a low-pass filter with a corner frequency of about 5 kHz to prevent high-frequency aliasing and to limit the noise bandwidth. Finally, a buffer with a larger bandwidth has been realized to further amplify the signal and to allow for multiplexing.

Another important parameter is the resolution of the A/D converter. The expected maximum signal amplitude is 500 μV for neural cell cultures [3,100] and 2 mV for heart cells [32]. The noise of the electrodes is in the range of 1-20 μV_{RMS} [12,44,101,102]. To achieve good signal-to-noise ratio, an 8-bit resolution for the A/D converters seems to be sufficient. The noise level of the electrode voltage is also an important design specification for the front-end amplifiers.
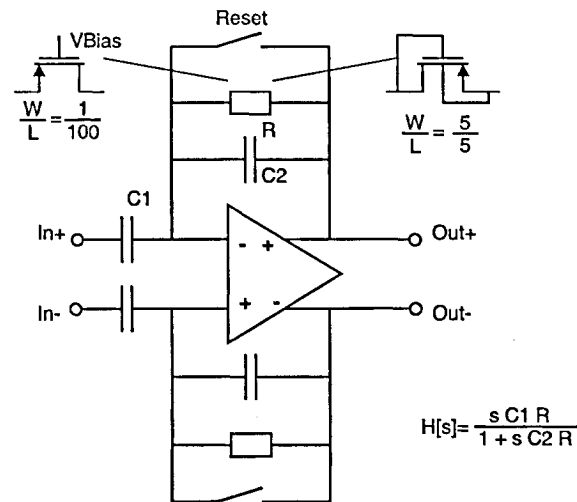
Figure 4.3: Circuit diagram of the High-Pass Filter (HPF in Figure 4.2). The high resistance needed in the feedback is realized using a MOS resistor. A test structure using a MOS diode has also been implemented.

Pixel readout circuitry

The first readout stage is a high-pass filter (see Figure 4.3 and HPF in Figure 4.2). This filter cancels drift and offset of the metal electrode, which can be significantly larger than the signal amplitude (see section 3.1). The high-frequency gain of the filter is 20 dB and is defined by the capacitance ratio $C1/C2 = 2pF/0.2pF$ (Figure 4.3). The corner frequency is given by the capacitor $C2$ and the Resistor R: $\frac{1}{2\pi RC2}$. The value of $C2$ is a trade-off between gain accuracy and corner frequency. The smaller $C2$, the larger is the gain, and the more relaxed are the noise constraints. But a small $C2$ also leads to problems in gain accuracy and requires a larger resistance, R, which may lead to problems with parasitic leakage currents. Given the spatial constraints imposed by the 250 μm pixel pitch, a 200 fF capacitance was chosen for $C2$. To realize a corner frequency of 1 Hz, a large resistance, R, is required. This large resistance has been realized by using a MOS resistor (the use of MOS transistors as resistors is described in [103]) with a gate length of 100 μm and a gate width of 1 μm. A minimum transistor width of 0.6 μm would be possible, but 1 μm has been chosen for a better matching. The absolute value of the resistor can be externally controlled by changing the gate voltage. The transistor is generally biased in the subthreshold region. The corner frequency can be tuned from approximately 1 Hz to about 1 kHz, which corresponds to resistances between 8 GΩ and 800 GΩ. A second design that makes use of a MOS diode to realize the large resistance has been implemented as a test structure (compare [101, 104]).

The corner frequency in this case was measured to be in the range of 1 Hz. For the MOS-diode-based approach no reference voltage is required, and less space is needed, but the filter stage is not tunable as is with the MOS resistor. The tunability of the MOS resistors can be advantageous if the signal band starts, e.g. at 100 Hz, since then, a good portion of the low-frequency can be cut off.

As shown in Figure 4.3, a switch is included in the high-pass filter. The idea is to bring the filter back to its operating point, when a large stimulation pulse saturates the filter as will be described on page 63. The OTA used in this filter (see Figure 4.4) is a fully differential folded-cascode amplifier occupying an area of 130x105 μm^2. The current in each branch is 2 μA, resulting in a total power consumption of 90 μW. The main noise contributions originate from the input transistors (*M1* and *M1'*) and the current sources (*M5* and *M5'*). Degeneration resistors (*R1* and *R1'*) decrease the noise from the current sources (*M5* and *M5'*) of the main amplifier. The value of these resistors results from the area-versus-noise trade-off of the transistors and the resistors themselves as will be described on page 60. The dominant pole of the amplifier is at the output nodes (*Out+* and *Out-*). The capacitor *C1* has been implemented to stabilize the amplifier, and the capacitors *C2* and *C2'* stabilize the common-mode feedback. The common-mode feedback includes source followers (*M12* and *M12'*) to ensure a purely capacitive load on the outputs (*Out+* and *Out-*). The open-loop DC-gain is 70 dB, the unity-gain bandwidth is 1 MHz, and the phase margin is 70°.

In the subsequent filter stage, a passive MOSFET-C low-pass filter (Figure 4.5) limits the noise bandwidth and prevents aliasing. The area (90 x 45 μm^2) of the passive low-pass filter was minimized by using MOS-resistors (*M1* and *M1'*) that are tunable by modifying the gate voltage and by using MOS-capacitors (*M2* and *M2'*). The corner frequency of the filter can be tuned from about 1 kHz to 30 kHz. Higher frequency signals, above about 200 kHz, can pass through the MOS resistor via the drain-source capacitance. In order to limit the bandwidth of those signals, the resistors *R* and *R'* have been added to the signal path. The MOS capacitors *M2* and *M2'* attenuate both, high-frequency differential as well as common-mode signals. Capacitors *C* and *C'* were used to limit the bandwidth of differential signals because they feature less non-idealities and less parasitics than MOS capacitors. The dimensions for *M1* are 1.2 μm / 50 μm, *R* is 26 kΩ, *C* is 300 fF and C_{M2} is approximately 1 pF, the elements marked with a prime have the same characteristics. The corner frequency of the low-pass filter is given by $1/2\pi 2R(C + \frac{1}{2}C_{M2})$, the corner frequency of the common-mode suppression is $1/2\pi RC_{M2}$. The differential signals are four times more attenuated than common-mode signals.
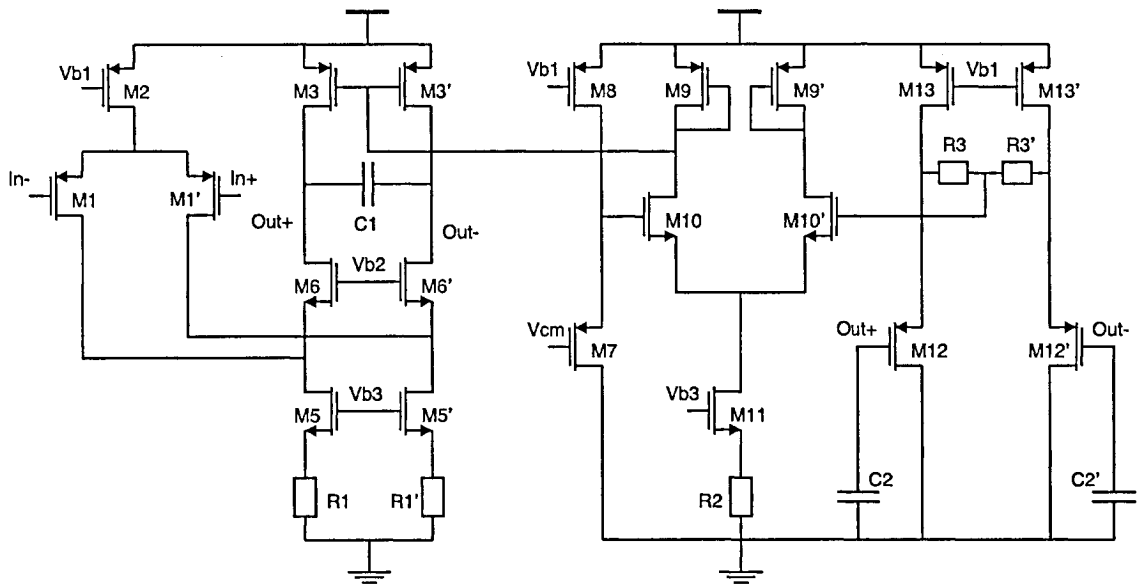
Figure 4.4: Circuit diagram of the operational transconductance amplifier in the high-pass filter.

Table 4.2: Transistor, capacitor and resistor dimensions, bias currents and common-mode voltage of the operational transconductance amplifier in Figure 4.4.

Transistor	W/L = [µm/µm]
M1	150/1
M2, M7, M12	20/2
M3, M8, M9, M13	10/2
M5, M11	20/5
M6	5/3
M10	30/5
Resistor	**Resistance [Ω]**
R1, R2	50'000
Capacitor	**Capacitance [pF]**
C1	0.2
C2	0.5
Current	**Value [µA]**
M8, M11, M13	2
M2	4

Figure 4.5: Circuit diagram of the low-pass filter (LPF in Figure 4.2).

Following the LPF, an additional amplifier (see Figure 4.6 and Amp in Figure 4.2) amplifies the signals and allows for fast multiplexing. This buffer is a fully differential version of the amplifier presented in [105] and has a gain of 30 dB. The key features of this amplifier are the high input impedance, large bandwidth, good linearity and the overall gain can be defined by resistor ratios. The concept of this amplifier is illustrated in Figure 4.6. The Transistors *M1* and *M1'* represent a degenerated differential pair with a resistive load, R_{deg}, and with grounded gm-boosting amplifiers *M2* and *M2'*. The PMOS input devices (*M1, M1'*) are forced to conduct a static current, *Ibias*, by the current sources at their drains so that these input devices ideally act as dc level shifters and create a linear voltage copy of the input signals from gate to source. Therefore, the voltage difference at the input terminals (*In+* and *In-*) is copied and drops across the degeneration resistor, R_{deg}. Transistors *M2* and *M2'* conduct a dc current, Ibias, and the signal current, I_{AC}, which is given by equation 4.1. A_0 is the open-loop gain of the gm-boosted amplifier.

$$I_{AC} = \frac{V_{In}}{R_{deg} + \frac{2}{gm1 \cdot (1+A_0)}} \cdot \frac{A_0}{(1+A_0)} \tag{4.1}$$

I_{AC} is copied from transistor *M2* to *M3* and from *M2'* to *M3'*, respectively, and flows across *Rout* = *Rout+* + *Rout-*. The total voltage gain is then given by I_{AC} multiplied by *Rout*. The total voltage gain A_{Amp} is consequently defined by resistor ratios and an error, which is mainly arising from the output resistance of the input transistor, *M1*, which is dominated by its transconductance *gm1*. If we assume A_0 to be large compared to the degeneration resistor, the total voltage gain can be simplified according to equation 4.2.
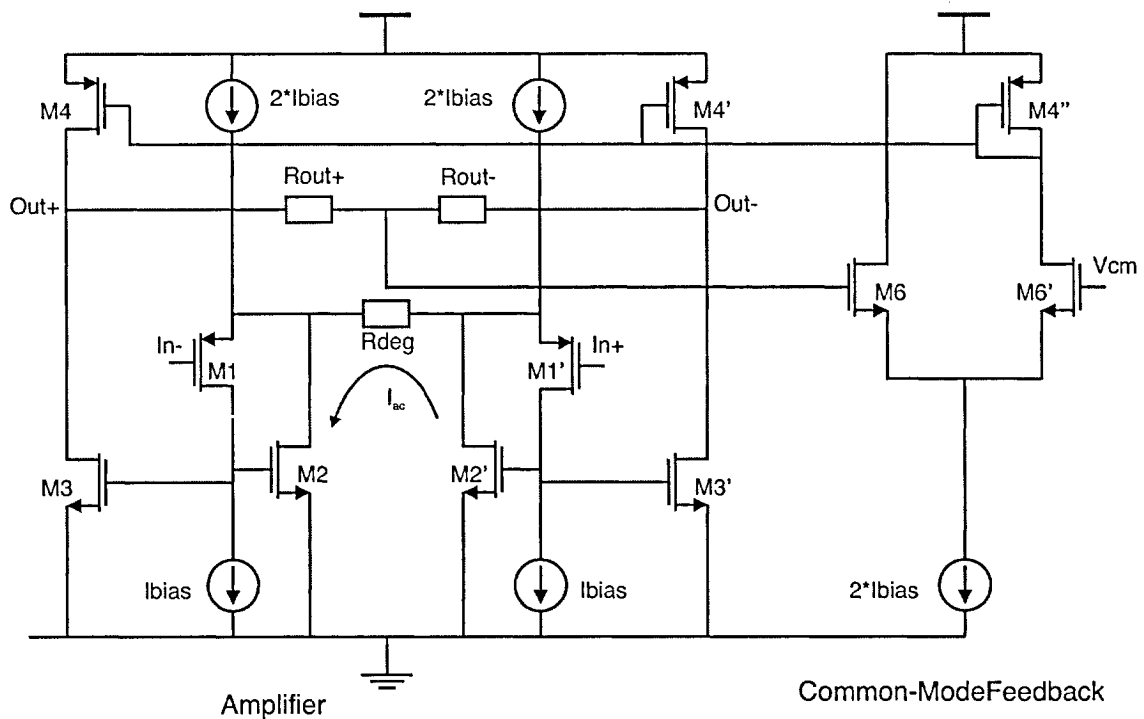
Figure 4.6: Circuit diagram of the fully differential amplifier that drives the multiplexed lines ("Amp" in Figure 4.2).

$$A_{Amp} = \frac{V_{Out}}{V_{In}} = \frac{R_{Out}}{R_{deg} + \frac{2}{gm1 \cdot (1+A_0)}} \cdot \frac{A_0}{(1+A_0)} \approx \frac{R_{Out}}{R_{deg}} \qquad (4.2)$$

The common-mode output voltage is sensed between $Rout+$ and $Rout-$ by the error amplifier on the right side in Figure 4.6 and is compared to Vcm. The dominant pole is at the output, and all other poles are far beyond the unity gain bandwidth so that the amplifier is very stable. The connection to the A/D converters is realized via CMOS switches ("*read*" in Figure 4.2).

Noise analysis of the in-pixel readout circuitry

The significant noise sources for the noise analysis are *M1*, *M3*, *M5*, *R1* of the OTA in Figure 4.4; *C1*, *C2*, *R* of the high-pass filter in Figure 4.3; and the passive elements of the low-pass filter, R_{LPF} and C_{LPF}. All these noise sources are assumed to be uncorrelated.

The equivalent-input noise of the folded cascode OTA described in Figure 4.4 is given by equation 4.3. The noise-spectral-density terms dv_i^2 (i=1,3,5) are re-

Table 4.3: Summary of the transistor sizes of the amplifier in Figure 4.6.

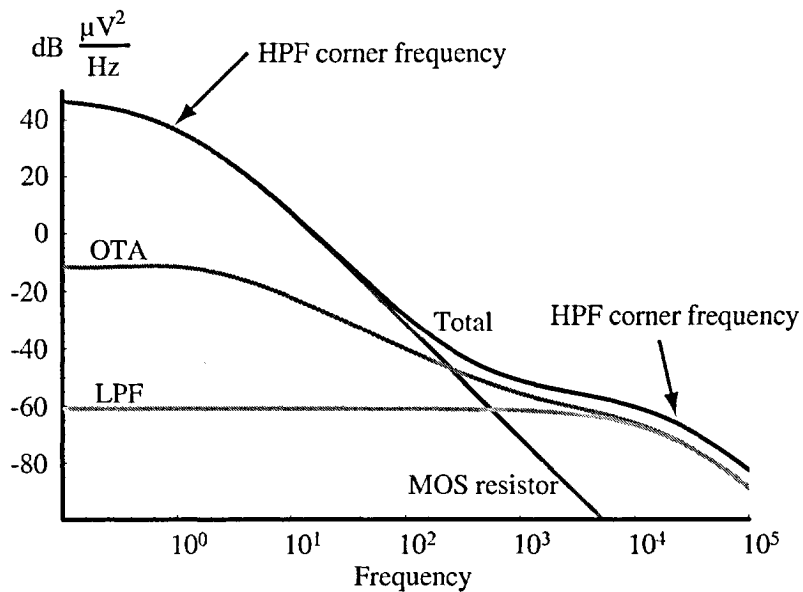| Transistor	W/L [μm/μm]
M1	20/2
M2, M3	8/8
M4	3/3
M6	16/1
Resistors	**Resistance [Ω]**
R_{Deg}	5'000
Rout	180'000
Currents	**Value [μA]**
Ibias	2

Figure 4.7: Input-referred noise spectral density of the in-pixel HPF and LPF. White noise from the MOS resistors and flicker noise from the OTA represent the main noise contributions of the readout circuitry.

placed by the expressions for the equivalent-input noise of the corresponding MOS transistors, M_i, as given in equation 4.4. The first and the third term in equation 4.3 are the noise contributions of $M1$ and $M3$ in reference to the input. The degeneration resistors R and R' considerably reduce the noise contribution of the current sources $M5$ and $M5'$, as can be seen in the second term of equation 4.3. The chosen resistance value of these resistors results from a tradeoff between noise, area consumption and output swing of the OTA. The inclusion of these degeneration resistors resulted in an area reduction of more than 50% for $M5$ and $M5'$, which corresponds to a 20% area reduction for the entire OTA, while the noise characteristics were preserved.

$$V_{eq,OTA}^2 = 2dv_1^2 + 2dv_5^2 \left(\frac{g_{m5}}{g_{m1}(1+g_{m5}R1)} \right)^2$$

$$+ 2dv_3^2 \left(\frac{g_{m3}}{g_{m1}} \right)^2 + 2 \cdot \frac{4kT}{R1} \left(\frac{1}{g_{m1}} \right)^2 \qquad (4.3)$$

$$dv_i^2 = \frac{8kT}{3g_{mi}} + \frac{KF}{W_iL_iC_{Ox}^2} \frac{1}{f} \qquad (4.4)$$

Equation 4.5 represents the output noise of the high-pass filter in Figure 4.3. The first term is the noise contribution of the OTA multiplied with the transfer function from the input terminal of the OTA to the output of the high-pass filter. The noise from the feedback resistors, R and R', is represented by the second term. Flicker noise from the input transistors of the OTA ($M1$ and $M1'$) and white noise from the resistors in the feedback of the high-pass filter (R and R') represent the main noise contributions to the overall readout circuitry noise. This is illustrated in Figure 4.7, the white noise from the MOS resistors is the dominating noise at frequencies below 100 Hz. In the frequency region between 500 Hz and about 5 kHz the 1/f noise of the OTA dominates the noise spectrum. At frequencies above 10 kHz the white noise from the OTA and the MOS resistor in the low-pass filter as the main contributors to the noise spectrum.

$$V_{no,HPF}^2 = V_{eqOTA}^2 \cdot \left(\frac{1+sR(C1+C2)}{1+sRC2} \right)^2 + 2 \cdot \frac{4kTR}{(1+sRC2)^2} \qquad (4.5)$$

$$V_{no,LPF}^2 = \left(V_{no,HPF}^2 + 2 \cdot 4kTR_{LPF} \right) \cdot \left(\frac{1}{1+sR_{LPF}C_{LPF}} \right)^2 \qquad (4.6)$$

The total output noise including the passive low-pass filter (LPF in Figure 4.2)

is shown in equation 4.6. The contribution of R_{LPF} ($4kTR_{LPF}$ in equation 4.6) to the total noise is small, but the noise bandwidth is drastically reduced by the low-pass transfer function. Finally, the total equivalent input-referred noise is obtained by dividing $V^2_{no,LPF}$ by the gain C1/C2 of the high-pass filter. The total noise is plotted in Figure 4.7 and compared with measurements in Figure 5.3 in section 5.1.1.

In-pixel mode selection and reset

As is shown in Figure 4.2, each electrode has a small digital circuit to control the pixel operation. Row- and column-addressing signals (*Row[i]* and *Col[j]*) are generated by the digital core. *Pixel[i,j]* is sampled when *Row[i]* and *Col[j]* are high. The signals *Prg_data* and *Prg_addr* are also produced by the digital core and are used to set the pixel operation. If *Prg_addr* is low, the flip-flop for stimulation (*stim*) is addressed, and the value of *Prg_data* at that time is stored. Similarly, the flip-flop for *reset* is set to the value of *Prg_data* if *Prg_addr* is high when the pixel is selected. Since the *read* signal has a rising edge every 50 μs it is possible to set one of the flip-flops every 50 μs. The *stim* signal powers up the stimulation buffer and connects the buffer to the electrode by closing a switch. Communication between chip and external electronics and the coding of the information on selection and reset will be described on pages 65ff.

Electrical stimulation pulses will disturb the neural recordings on the stimulating electrode and on neighboring electrodes by causing large artifacts, which might superimpose with action potentials occurring during the decay time of this artifact (more than 5 ms). Such artifacts have limited the use of combined stimulation and recording techniques so far. There are several recent papers on removing the stimulation artifact [106–108]. However the described methods are computationally expensive and often require real-time processing. In the design presented here, an artifact cancellation technique is implemented directly in the pixel circuitry. A similar approach has been realized with discrete off-chip components by Jimbo et al. [55].

A simulation of the reset operation is shown in Figure 4.8. The HPF (schematic in Figure 4.3) saturates when a large input signal is applied. As a result, the outputs of the HPF, *HPFout+* and *HPFout-*, saturate and the input nodes of the OTA get charged since the resistance of the MOS resistors is significantly reduced for a short period of time. Afterwards, this charge has to be removed from those nodes, which is a very slow process as it can be seen in the slow decay of the outputs of the HPF (Figure 4.8 left). The discharge operation without
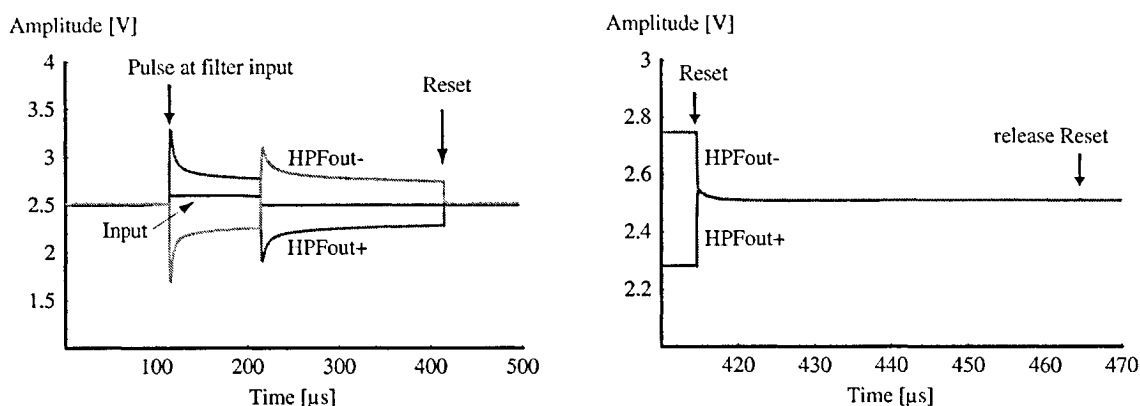
Figure 4.8: Recovery of the in-pixel HPF after saturation upon using the reset switch. The right graph shows the effect of the reset at enlarged time scale.

the reset switch takes several 100 ms. When the *reset* switch is closed, the OTA is in buffer mode and brings the filter back to proper operation within a few microseconds. But, it takes 100 μs to record the first value. The reset switch is released earliest after 50 μs and then it takes another 50 μs to record the first post-reset signal. It is worth mentioning that this reset operation would be critical without the differential design. In a single-ended design, charge injection due to opening of the reset switch would eventually set off the circuit from the operating point again.

Circuitry per row of electrodes

Each row comprising eight electrodes is connected to one A/D converter. Since a single-ended A/D converter is used, the fully differential signals need to be converted to single-ended signals. A switched-capacitor amplifier is used for this conversion. This switched-capacitor amplifier features an opamp offset voltage cancellation and is insensitive to low opamp gain. Clock feed-through and charge injection are also reduced by additional switching circuitry and by the differential design. Details on the operation of this amplifier are given in [109]. A gain of 10 dB or 20 dB is selected by changing the feedback capacitance, which leads to an overall amplification of the complete readout chain of 1'000 or 3'000. The signal is then digitized by a successive-approximation A/D converter with 8-bit resolution. All sixteen successive-approximation registers of the sixteen converters are implemented in the digital part. The intention here is to completely separate all clocked digital circuitry from the analog parts.

- Stimulation Signal
- Stimulation Pattern
- Electrode Reset
- Chip Clock&Reset

- Stimulation Signal
- Stimulation Pattern
- Reset

Real-Time Visualization
Stimulation Data

MEA128   Digital Lines   **FPGA**   USB 2   **PC**

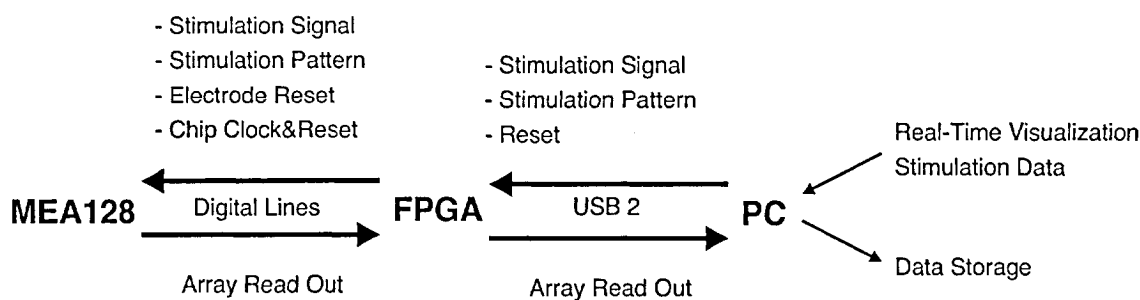Array Read Out   Array Read Out

Data Storage

Figure 4.9: Signal chain. Sample data from the electrodes are pre-processed in the FPGA. Using a spike detection algorithm in the FPGA, only events are passed on to the computer.

Digital Core

The digital core operates at 1.6 MHz clock speed and scans the array in a programmable manner by steering the array column and row signals, and by operating the ADCs accordingly. The combination and order of how electrodes are read out is determined by a programmable look-up table (LUT). This LUT allows for restricting the sampling to subsets of each row of electrodes. For example, a row entry *{0,1,2,3,4,5,6,7}* records from all eight electrodes in the corresponding row at 20-kHz sampling rate. An entry *{0,1,2,3,0,1,2,3}* entails recording from the first four electrodes in the row at a sampling rate of 40 kHz and *{0,2,4,6,0,2,4,6}* entails recording from every second electrode at 40 kHz. A maximum sampling rate of 160 kHz of the first electrode in a row is achieved using an entry {0,0,0,0,0,0,0,0}. The status of each cell (*stimulation*, *reset* or only *recording*) is stored in two in-pixel flip-flops, which are updated at a rate of 20 kHz.

A Spartan-II FPGA in conjunction with the Cypress FX-2 USB 2.0 chip, both running at 48 MHz, are used to connect to a PC for data capturing and visualization (Figure 4.9). The micro-electrode-array chip transmits a continuous data stream of 128 x 20 kHz x 8 bit = 3.2 MB/s to the FPGA on a 16-bit-wide bus. The transmission from the chip is organized into 10-clock-cycle blocks given by the conversion time of the A/D converters (two clock cycles are required for the sample-and-hold operation and eight clock cycles are needed for conversion). In order to synchronize the chip with the external electronics, the first data value is preceded by a new-frame signal.

The chip input is a continuous stream of 0.4 MB/s on a 2-bit-wide bus from the FPGA. To minimize decoding logic and core size, the protocol for communication with the MEA128 is free of operational codes. Input always comprises

Table 4.4: Transmission cycle of a stimulation value; each word corresponds to 10 bit of input data. Transmitted are also 3/8 of a selection pattern (columns 0 to 2 and 7 to 10) and 1/96 of the column selection look up table bank (LUT).

Signal	word 0	word 1	word 3
rx_data_0	$select_{col=1,row=0..7}$ $data_6$ addr	$select_{col=1,row=0..7}$ $data_3$ addr	$select_{col=2,row=0..7}$ $data_0$ addr
rx_data_1	$select_{col=8,row=0..7}$ $data_7$ $data_5$	$select_{col=1,row=0..7}$ $data_4$ $data_2$	$select_{col=2,row=0..7}$ $data_1$ LUT

stimulation data (60 kHz sampling rate, 8 bit), electrode selection- and reset patterns (20 kHz refreshing rate), and the LUT data (555 Hz refreshing rate). Table 4.4 shows the encoding of three out of eight words of the input data stream. The data is encoded in stimulation data (*data*), selection data (*selection*) and an option (*addr*), which defines if a selected electrode is either reset or selected for stimulation. Additionally, every third word contains one entry for the LUT, which is continuously updated.

4.1.2 Stimulation Electronics

Specification

Stimulation of electrogenic cells can be realized by means of current or voltage pulses. Intra-cellular stimulation during patch clamp measurements is usually done in current mode since stimulation of the neurons in their natural environment occurs through currents via their dendritic inputs. For extracellular stimulation, both, voltage [12,47,55,110] and current stimulation [6] are widely used. When current stimulation is used, the total charge that passes the electrode-electrolyte interface is known. The electrode impedance, however, significantly varies with electrode size, material [97,111] and as a consequence of cell growth [68]. Thus, high voltages can occur, when the impedance is large, which requires a voltage-limiting element in order to prevent electrolysis, which may change the local pH or damage the electrode. Voltage stimulation has the advantage that the voltage at the electrode is well controlled and electrolysis is avoided as long as the voltage is kept small enough. Moreover, capacitive stimulation through an isolating layer is possible [110]. For these reasons voltage
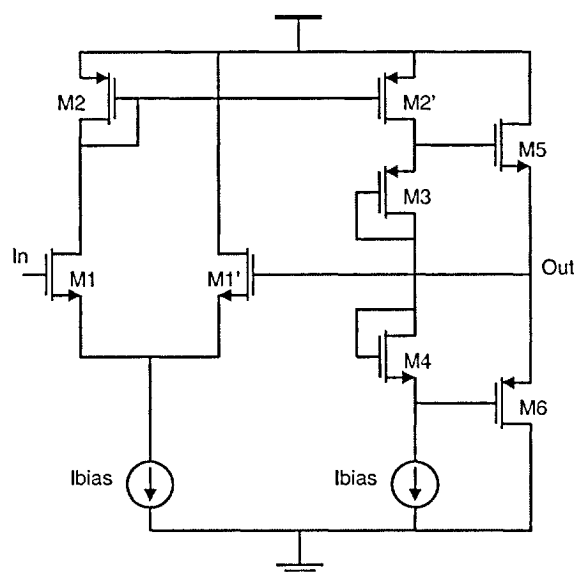
Figure 4.10: Circuit diagram of the class-AB buffer for stimulation.

stimulation was implemented in this design.

Further requirements include that the number of activated stimulation electrodes and, therefore, the load for the stimulation circuitry can vary. Therefore, it is necessary to implement a buffer at each electrode. The double-layer capacitance of an electrode can be larger than 1 nF. Sampling rates for the stimulation reported in the literature are up to 10 kHz when a square wave tetanus signal is applied to the electrode [3]. In order to stimulate with a variety of waveforms, a stimulation sampling rate of 60 kHz has been chosen, which entails the use of a buffer with a slew rate of 4 V/16 μs = 0.5 V/μs at a load of 1 nF. Since the overall power consumption should be kept low and the area should be kept small, we decided to implement a buffer with a class-AB output stage, which is powered down while the electrode is not selected for stimulation.

Implementation

The stimulation buffer (Figure 4.10) includes a differential input stage (*M1*, *M1'*) with an active load (*M2*) and is connected for unity gain operation (*Out* connected to gate of *M1'*). The class-AB stage is formed by the transistors *M3*, *M4*, *M5* and *M6*, where *M3* and *M4*, both diode connected, define the biasing of the output transistors *M5* and *M6*. If the input voltage (*In*) is increased, *M5* forces the output voltage (*Out*) to follow. The current through *M2* and *M2'* is increased, which raises the gate voltages of *M5* and *M6*. The load current is delivered by *M5*, the gate-source voltage (V_{GS}) of which will increase. Since a

constant voltage is maintained between the gates of *M5* and *M6* the V_{GS} of *M6* decreases by the same amount that the V_{GS} in *M5* increases. *M6* stays on, but conducts only a small current. When the input voltage is lowered the situation is inverted with *M6* forcing *Out* to follow and with the current through *M5* decreasing. The bias current is 2 μA, and the quiescent current of the output is 24 μA so that the total power consumption of this buffer is 150 μW at 5 V when no input signal is applied. However when slewing, the amplifier can deliver up to 10 mA to the electrode. This corresponds to a maximum current density of 60 A/cm². The whole buffer occupies an area of 42 x 32 μm².

Table 4.5: Summary of the transistor sizes of the class-AB buffer in Figure 4.10.

Transistor	W/L [μm/μm]
M1, M1'	10/0.6
M2	15/0.8
M2'	30/0.8
M3	12/0.6
M4	30/0.6
M5	45/0.6
M6	18/0.6

4.1.3   On-chip Temperature Sensor

Introduction

Electrogenic cells are very sensitive to temperature so that temperature changes may change cell activity and may even lead to cell death. An on-chip temperature sensor monitors the chip operating temperature and allows for controlling it by means of an external heater. The target temperature is around 37°C for most biological cells. The temperature sensing principle is based on the principle used in band-gap references. Integrated band-gap references and temperature sensors are closely related because they are all based on the approximately linear temperature dependence of the base-emitter voltage V_{BE} of diode-connected bipolar transistors. Taking the difference between the V_{BE}s (ΔV_{BE}) of two identical bipolar transistors biased at different currents leads to a voltage, which is proportional to the absolute temperature (PTAT) (see equation 4.8) and can be used for temperature sensors [112, 113].
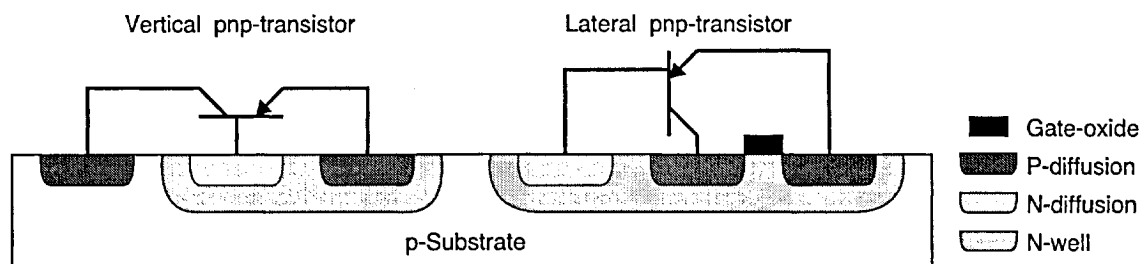
Figure 4.11: Bipolar transistors available in a standard n-well CMOS process: Vertical substrate pnp-transistor (left) and lateral pnp-transistor with n-well as base (right).

Bipolar Transistors in the CMOS Process

Two parasitic bipolar transistors (the lateral and the vertical pnp-transistor) are available in standard n-well CMOS technology (Figure 4.11). The lateral pnp-transistor is rarely used for temperature sensors, since it has large process tolerances and exhibits non-idealities due to the use of a gate to separate emitter and collector. The vertical pnp-transistor has better performance and less process spread, but the collector is tied to the negative supply, and, therefore, the collector current is not accessible. Most CMOS references and temperature sensors rely on the vertical pnp-transistor.

The base-emitter voltage of a bipolar transistor as a function of the collector current, I_C, is accurately described by

$$V_{BE}[T] = \frac{kT}{q} \ln\left(\frac{I_C[T]}{I_S[T]}\right) \tag{4.7}$$

T is the absolute temperature, q the electron charge, k the Boltzmann constant and I_S is the saturation current, which depends on process variables, temperature and the transistor geometry. The following equation results, if the difference between the V_{BE}s (ΔV_{BE}) of two identical bipolar transistors biased at different currents is taken.

$$\Delta V_{BE}[T] = \frac{kT}{q} \ln\left(\frac{I_{C1}}{I_{C2}}\right) \tag{4.8}$$

The ΔV_{BE} is proportional to the absolute temperature. Equation 4.8 contains only physical constants and no process-depending variables, such as I_S.
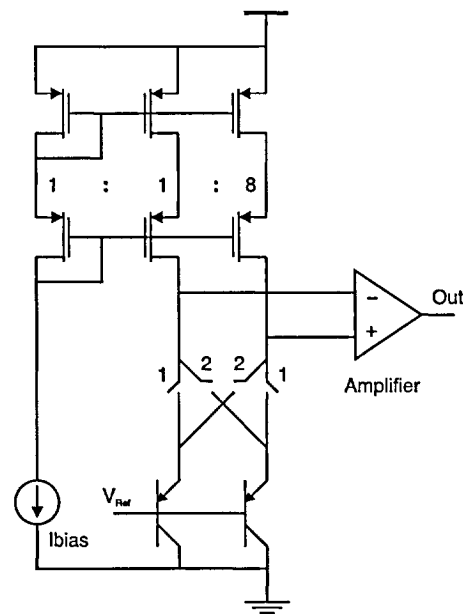
Figure 4.12: Temperature sensor based on the difference of the base-emitter voltages of two identical transistors at different currents.

Implementation

For the MEA128 system, the idea is to have an integrated temperature sensor underneath the cell culture. The temperature is then regulated via an external heating resistor underneath the packaged chip. In the MEA128 an analog voltage output can be used by an external controller. The next generation will be able to feed the signal from the temperature sensor in one of the A/D converters, so that the temperature can be digitally controlled. A schematic of the temperature sensor is shown in Figure 4.12.

The identical bipolar transistors, *T1* and *T2*, are biased at different current densities, I_{C1} and I_{C2}. The current I_{Bias} is generated by a bandgap reference and should show only little temperature dependence. The ratio of I_{C1} and I_{C2} is important and not the absolute value, as can be seen in equation 4.8. The current ratio through the transistors is 8, which yields for the right side of equation 4.8 to $\frac{kT}{q}\ln 8$. The transistors can be chopped (indicated by the switches *1* and *2* in Figure 4.12) so that any mismatch between the two transistors can be canceled. In the MEA128 the ΔV_{BE} is then fed to an amplifier with the same architecture as the the amplifier in Figure 4.6. However, this amplifier shows process dependence such as offset or gain variability. The offset of the amplifier is canceled when measuring first with the switches *1* closed then with the switches *2* closed and subtracting the results. Nevertheless, gain variabilities from chip to chip

arise from processing spreads of the resistors and transistors, which makes it necessary to calibrate each chip individually. For this reason a switched capacitor amplifier with correlated double sampling will be implemented in the next generation of the MEA128, the same design as the switched-capacitor amplifier in the readout chain (Section 4.1.1). The only process dependence that has to be taken into account is the gain variability of this amplifier, which relies on capacitor ratios and should be smaller than in the MEA128.

Result

The on-chip temperature sensors of four chips have been characterized using a climate chamber[2]. The temperature was swept from 20°C to 50°C and a 2-point calibration was performed. The measured sensitivity is about 210 μV/°C, and the error is less than 0.2°C.

With this on-chip temperature sensor the temperature can be controlled via an external heating resistor. Cooling of the system is not necessary as long as the room temperature is lower than the target temperature of 37°C. The heat dissipated by the CMOS chip is quite small. When the chip is mounted on a ceramic package or PCB (Section 4.2.2) and has liquid on the surface a temperature rise of less than 1°C was observed upon powering up the chip.

---

[2]Trio Tech Artic 60, www.triotech.com

4.2   Post-processing and packaging

Packaging is a challenging and time-consuming task when CMOS electronics and cells or biology come together. Special measures are necessary so that both, the CMOS chip and the cells, survive culturing. A packaged chip (Figure 4.14) is required to operate for several months with physiological solution and cell culture on top. The cells need a controlled atmosphere with a specifically defined temperature, humidity and CO_2 concentration. For this reason the chips are placed in an incubator, which provides an atmosphere of 95% humidity, and 5% CO_2 at 37°C. All materials that come in contact with the culture medium have to be biocompatible. The chip surface and the bondwires have to be tightly sealed from the culture medium. A special chip surface coating is needed to protect the underlying electronics from the physiological solution as well as the cells from the toxic materials used in the CMOS electronics, such as aluminum (Al). The smallest pin hole in the surface immediately leads to corrosion of the Al, thereby releasing harmful metal ions into the culture medium. The standard electrode potential of Al (-1.66 V) is significantly more negative than that of platinum (Pt, +1.20 V) or gold (Au, +1.69 V), so that the contact between Al and a noble metal, in the presence of an electrolyte such as the culture medium, creates a galvanic element. If the Al is not properly sealed, and both the Al and Pt are in contact with the culture medium, then the Al will spontaneously dissolve. This problem was solved by shifting the electrode and applying a stack of alternating SiO_2 and Si_3N_4 layers on the chip during the post-processing as described in section 4.2.1. Similarly, the bondwires and the bondpads immediately start to dissolve when they come in contact with the physiological solution. Electrochemical reactions are accelerated by the fact that voltage differences between two bondwires can be up to 5 V during operation. Various materials were used to encapsulate the bondwires and protect them from the physiological saline, a summary of which is given in table 4.6. Additionally, a technology has been developed to use a flip-chip packaging technique to integrate the CMOS chip together with microfluidics for nutrition and drug delivery (page 78).

4.2.1   Electrode post-processing

Electrode Material

In addition to Au and Pt, many different materials have been developed as a cell contact material: titanium nitride (TiN) [53], indium-tin oxide (ITO)

[2], palladium [54], iridium oxide (IrO) [82] or the silicon oxide of open-gate FETs [7]. The key requirements for the electrode material are biocompatibility, process compatibility, low impedance and high charge storage capacity. This last requirement refers to the fact that, in the ideal case no faradaic currents should flow since the products of redox reactions may damage the cells. Low impedance is particularly important for stimulation and when small-area electrodes are to be used, i.e. for high spatial resolution recordings. A smaller electrode area becomes more sensitive to random charge fluctuations, introducing noise to the recorded signal. As a result, techniques are used to increase the total electrode surface area, such as surface roughening [86]. The most common surface roughening technique is the electrochemical deposition of dendritically structured Pt, referred to as Pt black [81, 114], which can be deposited on either Au or Pt [14,51]. This approach has also been used for the chips presented here.

Electrode Fabrication

Special post-CMOS processing steps were required to fabricate the Pt-electrodes and to render the chip surface more robust with regard to the working conditions described above. A two-mask post-processing procedure is applied to realize noble-metal electrodes and to completely cover the Al contacts (see Figure 4.13 and [69]). First, the bond pad opening process step of the CMOS process is used to open the electrode contacts. The Al contact is then covered with ~50 nm TiW, an adhesion promoter, followed by ~270 nm of Pt. The metals are sputter-deposited and structured in a lift-off process. In order to avoid pinholes, an alternating SiO_2/Si_3N_4 passivation stack consisting of 1 μm of Si_3N_4, and two times 100 nm SiO_2 and 200 nm Si_3N_4 (total layer thickness of 1.6 μm) is deposited using plasma-enhanced chemical vapor deposition (PECVD). A mixed-frequency PECVD process was used to match the passivation stack stress with that of the underlying Si_3N_4 deposited during the CMOS process. Reactive-ion etching (RIE) is then used to open the nitride stack and to define the location, size and shape of the electrodes. The electrode post-processing offers great flexibility since the electrode dimensions and locations do not have to be defined during the CMOS process. Various electrode layouts have been realized depending on the application. Electrodes with a pitch ranging from 50 μm to 500 μm, both round and square electrodes with sizes of 10 μm to 50 μm have been fabricated.
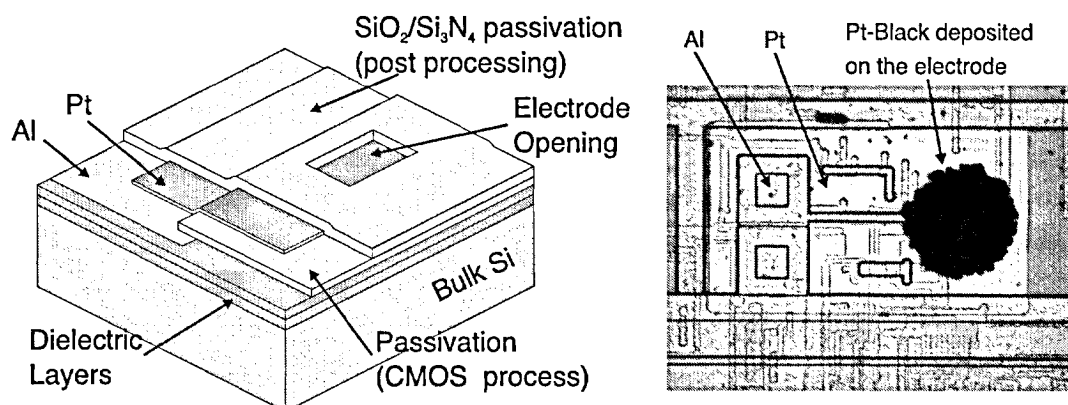
Figure 4.13: Post processing of the microelectrode. A schematic representation of the important layers is given on the left and a micrograph of the shifted electrode is shown on the right side.

Platinization

Often, the Pt electrodes are covered with platinum black (Pt-black) [114] to reduce the electrode-electrolyte impedance. The dendritic structure of Pt-black increases the surface area, and the electrode impedance is decreased by two orders of magnitude [97, 115]. Pt-black is electrochemically deposited on the electrodes using 0.25 nA/μm^2 current density applied to electrodes in contact with a solution containing 7 mM hexachloroplatinic acid, 0.3 mM lead acetate, and hydrochloric acid to adjust the solution pH to 1.0. A platinum wire is used as the counter electrode and is connected to an external current source. The on-chip stimulation circuitry is used to set the electrodes to a defined potential. Figure 4.13 (right) shows an electrode with Pt-black.

4.2.2 Packaging

The package for a CMOS chip to be used with biological cells has to fulfill two main requirements. First, a bath or flow-through system for nutrient delivery to the living cells has to be incorporated. Second the packaging has to protect the electric connections from the chip to the outside world from being attacked by the physiological solution. The material that comes in contact with the cells has to be biocompatible and it has to tightly connect to the chip surface so that no liquid flows between the chip and packaging material. Next, the bond wires may not be pulled off, either by thermal expansion or by swelling of the material due to liquid absorption. An optical material that is permeable to visible light

is preferred, allowing for an optical inspection to detect flaws. The packaging approaches presented here make use of different epoxies and/or polydimethyl siloxane (PDMS) to encapsulate the CMOS chips. Details on the procedures are described in this section.

State of the Art

Other groups successfully cultured cells on packaged silicon chips. For example Jenkner et al. [58,116] used a perspex chamber and glued it to the surface with a medical glue (MK3, Sulzer Osypka GmbH, Germany). DeBusschere et al. [32] used a PDMS chamber and a gasket seal to form a chamber and to protect the bond wires. Additionally, an insulative and protective epoxy (EP42LV, Masterbond, Hackensack, NJ) encapsulation layer was applied to the bond wires. Eversmann et al. [13] glued a cultivation chamber on the chip with silicone after the bond wires were protected by epoxy. None of these designs have been used for long-term incubation and, therefore, it is not sure that these approaches would sustain several months in the incubator. Cultivation of more than one month was carried out by Baumann et al. [54]. A polycarbonate CNC component was used for encapsulation. The CNC encapsulation was glued on the sensor chip in a ceramic IC socket with a thin film of biocompatible silicon glue. Voelkner and Fromherz [59] successfully measured signals from mammalian neurons after 25 days in vitro. The silicon chip has been mounted onto a ceramic package, wirebonded, and a polypropylene culture chamber was glued onto the chip with silicone adhesive.

Epoxy-and-PDMS Package

The processed chips are mounted on a PLCC84 ceramic package (see Figure 4.14) and encapsulated in a two-step procedure. An epoxy (Masterbond 42HT-T, Masterbond Inc., U.S.A.) is first used to encapsulate and stabilize the bond wires. Before curing the epoxy at 80°C for 2 hours, it has been left at room temperature for 12 hours to prevent the epoxy to flow across the chip due to a temperature-related viscosity change. The chips were exposed during 2 minutes to an oxygen plasma to clean and activate the surface. PDMS has then been applied to form a bath, isolating the bond wires from the cells. A glass O-ring, affixed to the package with PDMS, forms a larger bath capable of containing a suitable amount of culture medium. A Teflon stamp was used to prevent the active area from being covered with the PDMS. The PDMS has been cured at 80°C for 2 hours.

*Table 4.6: Different packaging materials and their advantages and disadvantages ("Bio" stands for biocompatibility). * has not been tested for biocompatibility but is used in similar applications by other research groups [12].*

Material(s)	Bio	Optical Properties	Incubation Sustainability
PDMS	+	transparent	swells, permeable to liquid
Masterbond	?*	opaque	does not seal when not protected by PDMS
PDMS + Masterbond	+	opaque	good
EPOTEK 301	+	transparent	bad surface adhesion
EPOTEK 353ND	+	red, transparent	good
EPOTEK 302-3M	+	transparent	under test

Previous trials using only PDMS without fixing the wires with epoxy resulted in an unstable package. PDMS tends to swell when it comes in contact with liquid, which causes the bondwires to detach from the bondpads. In a next approach, the epoxy was used to stabilize the bond wires. Then, PDMS was applied to form a bath as in the first approach. This solution works for a few days, but the PDMS is partly permeable for the liquid. As a consequence, the bondwires started dissolving at the locations where they were only covered by PDMS and not by epoxy.
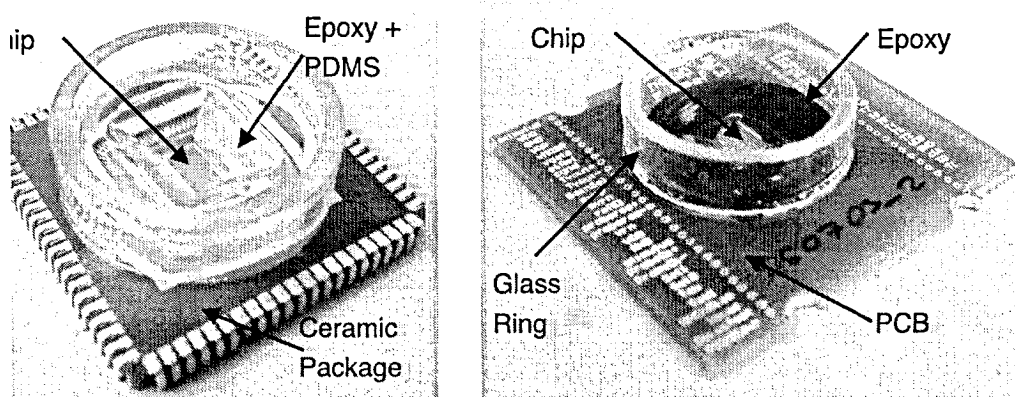
Figure 4.14: Packaged CMOS chips. Left: The chip has been mounted on a ceramic package, PLCC84. The bond wires were protected with epoxy and then a bath has been formed by PDMS and a glass o-ring. Right: The chip has been mounted on a custom designed PCB. The bondwires have been encapsulated using an epoxy (EPOTEK 353ND) and a glass o-ring forms a bath.

Epoxy-only Strategy

A faster procedure would be to cover the chip with epoxy only thereby shortening the procedure to a single processing step. Chips with three different epoxies have been packaged and tested. First, we used the Masterbond 42HT-T and fixed the glass ring with only this epoxy. But liquid flowed between chip and epoxy, and most chips were destroyed after a few days in the incubator showing corroded bond pads or mechanically disconnected bond wires. Rinsing the chip surface with isopropanol and applying subsequent oxygen-plasma cleaning improved the connection between chip and epoxy but was yet not sufficient.

Two other biocompatible epoxies have been tested: EPOTEK 301 and EPOTEK 353ND. Both epoxies meet the requirements of a USP Class VI Plastic, which ensures their biocompatibility. According to the datasheet the EPOTEK 301 should form a strong connection to SiO_2, but the sealing proved to be inadequate. All packaged chips were destroyed when placed in the incubator with culture medium in the bath. Chips packaged with EPOTEK 353ND formed a tight seal and survived several months of incubation. The EPOTEK 353ND was applied using a syringe and then left at room temperature for about 5 hours before a temperature ramp was applied. The epoxy was cured for 2 hours at 40°C, 1 hour at 60°C, 30 minutes at 80°C, 10 minutes at 110°C and then slowly cooled down within about 1 hour. The main reason for the room temperature curing and the temperature ramp is the slow change of viscosity. The viscosity

increases slowly so that the epoxy hardens without flowing over the active area. If the freshly prepared epoxy is heated above 60°C it immediately flows over the entire chip surface including the electrodes. Furthermore, it is important that the epoxy coverage is not too thin, so that the distance between the bondwires and the culture medium is not too small, otherwise crosstalk between the digital circuitry and the solution can perturb the measurements as a consequence of capacitive coupling. A new epoxy (EPOTEK 302-3M) is currently under test. This epoxy has excellent exothermal characteristics and has low water absorption properties.

Chip on Board

The connection leads of the ceramic package, PLCC84, were attacked when the packages were incubated for several weeks. The leads corrode and can only be used after treatment with sand paper, or may even fall off. We replaced the ceramic package by a custom designed PCB (Printed Circuit Board) with gold-plated connections (Figure 4.14). The chip has then been directly bonded on the board, in a as *Chip On Board* like technique. This method offers significantly more flexibility in terms of integration with other structures such as microfluidics. The design of the package can be individually adjusted for a given application, which is not possible with ceramic packages. Furthermore, the custom-designed PCB is about four times cheaper even for low-volume production. Before using the PCBs for packaging they were heated to 150°C for 12 hours to remove any solvents, which may be harmful to the cell culture. The chip has been encapsulated with epoxy as described in the previous section on page 77.

Flip-Chip and Microfluidics

The terminology flip chip originates from the upside-down (i.e. flipped) mounting of an IC chip. This leaves the chip pads and their solder beads facing down onto the package, while the back side of the chip faces up. Flip chip does not require any wire bonds. Instead, solder beads are placed on the chip pads. The chip is mounted upside down on the substrate (e.g. a PCB), and the solder is allowed to reflow. The advantage of flip chip technology is the capability of connecting all the I/Os in one single process step. Additionally, the bumps can be spread over the whole chip surface. This means the I/O density on the chip can be significantly higher than of devices with wire bonding. Wire bonding
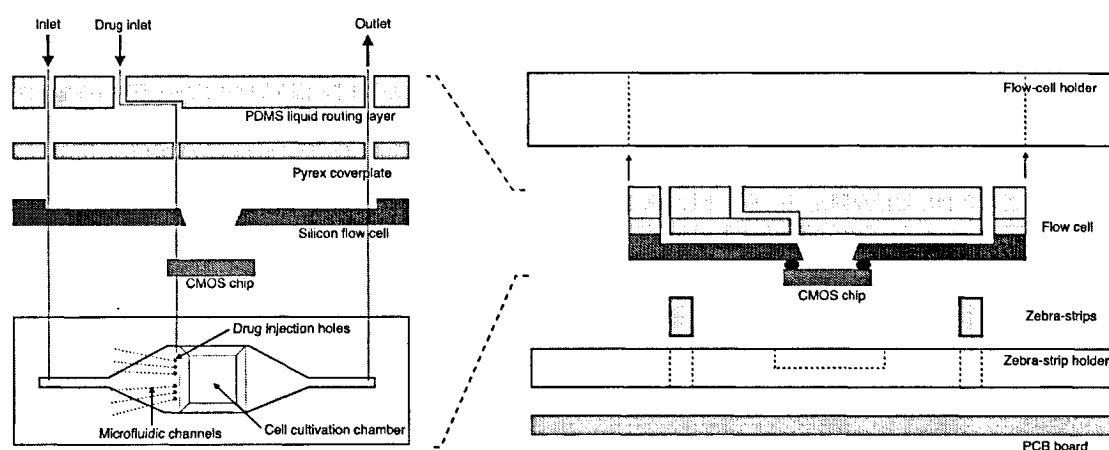
Figure 4.15: Side view and top view of the microfluidic system consisting of a silicon flow cell, a pyrex plate and a PDMS top (left). The flow cell with the attached chip and the zebra strips are placed in a PMMA chip holder and screwed onto a PCB (right).

is a mature technology and is very flexible. For chips with 500 and more connections flip-chip is the technology of choice, below 500 wire bonding is often cheaper. Here, we want to use another advantage of the flip-chip technology. We apply this technique to electrically and mechanically interconnect a CMOS MEA to a microfluidic module in one step. The microfluidic module allows for continuously controlled supply of fresh nutrient medium and for the removal of toxic waste products. Furthermore, additional channels incorporated in the microfluidic module can be used to locally add chemicals such as growth factors or pharmaceuticals.

A schematic of the flow cell is shown in Figure 4.15 and a flow cell with integrated connections for flip-chip bonding has been fabricated by IMT in Neuchatel[3]. This silicon flow cell comprises an opening for the active area and electrical connections, where the chip can be attached using flip-chip. The flow cell is then electrically connected to a PCB board using zebra strips from Fujipoly[4].

The chip layout has been modified in order to be used for flip-chip packaging. The bondpads of the MEA128 are 150 µm in diameter and have a pitch of 300 µm (see Figure 4.1). These relatively large pads make the flip-chip bonding more reliable. A wetting layer for the solder bumps has to be placed on the Al

---

[3]www.unine.ch/imt

[4]www.fujipoly.com

of the bond pads. Aluprep BP Zincate from Rohm&Haas Electronic Materials[5] has been used to remove the aluminum oxide from the bond pads and to deposit a thin layer of zinc, a starting layer for the subsequent electroless-nickel deposition. The Ni acts as a wetting material for the solder balls.

Screen printing is used to deposit solder paste on the bond pads. The chip is then 'flipped' onto the flow cell, and the system is heated above the melting temperature of the solder paste, a procedure named *reflow*. The surface tension of the solder paste aligns the chip very accurately with the flow cell. The solder paste should not come in contact with the culture medium and has to be sealed so that the gap between the silicon flow cell and the chip is filled with PDMS or epoxy. A drop of PDMS has been placed in one corner of the active area. Capillary forces drag the liquid PDMS into the gap between the chip and flow cell. All the parts have then been placed in a PMMA chip holder, which has then been screwed onto the PCB board (see Figure 4.15).

A prototype has not yet been produced within the time-frame of this thesis. Two main yield problems remain, the zinc layer and the solder ball size. The zinc layer did not attach well to the bond pads. A reason could be that SiO_2 remaining from the post-processing prevents the zinc from adhering properly. A second difficulty is to accurately and homogeneously screenprint the solder paste on 50 bond pads. When the amount of paste on the different pads varies by more than 10 % or 20 % the smaller solder balls can not form an electrical connection between the chip and the flow cell. The mask for the screen printing featured 150-μm-diameter square openings. Different layouts for the screen printing mask, such as circular or oval openings, could solve this problem.
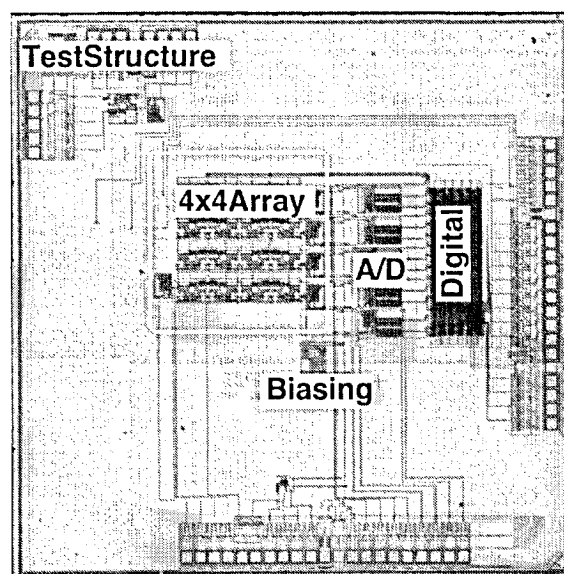
---

[5]www.rohmhaas.com

Figure 4.16: Micrograph of the CMOS chip comprising 16 stimulation and readout electrode.

4.3 Precursor System with 16 Electrodes

A predecessor design of the MEA128 (termed "MEA16") has been presented in [97]. This chip comprises an array of 16 microelectrodes with fully-integrated analog and digital circuitry realized in an industrial CMOS process. Although the function and the basic architecture of the two chips are very similar, their implementation has some key-differences with regard to performance, which are briefly discussed in this section.

4.3.1 System Overview

The 4.4 x 4.4 mm^2 chip shown in Figure 4.16 consists of a 4 x 4 electrode array with integrated reference electrode. Fabrication was performed using an industrial double-polysilicon, triple-metal, 0.6 μm CMOS process at Austriamicrosystems AG, Austria. The electrodes are 40 x 40 μm^2 with a 250 μm pitch. Space between the electrode array and the bond pads has been intentionally left blank for the sealant that isolates the cells from the bond wires. A repeated unit of circuitry associated with each electrode comprises a stimulation buffer and a bandpass filter for readout. The bandpass filter has corner frequencies of 100 Hz and 50 kHz, and a gain of 1'000. The total equivalent input noise in this frequency range is 10 μV$_{RMS}$. The sampling frequency is 20 kHz for each elec-
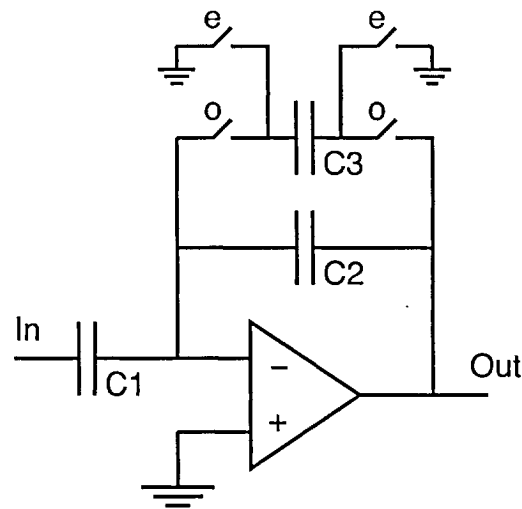
Figure 4.17: Switched-capacitor HPF used in the 16-electrode MEA.

trode and the resolution of the recorded signals is 8 bits given by the resolution of the A/D converter. Stimulation voltages are generated from an 8-bit digital signal and converted to an analog signal at a sampling frequency of 120 kHz. The complete system description is given in the references [98] and [97].

4.3.2 Comparison of the two Designs

The most important difference between the two designs is the shift of the AC-coupling from the second stage in the MEA16 to the first stage in the MEA128. The HPF, which realizes the AC-coupling, is the most sensitive and area consuming structure. In order to relax the noise restrictions for the HPF it would be convenient to first amplify the signal and then to have the HPF in a second stage as it was realized in the MEA16. But, the dc-offset of the metal electrode in solution is too large so that AC-coupling is required before amplification (see also section 3.1.2). Amplification is necessary in order to achieve a sufficient signal-to-noise ratio. A simple example using a passive HPF can illustrate this: A HPF realized with a resistor, R, and a capacitor, C, has a corner frequency of $1/2\pi RC$ and an in-band gain of 1. The noise generated in this passive HPF amounts to kT/C and is inversely proportional to the capacitance. A 1 pF capacitor, e.g., leads to a noise of 64 μV_{RMS}, which is as large as the expected signal amplitudes. An active HPF with amplification is therefore necessary.

The HPF of the MEA128 has been realized as a continuous-time filter in contrast to the switched-capacitor filter implemented in the MEA16 (Figure 4.17). It was not possible to use a switched capacitor technique in the MEA128 given

the required frequency range and the area constraints. The lower corner frequency of the MEA16 was fixed to 100 Hz. In the MEA128, the frequency range is tunable in order to have the flexibility to measure different types of cells and also whole organs or slices. An adjustable corner frequency down to 1 Hz is, therefore, required. This is difficult to realize with the switched-capacitor HPF. In a switched capacitor filter, the resistor, R, is replaced by a capacitor ($C3$ in Figure 4.17) and a number of switches; the equivalent resistance of this structure is $1/f_SC$, where f_S is the sampling frequency. The corner frequency is given by $f_SC3/2\pi C2$. With a sampling frequency of 20 kHz (given by the Nyquist Theorem when the signal bandwidth is 10 kHz) and a feedback capacitor $C2$ of 1 pF, a 37 fF capacitor is needed for $C3$ to realize a corner frequency of 100 Hz. If the corner frequency is lowered to 1 Hz this capacitor is in the range of 1 fF which is too small for a reliable design. Parasitic effects, charge injection and noise would probably make the design unusable. A larger capacitor $C2$ would relax this problem, but since the in-band gain of the structure is given by $C1/C2$ a very large capacitor $C1$ would be needed, which would not be compatible with the given area constraints. Therefore, MOS resistors are used in the MEA128 design to realize the large resistances of several hundred $G\Omega$. Their resistance can be tuned by the gate voltage and is not limited by the area as it is the case for poly-silicon resistors, N-well resistors or switched capacitors at a given frequency.

A fully differential design has been chosen in the MEA128 instead of single-ended design of the MEA16. A fully differential design drastically reduces the risk of interference along the signal paths. Furthermore, common-mode signals of the electrode and the counter electrode are suppressed by the differential design. The sensitivity to leakage currents, especially at the input node of the OTA in the HPF (Figure 4.3) is reduced.

4.4 Future Work and Possible Improvements

One important issue is to increase the number of electrodes and/or the electrode density. Another extension for the MEA128 is the integration of more sensors. A pH-sensor, for example an ISFET, could monitor the cell culture pH [100]. Interdigitated electrodes could serve as a cell attachment sensor [100], closely attached cells indicate a healthy cell culture. Further possible changes and improvements of the system are discussed below.

Circuitry

Offset and noise are among the remaining problems in the MEA128. Both, offset and noise can be reduced by making the electrical units in the readout chain larger, which is hardly possible in our case because of the limited area. Flicker noise could be reduced by using JFETs instead of MOSFETs [59], but this is not standard CMOS technology and, consequently not an option for the technology used here. For offset and low-frequency-noise reduction a second high-pass filter can be used. A second HPF cancels the offset of the first HPF. Additionally, low-frequency noise and drift effects (section 3.1.2) are further suppressed by a 2nd order high-pass filter. The noise specifications are much more relaxed for this second high-pass filter, since the signal is already amplified in the first stage. The filter can therefore be realized as a passive structure that requires a minimum amount of area.

For an increased electrode-density the area of the pixel circuitry has to be reduced. The area of the HPF (Figure 4.5) can be reduced by decreasing its performance. The in-pixel digital circuitry can be made smaller by using area-optimized digital cells or by replacing the flip-flops by SRAMs. The fully-differential amplifier (Figure 4.6) that drives the lines can be replaced by a pseudo-differential amplifier using source followers. In total, a reduction of the pitch from 250 μm to 200 μm should be possible using the same architecture and the same technology. Further area reduction is possible by using a CMOS process with smaller feature size (smaller than 0.6 μm). The gate sizes of the transistors in the analog circuitry part are not automatically reduced minimum feature size is rarely used due to noise and matching requirements. In addition, the capacitors are not scalable using smaller feature-size CMOS technology. However, the area could still be significantly reduced because the routing requires less area. Furthermore, the transistors are smaller since source and drain contacts are smaller. By using, e.g., a 0.35-μm CMOS process the area could be

reduced by probably more than 50 %. Combining both, using advances CMOS technology and further optimizing the analog circuitry could reduce the pitch to maybe 100 μm or even less.

The power consumption of the chip of about 120 mW is rather large. Most of this power can be saved by using more efficient A/D converters. Additionally, the supply voltage can be reduced from 5 V to 3.3 V while preserving the SNR. The power consumption of the in-pixel circuitry can be reduced. For example, the power consumption of the folded-cascode amplifier (Figure 4.4) can also be reduced by using a common-mode feedback based on linear MOS transistors [117], which reduces the number of branches of the amplifier by a factor of 2.

Further possible improvements include the integration of a stimulation buffer that can be used in current- or voltage-simulation mode. One of the problems of a current-stimulation buffer is the quiescent current. The offset is large in these small structures, which leads to current offsets that are different for each electrode. Additionally, electrolysis that can damage the electrode or the cell culture has to be prevented avoided when using current stimulation.

Post-processing

Different electrode materials other than Pt can be used. Pt and Au are the most commonly used materials in the literature, see, e.g., refs. [14,26,51,118]. Other materials include TiN [53] , ITO [2], Palladium [54] or IrO [82]. Open-gate FETs have been used by Fromherz et al. [7]. Recent studies have shown that carbon nanotubes could serve as a substate or electrode material for neuronal networks [119].

Packaging

The number of bond pads of the MEA128 can be reduced. With a redesign of the MEA128, a basic operation with 18 bond pads would be possible instead of the 50 bond connections that are currently needed. The only drawback is the reduced flexibility in using the chip.

Chapter 5

Chip Characterization and Biological Measurements

Measurement results from the MEA128 are presented in this chapter. The first section includes the electrical characterization of the chips with a focus on the in-pixel readout circuitry. The second section presents recordings from spontaneously firing chicken cortical neurons after 56 DIV (days in vitro). Additionally, spontaneous and triggered action potentials from primary neonatal rat cardiomyocytes after 4 and 5 DIV are presented.

5.1 Characterization of the MEA128

5.1.1 Readout Electronics

Electrical tests of the whole array in physiological saline were performed applying a sinusoidal signal (500 Hz, 1 mV_{pp}) to the electrolyte solution via a platinum wire while recording from all sensor electrodes. The signals from 10 randomly chosen electrodes are shown in Figure 5.1. The measured amplitude is about 0.75 mV_{PP}, which is smaller than the stimulation input most likely due to attenuation in the liquid and at the electrode electrolyte interfaces.

The in-band gain and offset of the in-pixel band-pass filter without the third amplification stage has been measured. The midband gain of the HPF and the LPF together is 19.12 dB ± 0.3 (figure 5.2). The discrepancy between the designed gain value of 20 dB and the measured value is most probably caused by fringing fields on the feedback capacitors (C2 in Figure 4.3). The first chip has been
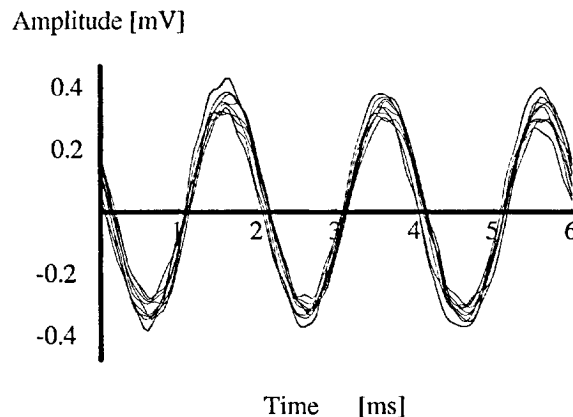
Amplitude [mV]

Time   [ms]

Figure 5.1: Signal output from 10 randomly chosen electrodes upon a sinusoidal signal of 1 mV$_{PP}$ amplitude at 500 Hz. The dc-offset has been removed from these signals.

adjusted to a corner-frequency of 10 Hz. Then, using the same bias voltage, the other three chips showed corner fruequencies between 5 Hz and 13 Hz. The corner-frequency variation within the array can not be characterized with this design, but it can be assumed that it does not exceed the chip-to-chip variation.

The input-referred offset of the filter using the MOS resistor was up to ± 0.5 mV when the filter was set to a corner frequency of 10 Hz. This offset is randomly distributed over the entire array and limits the resolution. A minimal input range of 1 mV, corresponding to a resolution of 4 µV, is needed to keep the signals within the range of the A/D converters. Additionally, this offset depends on the adjustment of the MOS resistor defining the corner frequency. The offset increases for lower frequencies, and below 1 Hz most of the signals are outside the maximum range of the A/D converters. The same problem was observed with the HPF using the MOS diode. In this case the corner frequency is fixed to approximately 1 Hz and offsets of up to 3 mV were measured. The offset is too large to be explained by the mismatch of the input transistors in the OTA in the HPF. We assume that the offset originates from the compensation of leakage currents at the input of the OTA. These leakage currents are compensated by the MOS resistors R in the feedback. A difference in the absolute resistance in the positive and the negative signal path leads to an offset at the output of the filter. The resistance of the MOS resistors depends heavily on the threshold voltage, which is subject to mismatch. As an example, a threshold voltage offset of 10 mV can lead to almost a factor of 2 in the resistance. A leakage current of 5 fA can, therefore, produce 1 mV offset at a resistance of 200 GΩ (8 Hz corner frequency). This offset voltage increases if the filter is set to lower frequencies

since the absolute resistance increases. Reducing this offset is one of the main design improvements for future approaches as will be described in section 4.4.

The input-referred spectrum of all in-pixel readout stages with a sinusoidal input is plotted in Figure 5.3. For this measurement, a sine-wave input with a frequency of 500 Hz and an amplitude of 1 mV_{PP} has been has been applied to the input. The spectrum was recorded using a dynamic signal analyzer (HP3562A). The corner frequencies of the filter were set to 5 Hz and 10 kHz, respectively. A total equivalent-input-referred noise of the in-pixel readout circuitry of 11.7 μV_{RMS} (100 mHz - 100 kHz) was measured. Flicker noise from the OTA (Figure 4.4) and low-frequency noise from the MOS resistors, R, in the HPF (Figure 4.3) are the dominant noise sources. The total equivalent-input-referred noise is reduced to 5.9 μV_{RMS} if the signal bandwidth is reduced to 10 Hz - 100 kHz. However, in the frequency region of 10 Hz and below, the signals of interest are field potentials with larger amplitudes, such as beats from cardiac cultures or ex-vivo organs, see section 5.2.2. An adequate signal-to-noise ratio is therefore preserved even when the filters are adjusted to include the low-frequency region. The minimal corner frequency is about 1 Hz given by the offset limitation as mentioned previously.

The total harmonic distortion (THD) amounts to -54.8 dB considering the first four harmonics. This value is sufficient for a resolution of 8 bits. The common-mode-rejection ratio (CMRR) of the filter is 69 dB as can be seen in Figure 5.4. The power-source rejection ratio (PSRR) is plotted in the same Figure and is approximately 90 dB for V_{DD} and 80 dB for V_{SS}.

5.1.2 Stimulation Electronics

Functionality of the stimulation circuitry has been shown by applying a saw-tooth signal to one of the electrodes, as shown in Figure 5.5 (left). A special packaging scheme has been used for this measurement. First, the bond wires were covered with epoxy, then gold was sputtered over the entire chip surface. All electrodes, including the reference electrode, were electrically shorted by the sputtered gold layer. With this setup signals from the electrodes can be recorded via the bond pad of the reference electrode. The stimulation signal generated on-chip has been recorded by an oscilloscope (Agilent 54641D) connected to the pad of the reference electrode. Digital commands to select one electrode for stimulation and to generate a sawtooth stimulation signal on this electrode were sent to the chip. The sawtooth signal that covered the entire code range (0 .. 255) was repeated at a frequency of 1.8 Hz. The positive and the
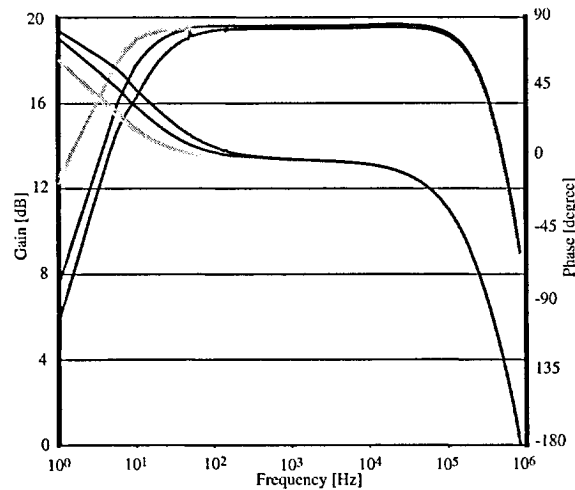
Figure 5.2: Bode-plot measurement of the in-pixel high-pass filter. The graph shows the measurements from four different chips.
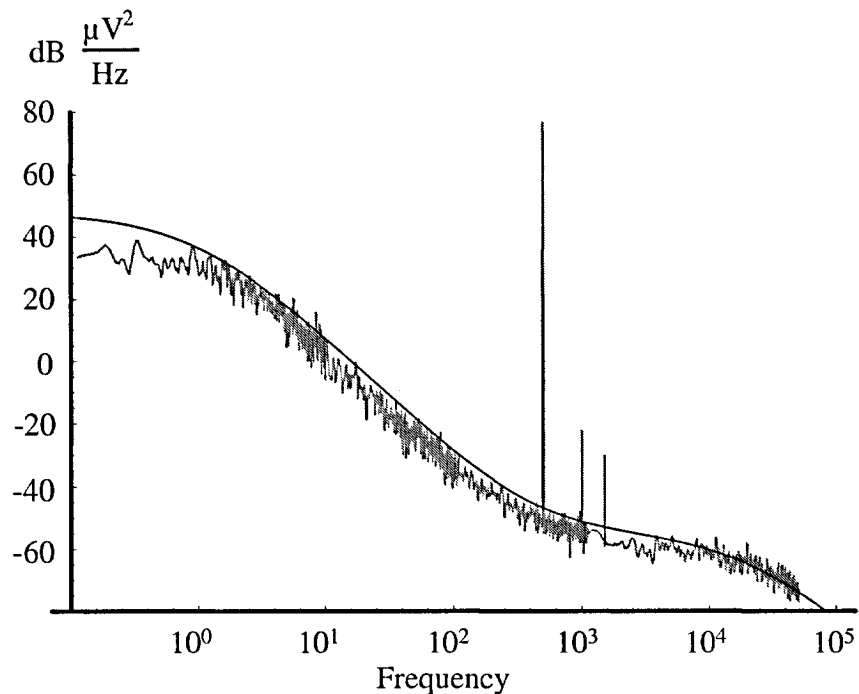

Figure 5.3: Input-referred spectrum of all in-pixel readout stages. The smooth curve represents the input-referred noise derived from equation 4.6. A sine wave ($1mV_{PP}$, 500 Hz) has been applied to measure the harmonic distortion.
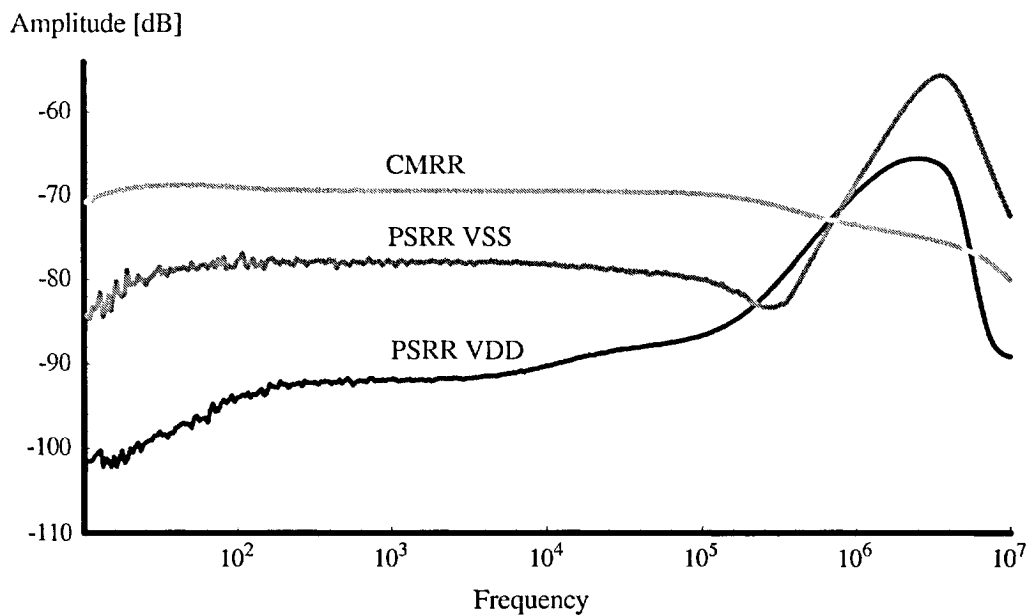
Figure 5.4: CMRR is the common-mode rejection ratio of the in-pixel readout stages. PSRRVSS is the power-source rejection ratio for VSS and PSRRVDD is the power-source rejection ratio for VDD.

negative reference voltages were set to 1.5 V and 3.5 V. The signal recorded from the reference contacts shows good monotony and linearity. This test was repeated for different electrodes (results not shown), in all cases the same result was observed.
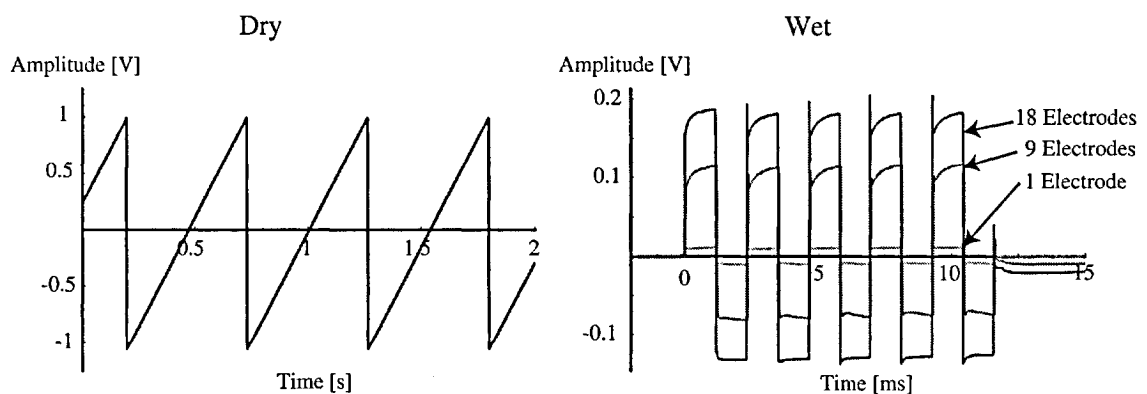

Figure 5.5: Left: Saw-tooth stimulus generated by the on-chip stimulation circuitry. Right: Stimulation pulses measured in the liquid. A number 1, 9 and 18 electrodes was selected for stimulation.

Stimulation with physiological saline on top of the chip has also been performed. For this measurement a normally packaged chip (section 4.2.2) has

been used and the bath has been filled with physiological saline (0.9 % NaCl dissolved in distilled water). The signal was recorded by connecting the oscilloscope to the solution using a Pt-wire. A square-wave stimulus with $1 V_{PP}$ at a frequency of 480 Hz was produced by one or more stimulation electrodes. The recorded signals are shown in Figure 5.5 (right). The number of selected electrodes has been varied from 1 to 18. The recorded signal is about $21 mV_{PP}$ for 1 electrode, $190 mV_{PP}$ for 9 electrodes and $320 mV_{PP}$ for 18 electrodes. Doubling the number of stimulation electrodes approximately doubles the recorded signal amplitude. This can easily be explained. The stimulation electrode and the Pt-wire together with all parasitics build a capacitive divider that is charged and discharged during the stimulation. The larger the number of stimulation electrodes, the smaller the ratio between the total electrode capacitance and the load capacitance. The recorded signal is not perfectly symmetric. This might be caused by the fact that the open-circuit potential (OCP) of the electrode does not coincide with the common-mode voltage of the stimulation circuitry. Although the platinum counter electrode is biased at 2.5 V, the electrode can be at a different potential (see section 3.1.2).

This measurement proves that the stimulation circuitry works in a liquid environment. This is not obvious since interfacing the electrode with a liquid drastically changes the load capacitance for the stimulation amplifier by several orders of magnitude. The results given in table 3.1 show that the capacitance can be well above 1 nF and up to 100 nF. This could eventually lead to instabilities in the stimulation buffer, however, have not been observed.

5.2 Biological Measurements

Signals from neural and cardiac cells cultured on the MEA128 are presented in this section. The biocompatibiltiy of the design is proven by recordings from chicken neurons after as many as 56 DIV. The stimulation capability of the design is demonstrated using cardiac cell cultures.
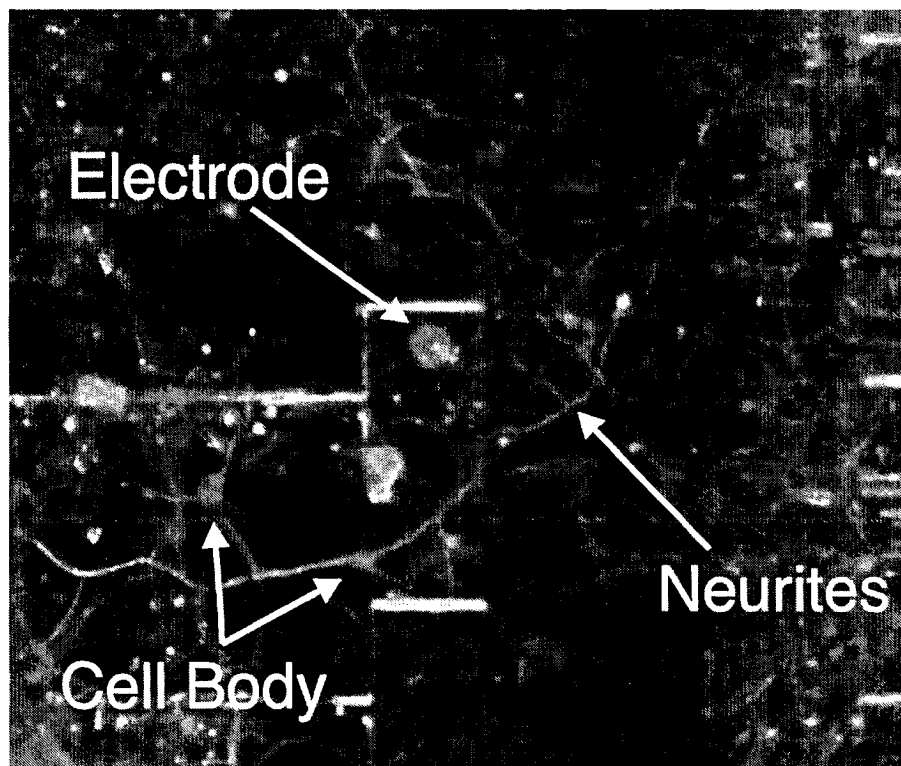

Figure 5.6: Fluorescence image of a neural network grown on the chip and stained after 56 DIV. The circular electrodes can be recognized in the background.

5.2.1 Neuronal Networks

Neural networks originating from dissociated cortical tissue of fertilized chicken eggs (gallus domesticus) were successfully cultured on the chip. The cells were extracted from the chicken egg at embryonic day 10 (E10), mechanically and chemically dissociated and placed on the CMOS chip (see Appendix A.2 for a detailed protocol). The neurons were then maintained in supplemented serum-free Neurobasal medium.

The chips were prepared as follows. Before plating with cells, the CMOS chips were sterilized by immersing them in 70% ethanol at room temperature for 30 minutes. The chips were then rinsed several times with sterile ultrapure water and allowed to dry under a sterile workbench. The electrode area was exposed to a 30 μl drop of sterile-filtered 0.1% polyethyleneimine solution (PEI, Sigma P3143), a cell adhesion mediator, for 1.5 hours before being rinsed several times with cold phosphate-buffered saline (PBS). Ten μl of 50 μg/ml laminin (dissolved in culture medium) were applied to the PEI coating to further promote cell adhesion and neural differentiation.

The fluorescence image in Figure 5.6 shows a neuronal network grown for 56 days on the chip. The large bright spots are cell nuclei, and the bright lines are neurites. The electrode is also visible as a bright round spot. The picture was created by immunostaining the microtubuli-associated protein-2 (MAP2) of the neurons using a fluorescein isothiocyanate (FITC)-conjugated secondary antibody (Appendix A.3). The cells were finally immersed in glycerol and observed by fluorescence microscopy using a Zeiss microscope (Axioskop 2 mot) with digital imaging equipment.

Figure 5.7 shows signals from spontaneously firing cells at 56 DIV. A sterilized elastomer cap with integrated reference electrode was placed over the dish during recording to maintain the cell culture pH for a short period of time. The cut-off frequency of the filters was set to about 10 Hz for the HPF and that of the LPF was set to 5 kHz. The noise level in these recordings is 27 μV_{RMS}. This noise is about twice as large as the measured noise from the circuitry. It has generally been observed that the noise is larger when a cell culture is on top of the electrodes. The signals recorded from 30-μm-diameter electrodes showed signal amplitudes between 500 μV and 700 μV, while signals from 40-μm-diameter electrodes were in the range of 200 μV and 300 μV. The signal amplitudes are seemingly inversely proportional to electrode area. In our case, a twice as large electrode area leads to about half the signal amplitude, which is in agreement with the models used for electrogenic cells on microelectrodes as described in [13,67,68]. The fraction of the electrode area underneath the cell and the fraction that is not covered by the cell constitute, in a first approximation, a capacitive divider, so that the signal amplitude decreases when cells of a certain size are placed on larger electrodes.
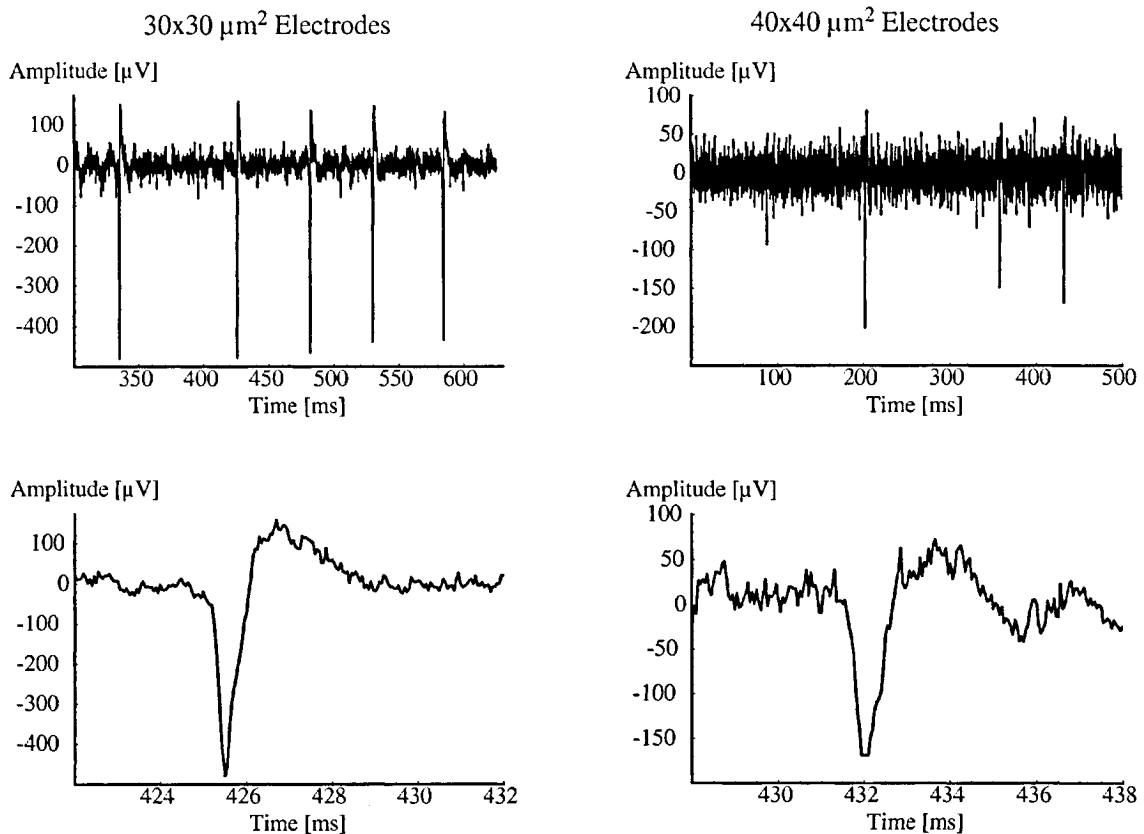
Figure 5.7: These graphs show spontaneously firing chicken neurons at 56 DIV. The signals on the left were measured on circular 30-µm-diameter electrodes, and the signals on the right using 40-µm-diameter electrodes. The lower graphs show one of the spikes at extended time scale.

5.2.2 Cardiac Cells

Cardiac cell cultures

Primary neonatal rat cardiomyocytes (NRC) were successfully cultured on the MEA128. These cells very quickly become spontaneously electrically active, which renders them ideally suitable for device testing. Recordings from the entire network can be obtained after three days in culture, whereas dissociated neurons need to develop and form connections for about two weeks before they show a regular spiking behavior. Additionally, cardiomyocyte signals are larger than those from neurons.

The chips were plated with cardiac cells according to the procedure described in appendix A.4. A recording from spontaneously beating cells on 20-µm-diameter electrodes at 5 DIV is shown in Figure 5.8. In this example, the cells

beat at a rate of about 10 Hz. The right graph shows one of the spikes at an expanded time scale.
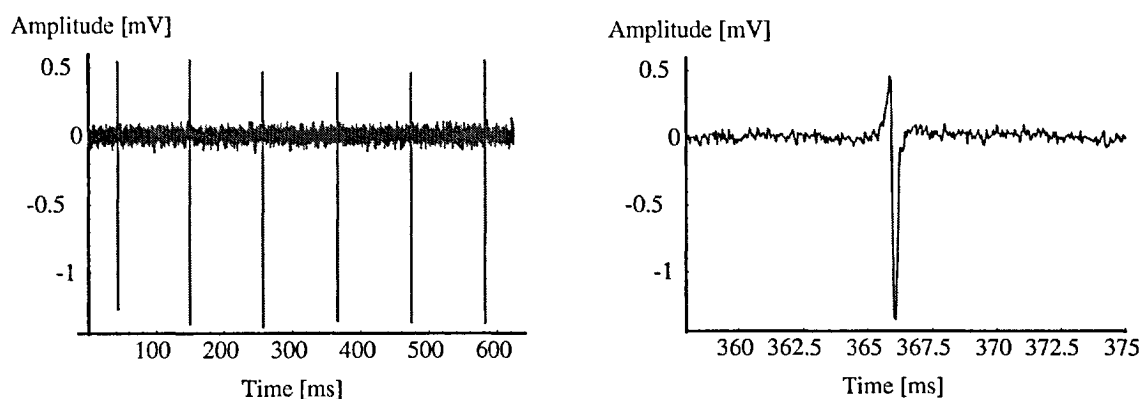
Amplitude [mV]   Amplitude [mV]

Figure 5.8: *Spontaneously active primary cardiomyocytes from neonatal rat at 5 DIV. The right graph shows one of the spikes at an expanded time scale.*

Figure 5.9 shows the recordings from spontaneously beating NRCs at 4 DIV. The plot shows the time dependence of the signals on 64 electrodes where the y-axis represents the electrode number. A simple threshold detection algorithm has been used to detect the spikes, and each event is illustrated as a dot. The resulting vertical lines represent correlated depolarization of the whole cell culture. The beat rate is about 1 Hz. The points in between come from noise in most cases. If one of these vertical lines is expanded one can see that the signal starts at one point and travels across the electrode array within around 11 ms as it is illustrated in Figure 5.10. In Figure 5.10, each plot constitutes the 8 x 8 electrodes at different points in time. The line in each plot represents the location of the depolarization front at each time. The pacemaker (pacemaker cells are described in section 2.1.3) seemingly located in the lower left corner of the culture evokes an action potential at time 0, the wave front of the action potentials then travels across the electrode array. The velocity of the front is about 2 mm in 11 ms, which is 1.8 m/s.
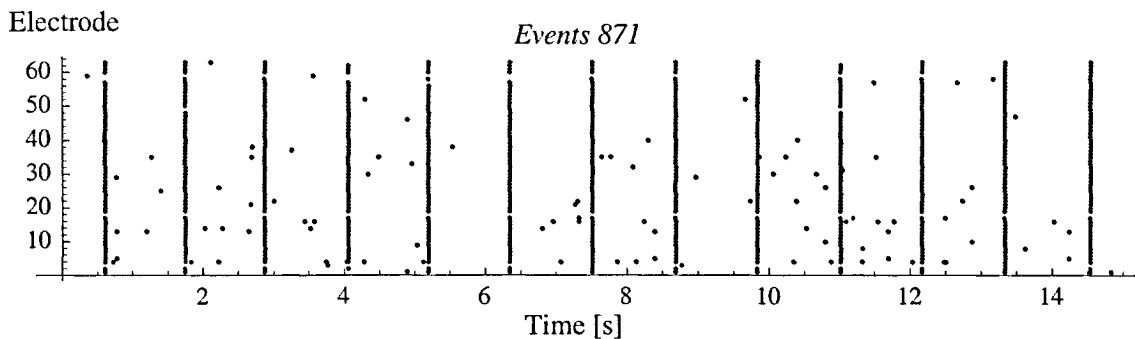
Figure 5.9: Spontaneously beating cardiac cell culture. The y-axis represents the electrode number, only electrodes 1 to 64 are shown here. Each dot represents one spike on the electrode. The resulting vertical lines represent a correlated spiking of the whole culture. The dots in between represent noise in most cases.

Stimulation of a cardiac cell culture

Figure 5.11 shows the recording from a single electrode. The stimulation pulses and the depolarization of the cell culture can be seen in this plot. This electrode was selected for recording, the stimulation was applied to a neighboring electrode. The stimulation pulses appear at all recording electrodes in the array due to crosstalk through the electrolyte. The amplitude of those pulses depends on the distance from the stimulation electrode. Neighboring electrodes of the stimulation electrode may even show saturation effects (not shown).

Twenty stimulation pulses with an amplitude of +/-350 mV at a frequency of 1.5 kHz were used for the measurement in Figure 5.11. Regarding the ability of the stimulation pulses to elicit a depolarization, the influence of the amplitude was observed to be minor compared to the effect of the number of pulses. Ten pulses with an amplitude of up to 1 V were not sufficient to stimulate the cardiomyocytes. A number of 20 pulses at +/-350 mV amplitude often lead to depolarization and 30 pulses reliably elicited a depolarization (in this culture).

The stimulation of a cardiac cell culture is shown in Figure 5.12. The stimulation pulses (indicated by arrows) effectively elicit a depolarization of the cardiac cell tissue. The pacemaker instantaneously synchronizes to the stimulated depolarization, which is indicated by the time interval between the stimulated and the spontaneous depolarization. The time interval of the spontaneous depolarizations is 1.2 ±0.1 s. At the stimulus-induced depolarizations this interval is
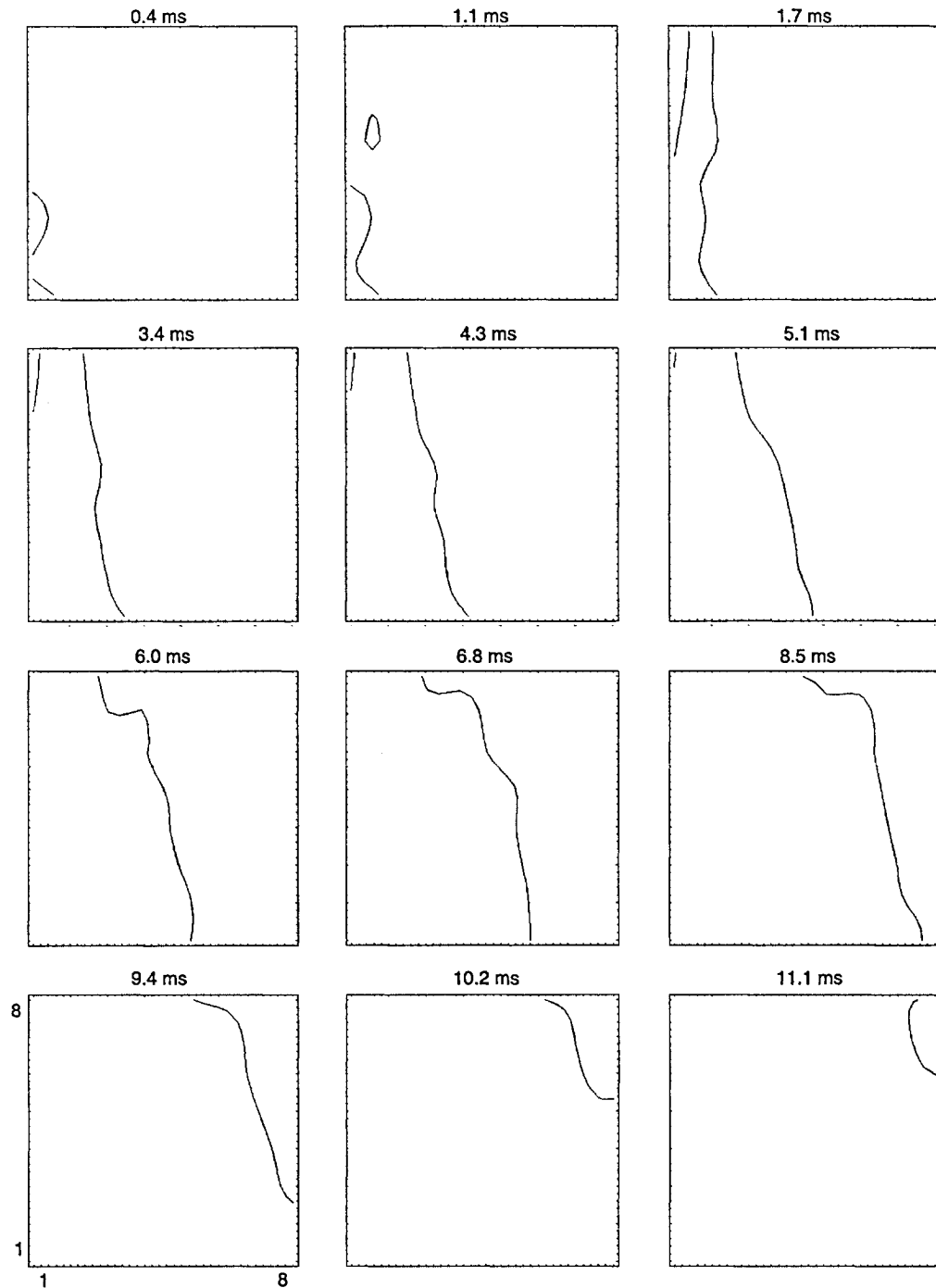
Figure 5.10: Measurement of spontaneously beating rat cardiomyocytes. 8 x 8 electrodes are represented in each square. The line represents the location of the wave front at the given time. A pacemaker seemingly located in the lower left corner of the culture evokes an action potential at time 0, the front of the action potentials travels across the electrode array. This corresponds to a wavefront velocity of 1.8 m/s.

shortened to 0.35 s in the first case and 0.8 s in the second. After the stimulus-induced depolarization the beat rate immediately returns to the normal beat rate triggered by the spontaneous depolarization of the pacemaker.
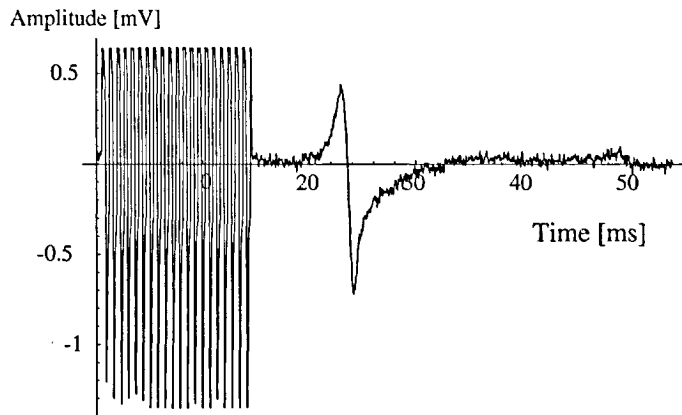

Figure 5.11: Recording from an electrode. Stimulation pulses on a neighboring electrode elicit an action potential.
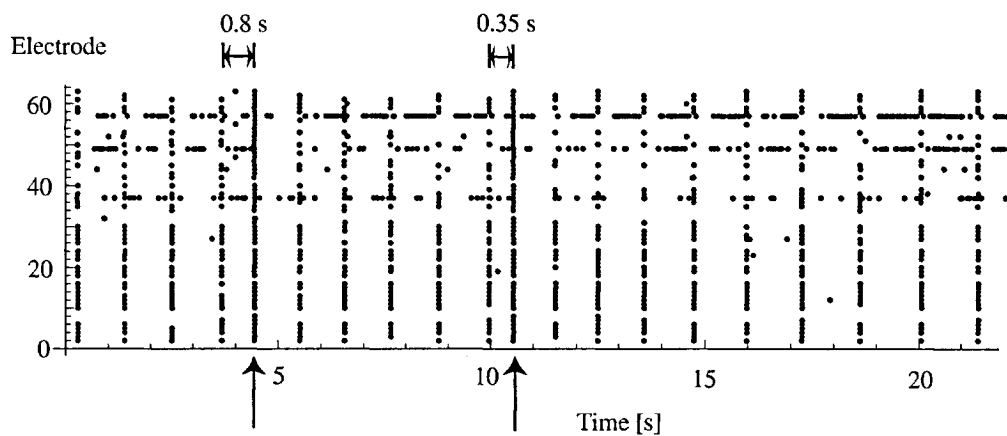
Figure 5.12: Stimulation of a cardiac cell culture. The pacemaker instantaneously synchronizes to the stimulated depolarization as is indicated by the time interval between the stimulated (arrows) and the pace-maker-induced depolarization.

Ex vivo heart on chip

Further tests of the MEA128 were performed with an in situ preparation of cardiomyocytes from fertilized chicken eggs at embryonic day E10. The heart was extracted from the embryo, briefly rinsed with cold Dulbecco's PBS and

directly transferred onto the electrodes of the chip. A reference system was used in order to compare our measurements with standard equipment (MCS system from Multi Channel Systems [57]). A single spike from each of the systems is shown in Figure 5.13. The two waveforms coincide accurately; the P-wave and the T-wave can clearly be seen (the functioning of the heart is described in section 2.1.3). The amplitudes of the heart beats are different since these measurements were performed with organs from different animals.
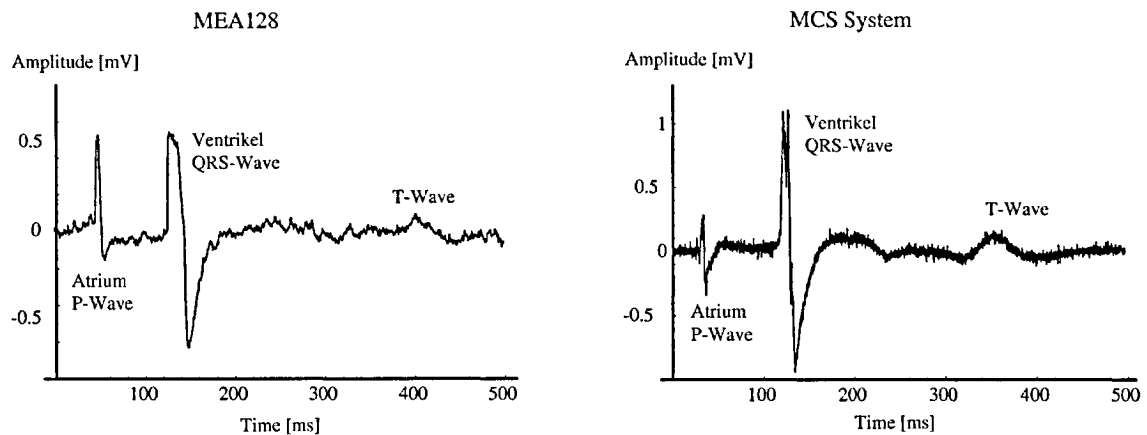

Figure 5.13: Heart spike from an ex-vivo whole-organ measurement. The Figure shows the measurement result from the MEA128 (left) and from the MCS system (right).

Chapter 6

Conclusion and Outlook

6.1 Conclusion

The main topic of this thesis was the development of a monolithic extracellular recording system featuring bidirectional communication (stimulation and recording) to electrogenic cells. To achieve this, a microelectrode array has been fabricated using a standard CMOS process. The system incorporates 128 stimulation- and recording-capable electrodes in an 8x16 array. Post-CMOS processing steps were used to realize biocompatible electrodes and to ensure chip stability in a physiological environment. The system comprises all necessary control and signal-conditioning circuitry as well as on-chip A/D and D/A conversion. An overview of the main characteristics is given in Table 4.1.

The biocompatibiltiy and the functionality of the design have been proven by recordings from chicken neurons after as many as 56 days in culture. Peak-to-peak amplitudes of up to 700 μV_{PP} were recorded. Recordings from cardiac myocytes at 5 days in vitro showed amplitudes of 1.8 mV_{PP}. The stimulation capability of the design has been demonstrated by triggering activity in cell cultures originating from primary neonatal rat cardiomyocytes after 4 days in vitro.

Why CMOS

Throughout this work, the question was often raised why to use CMOS technology. CMOS technology offers some decisive advantages, in particular multiplexers and on-chip electronics, which enable the integration of a large number of transducers and allow for achieving a small system size.

- *Multiplexers* allow the integration of a large number of transducers. A large number of electrodes enables high spatiotemporal resolution, which is required when the behavior of neural networks is studied. Traditional MEAs without multiplexers usually offer 64 electrodes (Table 1.1). The design presented here features 128 electrodes, but the architecture allows for increasing this number to 1024 or even more. In the literature, CMOS-based systems with up to 16'000 electrodes but without individual signal conditioning circuitry have been presented [13].

- *On-chip electronics* allow for the monolithic integration of the complete system on a single chip, which leads to small system dimensions and low power consumption. These are the key requirements for, e.g., implantable devices. Another advantage of on-chip electronics is that the signal can be filtered and amplified close to the signal source, which reduces the risk of signal deterioration along connection lines. On-chip A/D and D/A conversion enable the transfer of robust digital signals on- or off-chip.

A disadvantage of CMOS chips is that silicon is not transparent to visible light. For convenience, biologist generally use inverted microscopes to see the culture from below while working from above. Additionally, the chip can corrode in liquid. Therefore, a good packaging solution is needed to protect the chip and also to prevent the cells from being poisoned by toxic materials, such as Al.

6.2   Outlook

Chip design

One direction of further developments is to increase the number of electrodes. It has to be taken into account that a large number of electrodes leads to a large volume of recording data. For example, 1024 electrodes produce 20 MBytes/s at a sampling rate of 20 kHz. The data storage of long-term recordings, and, especially, subsequent data analysis will be time consuming. Online spike detection is deemed appropriate for long-term recordings from electrode arrays with several hundreds of electrodes. This was the main motivation for using a FPGA in between computer and chip. The FPGA allows for real-time spike detection and transmits only events or event characteristics to the computer, which drastically reduces the amount of data.

Another feasible extension is the integration of more sensors. A pH-sensor, for example an ISFET, could monitor the cell-culture pH [100]. Interdigitated

electrodes could serve as cell attachment sensors with tightly attached cells indicating a healthy cell culture.

Electrode materials different from Pt can be used. Pt and Au are the most commonly used materials in the literature, see refs.. [14,26,51,118]. Alternative materials include TiN [53] , ITO [2], Palladium [54] or IrO [82]. Open-gate FETs as electrodes are used by Fromherz et al. [7]. Recent studies have shown that carbon nanotubes could serve as a substrate or electrode material for neuronal networks [119].

Biological experiments

Recordings of spontaneous and triggered cell activity have been presented in this work, but more sophisticated experiments can be envisioned:

In vitro neural networks grown on a microelectrode array can be used to investigate fundamentals in learning processes on a small and defined neuronal network. Our design allows for fast switching of electrode patterns for stimulation. This offers the possibility to use the neuronal network for solving simple information-processing tasks such as pattern recognition. Additionally, the use of long-term potentiation and depression methods (LTP and LTD [120]) can be used to program a certain functionality in the network. Another interesting experiment is to produce a connectivity map by stimulating one electrode after the other and analyze the respective short-term responses (within approx. 20 ms after stimulation) of the network.

Pharmacologically active agents can be tested on neural and cardiac cell networks. The study of networks is of interest for pharmaceuticals influencing inter-signal transfer, such as neurotransmitters in synapses or connexin proteins during ventricular conduction in cardiac networks. The studies presented in the literature so far are mostly based on the analysis of spontaneous activity of the cell culture. Triggered activity might open new possibilities to test biochemical substances.

Commercial potential

Neuroscientists working with in-vitro networks need larger numbers of electrodes for their research. CMOS microelectrode arrays offer the technology to create a device meeting this requirement. However, the market for such devices is still rather small and mostly confined to academic research.

A large market volume can be expected for MEA-based biosensors for the detection of chemical and biological toxins or for the screening of pharmacologically active compounds. In-vitro networks show remarkable sensitivities to minute chemical dosings and, therefore represent good candidates for accessing dose-related effects of all kinds of chemicals or pharmacologically active substances [2,5,10,11,27,28,30–33,121].

Finally, in the field of neural prosthetics research, microdevices might become a viable approach to recover skeletal muscle function [18,35], to restore visual perception [36] or the auditory system [37,38]. To date the most successful microelectrode-based biohybrid device is the cochlear implant [37,38].

Appendix A

Cell Culture Preparation

A.1 Sterilization of the CMOS chips

CMOS chips were sterilized by incubating them in 70 % ethanol at room temperature for 0.5 hours. The ethanol was discarded and the chip rinsed several times with sterile ultra-pure water (Millipore). The chip was allowed to dry under the sterile workbench. Its electrode area was coated with a 30 µL drop of sterile-filtered 0.1 % polyethyleneimine solution (PEI, Sigma P3143) as a cell adhesion mediator, which was allowed to sit there for 1.5 hours before being rinsed off several times with cold PBS. 10 µl of 50 µg/mL laminin (dissolved in above-mentioned culturing medium) were applied onto the PEI coating to further promote cell adhesion and neural differentiation.

A.2 Neuronal Network Cell Culture

Neural networks originated from dissociated cortical tissue of a fertilized chicken egg (gallus domesticus) at embryonic day 10 (E10). The following cell extraction and culturing protocol was used:

A fertilized chicken egg was incubated in an egg incubator (Grumbach, BSS) for 10 days at 38°C and 60% humidity while being rolled in 6 hour intervals. Before organ extraction, the egg was rinsed with 70% ethanol and opened under a sterile flow bench. All subsequent steps were performed under sterile conditions. The embryo was decapitated and its brain extracted and washed in cold Dulbecco's phosphate buffered saline (PBS without Ca^{2+} and Mg^{2+}, Sigma D8537) containing 1% penicillin/streptomycin (P/S, PAA Laboratories

P11-010). Meninges were removed carefully. The brain parts were transferred to a centrifuge tube containing 5 ml PBS, 10 µg/ml DNase I (Sigma D4263), and 0.04 % trypsin (Sigma T4799). The tissue was tirturated carefully 20 times, incubated for 5 minutes at 37°C, triturated again five times, and incubated for another 5 minutes. To stop the digestive action of trypsin, 2 mL of cold horse serum were added. The suspension was carefully triturated again 10 times, and centrifuged to collect the cell pellet, which was resuspended in 2 mL of cold serum-free Neurobasal culturing medium (Invitrogen 21103 031) supplemented by B27 (Invitrogen 17504-010) and by a cocktail of 0.1% lipid-rich BSA (Sigma F-7175), 0.1% lipid-mixture (Sigma L-0288), 2 mM Ala-Glu (Sigma G8541), 120 µg/ml Na-Pyruvate (Sigma P5280) and 1.5% P/S. A 30 µL drop of cell suspension was placed onto the CMOS to give a final cell density of 900 000 cells per electrode array. The cells were allowed to adhere to the CMOS surface for 20 minutes while being stored in a 5% CO_2 incubator at 37.0°C. Finally, 1 mL of prewarmed culturing medium was added. The chip was returned to the CO_2 incubator after closing it with a gas-permeable lid. After the first seven days, 250 µL of medium were replaced by fresh culturing medium without antibiotics twice a week.

A.3 Fluorescence Imaging of Neuronal Cultures

After 56 DIV, neuronal cultures on CMOS chips were fixed with 4% paraformaldehyde. Non-specific binding sites were blocked with 5% goat serum and 1% BSA in PBS, and the cells were permeabilized with 0.4% Triton X-100 in PBS. The primary anti-MAP2 mouse IgG antibody (Sigma M4403) was incubated with the cells overnight at a dilution of 1:400. After washing three times for 5 min with PBS, the secondary antibody FITC-conjugated anti-mouse IgG (Sigma F0257, 1:40) was applied and incubated for 30 minutes at 37°C. Afterwards, the chips were washed as described above. Cell nuclei were counter stained with the DNA-binding dye DAPI (Sigma D8417). The cells were finally immersed in glycerol and observed by fluorescence microscopy using a Zeiss Axioskop 2 mot microscope with digital imaging equipment.

A.4 Cardiac Cell Culture Protocol

The NRCs were dispersed from the ventricles of 1-3-day-old Sprague-Dawley rats by digestion with collagenase II (Worthington Biochemical Corp., U.S.A.)

and pancreatin (Sigma-Aldrich, U.S.A.). To obtain cultures comprising more than 95% cardiomyocytes, the cell suspensions were separated on a discontinuous Percoll gradient [Sen et al., 1988]. Cells were seeded in plating medium consisting of 68% DMEM (Amimed, Switzerland), 17% Medium M199, 10% horse serum (Life Technologies, USA), 5% fetal calf serum (Life Technologies), 4 mM glutamine (Amimed), and 1% penicillin-streptomycin (Amimed), compare [122]. After 24 h the plating medium was exchanged for maintenance medium, consisting of 78% DMEM (Amimed), 20% Medium M1999 (Amimed), 1% horse serum (Life Technologies), 1% penicillin-streptomycin (Amimed),and 4 mM glutamine, (Amimed). The NRCs were generously provided by Evelyne and Jean-Claude Perriard, Department of Cell Biology, ETHZ.

Bibliography

[1] A. Hodgkin and A. Huxley, "A quantitative description of membrane current and its application to conduction and excitation in nerve," *J. Physiol.*, vol. 117, pp. 500 – 544, 1952.

[2] G. W. Gross, B. K. Rhoades, H. M. E. Azzazy, and W. Ming-Chi, "The use of neuronal networks on multielectrode arrays as biosensors," *Biosens. Bioelectron.*, vol. 10, no. 6-7, pp. 553 – 567, 1995.

[3] Y. Jimbo and H. P. C. Robinson, "Propagation of spontaneous synchronized activity in cortical slice cultures recorded by planar electrode arrays," *Bioelectrochemistry*, vol. 51, no. 2, pp. 107 – 115, 6 2000.

[4] S. Marom and G. Shahaf, "Development, learning and memory in large random networks of cortical neurons: lessons beyond anatomy," *Quarterly Reviews Of Biophysics*, vol. 35, no. 1, pp. 63 – 87, 2 2002.

[5] M. Chiappalone, A. Vato, M. B. Tedesco, M. Marcoli, F. Davide, and S. Martinoia, "Networks of neurons coupled to microelectrode arrays: a neuronal sensory system for pharmacological applications," *Biosensors Bioelectronics*, vol. 18, pp. 627 – 634, 2003.

[6] W. L. C. Rutten, "Selective electrical interfaces with the nervous system," *Annual Review Of Biomedical Engineering*, vol. 4, pp. 407 – 452, 2002.

[7] P. Fromherz, "Electrical interfacing of nerve cells and semiconductor chips," *Chemphyschem*, vol. 3, pp. 276 – 284, 2002.

[8] S. Fennrich, H. Stier, K. J. Foehr, D. Ray, J. F. G. Egea, and B. Schlosshauer, "Organotypic rat brain culture as in vivo-like model system," *Methods in Cell Science*, vol. 18, pp. 283 – 291, 1996.

[9] D. A. Stenger, G. W. Gross, E. W. Keefer, K. M.Shaffer, J. D. Andreadis, W. Ma, and J. J. Pancrazio, "Detection of physiologically active compounds using cell-based biosensors," *TRENDS in Biotechnology*, vol. 19, no. 8, pp. 304 – 309, 2001.

[10] A. Stett, U. Egert, E. Guenther, F. Hofmann, T. Meyer, W. Nisch, and H. Haemmerle, "Biological application of microelectrode arrays in drug discovery and basic research," *Anal Bioanal Chem*, vol. 377, pp. 486 – 495, 2003.

[11] T. Meyer, C. Leisgen, B. Gonser, and E. Guenther, "Qt-screen: High-throughput cardiac safety pharmacology by extracellular electrophysiology on primary cardiac myocytes," *ASSAY and Drug Development Technologies*, vol. 2, no. 5, pp. 507 – 515, 2004.

[12] G. T. A. Kovacs, "Electronic sensors with living cellular components," *Proc. IEEE*, vol. 91, no. 6, pp. 915 – 929, 2003.

[13] B. Eversmann, M. Jenkner, F. Hofmann, C. Paulus, R. Brederlow, B. Holzapfl, P. Fromherz, M. Merz, M. Brenner, M. Schreiter, R. Gabl, K. Plehnert, M. Steinhauser, G. Eckstein, D. Schmitt-Landsiedel, and R. Thewes, "A 128 x 128 CMOS biosensor array for extracellular recording of neural activity," *IEEE J. Solid-State Circuits*, vol. 38, no. 12, pp. 2306 – 2317, 2003.

[14] L. Berdondini, P. V. der Wal, O. Guenat, N. de Rooij, M. Koudelka-Hep, P. Seitz, R. Kaufmann, P. Metzler, N. Blanc, and S. Rohr, "High-density electrode array for imaging in vitro electrophysiological activity," *Biosensors Bioelectronics*, vol. 21, pp. 167 – 174, 2005.

[15] W. H. van der Schalie, H. S. Gardner, J. A. Bantle, C. T. de Rosa R. A. Finch, J. S. Reif, R. H. Reuter, L. C. Backer, J. Burger, L. C. Folmar, and W. S. Stokes, "Animals as sentinels of human health hazards of environmental chemicals," *Environmental Health Perspectives*, vol. 107, no. 4, pp. 309 – 315, 1999.

[16] G. E. Fabiani, D. J. McFarland, J. R. Wolpaw, and G. Pfurtscheller, "Conversion of eeg activity into cursor movement by a brain computer interface (bci)," *IEEE Transactions on Neural Systems and Rehabilitation Engeneering*, vol. 12, no. 3, pp. 331 – 339, 2004.

[17] M. P., "A role for sleep in the processing of memory traces. contribution of functional neuroimaging in humans," *Bull Mem Acad R Med Belg.*, vol. 159, no. 2, pp. 167 – 170, 2004.

[18] M. A. L. Nicolelis, "Brain machine interfaces to restore motor function and probe neural circuits," *Nature Reviews Neuroscience*, vol. 4, pp. 417 – 421, 2003.

[19] K. D. Wise, D. J. Anderson, J. F. Hetke, D. R. Kipke, and K. Najafi, "Wireless implantable microsystems: high-density electronic interfaces to the nervous system," *Proceedings of the IEEE*, vol. 92, no. 1, pp. 76 – 97, 2004.

[20] W. Singer, "Time as coding space?" *Current Opinion in Neurobiology*, vol. 9, no. 2, pp. 189 – 194, 1999.

[21] T. B. DeMarse, D. A. Wagenaar, W. Blau, and S. M. Potter, "The neurally controlled animat: Biological brains acting with simulated bodies," *Autonomous Robots*, vol. 11, pp. 305 – 310, 2001.

[22] S. Nirenberg and P. E. Latham, "Decoding neuronal spike trains: How important are correlations?" *PNAS*, vol. 100, no. 12, pp. 7348 – 7353, 2003.

[23] M. E. Ruaro, P. Bonifazi, and V. Torre, "Toward the neurocomputer: Image processing and pattern recognition with neuronal cultures," *Biosensors Bioelectronics*, vol. 52, no. 3, pp. 371 – 384, 2005.

[24] G. W. Gross, A. Harsch, B. K. Rhoades, and W. Goepel, "Odor, drug and toxin analysis with neuronal networks in witro: extracellular array recording of network responses," *Biosensors and Bioelectronics*, vol. 12, no. 5, pp. 373 – 393, 1997.

[25] J. J. Pancrazio, J. P. P. Bey, D. S. Cuttino, J. K. Kusel, D. A. Borkholder, K. M. Shaffer, G. T. A. Kovacs, and D. A. Stenger, "Portable cell-based biosensor system for toxin detection," *Sensors and Actuators B: Chemical*, vol. 53, no. 3, pp. 179 – 185, 12 1998.

[26] J. J. Pancrazio, J. P. Whelan, D. A. Borkholder, W. Ma, and D. A. Stenger, "Development and application of cell-based biodensors," *Annals of Biomedical Engeneering*, vol. 27, pp. 697 – 711, 1999.

[27] S. I. Morefield, E. W. Keefer, K. D. Chapman, and G. W. Gross, "Drug evaluations using neuronal networks cultured on microelectrode arrays," *Biosens. Bioelectron.*, vol. 15, no. 7-8, pp. 383 – 396, 10 2000.

[28] E. W. Keefer, A. Gramowski, D. A. Stenger, J. J. Pancrazio, and G. W. Gross, "Characterization of acute neurotoxic effects of trimethylolpropane phosphate via neuronal network biosensors," *Biosens. Bioelectron.*, vol. 16, no. 7-8, pp. 513 – 525, 9 2001.

[29] A. G. Kleber and Y. Rudy, "Basic mechanisms of cardiac impulse propagation and associated arrhythmias," *Physiol. Rev.*, vol. 84, pp. 431 – 488, 2003.

[30] FDA, *ICH S7B Guideline: The Nonclinical Evaluation of the Potential for Delayed Ventricular Repolarization (QT Interval Prolongation) by Human Pharmaceuticals.* Rockville MD 20857-0001, USA: U. S. Food and Drug Administration, 2004.

[31] J. J. Pancrazio, J. P. P. Bey, A. Loloee, M. a. C. H.-C. SubbaRao, H. L. L, G. W. Milton, D. A. Borkholder, and A. K. G. T, "Description and demonstration of a CMOS amplifier-based-system with measurement and stimulation capability for bioelectrical signal transduction," *Biosens. Bioelectron.*, vol. 13, no. 9, pp. 971 – 979, 10 1998.

[32] B. D. DeBusschere and G. T. A. Kovacs, "Portable cell-based biosensor system using integrated CMOS cell-cartridges," *Biosens. Bioelectron.*, vol. 16, no. 7-8, pp. 543 – 556, 9 2001.

[33] K. H. Gilchrist, V. N. Barker, L. E. Fletcher, B. D. DeBusschere, P. Ghanouni, L. Giovangrandi, and G. T. A. Kovacs, "General purpose, field-portable cell-based biosensor platform," *Biosens. Bioelectron.*, vol. 16, no. 7-8, pp. 557 – 564, 9 2001.

[34] A. Gramowski, K. Juegelt, D. G. Weiss, and G. W. Gross, "Substance identification by quantitative characterization of oscillatory activity in murine spinal cord networks on microelectrode arrays," *European Journal of Neuroscience*, vol. 19, pp. 2815 – 2825, 2004.

[35] T. Stieglitz, H. H. Ruf, M. Gross, M. Schuettler, and J. U. Meyer, "A biohybrid system to interface peripheral nerves after traumatic lesions: design of a high channel sieve electrode," *Biosensors Bioelectronics*, vol. 17, pp. 685 – 696, 2002.

[36] E. Zrenner, "Will retinal implants restore vision," *Science*, vol. 295, pp. 1022 – 1025, 2002.

[37] G. E. Loeb, "Cochlear prostethics," *Annu. Rev. Neuroscience*, vol. 13, pp. 357 – 371, 1990.

[38] J. P. Rauschecker and R. V. Shannon, "Sending sound to the brain," *Science*, vol. 295, pp. 1025 – 1028, 2002.

[39] A. Mannard, R. B. Stein, and D. Charles, "Regeneration electrode units: Implants for recording from single peripheral nerve fibers in freely moving animals," *Science*, vol. 183, no. 4124, pp. 547 – 549, 1974.

[40] D. J. Edell, R. Riso, L. Devaney, B. Larsen, M. Koris, and D. DeLorenzo, "Intraneural microstimulation for enhanced prosthetic control using a peripheral nerve interface," in *Proc. IEEE Int. Conf. of the EMBS*, St. Louis, Missouri, 1986, pp. 337 – 338.

[41] G. T. A. Kovacs, C. W. Storment, M. Halks-Miller, C. R. Belczynski, C. C. D. Santina, E. R. Lewis, and N. I. Maluf, "Silicon-substrate microelectrode arrays for parallel recording of neural activity in peripheral and cranial nerves," *Biomedical Engineering, IEEE Transactions on*, vol. 41, no. 6, pp. 567 – 577, 1994.

[42] T. Kawada, C. Yheng, S. Tanabe, T. Uemura, K. Sunagawa, and M. Sugimachi, "A sieve electrode as a potential automatic neural interface for bionic medicine," *Eng. Med and Bio Society IEEE Annual Int. Conf.*, vol. 2, pp. 4318 – 4321, 2004.

[43] K. Najafi and K. D. Wise, "An implantable multielectrode array with on-chip signal processing," *IEEE J. Solid-State Circuits*, vol. 21, no. 6, pp. 1035 – 1044, 1986.

[44] T. Akin, K. Najafi, and R. M. Bradley, "A wireless implantable multi-channel digital neural recording system for a micromachined sieve electrode," *IEEE J. Solid-State Circuits*, vol. 33, no. 1, pp. 109 – 118, 1998.

[45] P. Connolly, P. Clark, A. S. G. Curtis, J. A. T. Dow, and C. D. W. Wilkinson, "An extracellular microelectrode array for monitoring electrogenic cells in culture," *Biosens. Bioelectron.*, vol. 5, no. 3, pp. 223 – 234, 1990.

[46] J. Ji and K. D. Wise, "An implantable CMOS circuit interface for multiplexed multielectrode recording arrays," *IEEE J. Solid-State Circuits*, vol. 27, pp. 433 – 443, 1992.

[47] G. W. Gross, B. K. Rhoades, D. L. Reust, and F. U. Schwalm, "Stimulation of monolayer networks in culture through thin-film indium-tin oxide recording electrodes," *Journal of Neuroscience Methods*, vol. 50, no. 2, pp. 131 – 143, 11 1993.

[48] H. Haemmerle, U. Egert, A. Mohr, and W. Nisch, "Extracellular recording in neuronal networks with substrate integrated microelectrode arrays," *Biosensors Bioelectronics*, vol. 9, no. 9-10, pp. 691 – 696, 1994.

[49] U. Egert, B. Schlosshauer, S. Fennrich, W. Nisch, M. Fejtl, T. Knott, T. Muller, and H. Hammerle, "A novel organotypic long-term culture of the rat hippocampus on substrate-integrated multielectrode arrays," *Brain Research Protocols*, vol. 2, no. 4, pp. 229 – 242, 6 1998.

[50] V. Bucher, M. Graf, M. Stelzle, and W. Nisch, "Low-impedance thin-film polycrystalline silicon microelectrodes for extracellular stimulation and recording," *Biosens. Bioelectron.*, vol. 14, no. 7, pp. 639 – 649, 10 1999.

[51] M. P. Maher, J. Pine, J. Wright, and Y.-C. Tai, "The neurochip: a new multielectrode device for stimulating and recording from cultured neurons," *Journal of Neuroscience Methods*, vol. 87, no. 1, pp. 45 – 56, 2 1999.

[52] S. M. Potter, "Distributed processing in cultured neuronal networks," *Progress in Brain Research*, vol. 130, pp. 49 – 53, 2001.

[53] M. O. Heuschkel, M. Fejtl, M. Raggenbass, D. Bertrand, and P. Renaud, "A three-dimensional multi-electrode array for multi-site stimulation and recording in acute brain slices," *Journal of Neuroscience Methods*, vol. 114, no. 2, pp. 135 – 148, 3 2002.

[54] W. Baumann, E. Schreiber, G. Krause, S. Stuwe, A. Podssun, S. Homma, H. Anlaufa, R. Rosner, I. Freund, and M. Lehmann, "Multiparametric neurosensor microchip," *Proceedings Eurosensors XVI, Prag*, 2002.

[55] Y. Jimbo, N. Kasai, K. Torimitsu, T. Tateno, and H. P. C. Robinson, "A system for MEA-based multisite stimulation," *Biomedical Engineering, IEEE Transactions on*, vol. 50, no. 2, pp. 241 – 248, 2003.

[56] J. van Pelt, P. S. Wolters, M. A. Corner, W. L. C. Rutten, and G. J. A. Ramakers, "Long-term characterization of firing dynamics of spontaneous bursts in cultured neural networks," *Biomedical Engeneering, IEEE Trans on*, vol. 51, no. 11, pp. 2051 – 2062, 2004.

[57] MCS, "Multi Channel Systems GmbH," http://www.multichannelsystems.com.

[58] M. Jenkner, B. Muller, and P. Fromherz, "Interfacing a silicon chip to pairs of snail neurons connected by electrical synapses," *Biological Cybernetics*, vol. 84, no. 4, pp. 239 – 249, 4 2001.

[59] M. Voelker and P. Fromherz, "Signal transmission from individual mammalian nerve cell to field-effect transistor," *Small Journal.*, vol. 1, pp. 1–4, 2005.

[60] M. Merz and P. Fromherz, "Silicon chip interfaced with a geometrically defined net of snail neurons," *Advanced Functional Materials*, vol. 15, no. 5, pp. 739 – 744, 2005.

[61] C. Sprossler, M. Denyer, S. Britland, W. Knoll, and A. Offenhausser, "Electrical recordings from rat cardiac muscle cells using field-effect transistors," *Phys. Rev. E*, vol. 60, pp. 2171 – 2176, 1999.

[62] A. Offenhaeuser and W. Koll, "Cell transistor hybrid systems and their potential applications," *Trends in Biotechnology*, pp. 62 – 66, 2001.

[63] L. Berdondini, T. Overstolz, N. F. de Rooij, M. Koudelka-Hep, S. Martinoia, P. Seitz, M. Wany, and N. Blanc, "High resolution electrophysiological activity imaging of in-vitro neuronal networks," in *Proc. IEEE-EMB Int. Microtechnologies in Medicine and Biology Conf.*, Madison, Wisconsin, 2002, pp. 241 – 244.

[64] B. Eversmann, M. Jenkner, C. Paulus, F. Hofmann, R. Brederlow, B. Holzapfl, P. Fromherz, M. Brenner, M. Schreiter, R. Gabl, K. Plehnert, M. Steinhauser, G. Eckstein, D. Schmitt-Landsiedel, and R. Thewes, "A 128 x 128 CMOS bio-sensor array for extracellular recording of neural activity," in *IEEE Int. Solid-State Circuits Conf. Dig. Tech. Papers*, San Francisco, California, 2003, pp. 222 – 489 vol.1.

[65] M. Jenkner, M. Tartagni, A. Hierlemann, and R. Thewes, "Cell-based CMOS sensor and actuator arrays," *Solid-State Circuits, IEEE Journal of*, vol. 39, no. 12, pp. 2431 – 2437, 2004.

[66] A. Lambacher, M. Jenkner, M. Merz, B. Eversmann, R. A. Kaul, F. Hofmann, R. Thewes, and P. Fromherz, "Electrical imaging of neuronal activity by multi-transistor-array (MTA) recording at 7.8 mu m resolution," *Applied Physics A-Materials Science & Processing*, vol. 79, pp. 1607 – 1611, 2004.

[67] J. R. Buitenweg, W. L. C. Rutten, and E. Marani, "Geometry-based finite-element modeling of the electrical contact between a cultured neuron and a microelectrode," *IEEE Trans. Biomed. Eng.*, vol. 50, no. 4, pp. 501 – 509, 2003.

[68] X. Huang, D. Nguyen, D. W. Greve, and M. M. Domach, "Simulation of microelectrode impedance changes due to cell growth," *IEEE Sensors J.*, vol. 4, no. 5, pp. 576 – 583, 2004.

[69] W. Franks, *Towards Monolithic CMOS Cell-based Biosensors*. Zurich: Ph.D. Thesis, No. 15990, ETH Zurich, 2005.

[70] D. Johnston and S. M. S. Wu, *Foundations of cellular neurophysiology*. Massachusetts Institute of Technology, 1995.

[71] E. R. Kandel, J. H. Schwartz, and T. M. Jessell, *Principles of Neural Science*. McGraw-Hill Companies, 2000.

[72] H. Lodish, A. Berk, S. L. Zipursky, P. Matsudaira, D. Baltimore, and J. E. Darnell, *Molecular Cell Biology*. 41 Madison Avenue, New York, New York 10010: W. H. Freeman and Company, 2000.

[73] M. Tsacopoulos and P. J. Magistretti, "Metabolic coupling between glia and neurons," *J. of Neuroscience*, vol. 16, no. 3, pp. 877 – 885, 1996.

[74] L. R. Watkins and S. F. Maier, "Glia: A novel drug discovery target for clinical pain," *Nature Reviews*, vol. 2, pp. 973–87, 2003.

[75] M. A. Harrison, I. F. Rae, and A. Harris, *General techniques of cell culture*. Cambridge University Press, 1997.

[76] E. Neher and B. Sakmann, "Single-channel currents recorded from membrane of denervated frog muscle fibres," *Nature*, vol. 260, pp. 799 – 802, 1976.

[77] K. Cole, "Dynamic electrical characteristics of the squid axon membrane," *Arch. Sci. physiol.*, vol. 3, pp. 253 – 258, 1949.

[78] R. Caton, "The electric currents of the brain," *Br. Med. J.*, vol. 2, p. 278, 1875.

[79] K. D. Wise and J. B. Angeli, "A microprobe with integrated amplifiers for neurophysiology," *ISSCC, Proc. IEEE Int. Solid-State Circuits Conference*, pp. 100 – 101, 1971.

[80] C. A. Thomas, P. A. Springer, G. E. Loeb, Y. Berwald-Netter, and L. M. Okum, "A miniature microelectrode array to monitor the bioelectric activity of cultured cells," *Experimental Cell Research*, vol. 74, pp. 61 – 66, 1972.

[81] R. C. Gesteland, B. Howland, J. Y. Lettvin, and W. H. Pitts, "Comments on microelectrodes," *Proc. IRE*, vol. 47, pp. 1856–62, 1959.

[82] J. D. Weiland, D. J. Anderson, and M. S. Humayun, "In vitro electrical properties for iridium oxide versus titanium nitride stimulating electrodes," *IEEE Trans. Biomed. Eng.*, vol. 49, no. 12, pp. 1574 – 1579, 2002.

[83] J. R. Buitenweg, W. L. C. Rutten, and E. Marani, "Modeled channel distributions explain extracellular recordings from cultured neurons sealed to microelectrodes," *IEEE Trans. Biomed. Eng.*, vol. 49, no. 12, pp. 1580 – 1590, 2002.

[84] F. Heer, S. Hafizovic, W. Franks, T. Ugniwenko, A. Blau, C. Ziegler, and A. Hierlemann, "Fully integrated 128-electrode CMOS chip for bidirectional interaction with electrogenic cells," in *Eurosensors XIX*, Barcelona, Spain, 2005.

[85] F. Heer, S. Hafizovic, W. Franks, T. Ugniwenko, A. Blau, C. Ziegler, and Hierlemann, "CMOS microelectrode array for bidirectional interaction with neuronal networks," in *Proc. Eur. Solid-State Circuits Conf.*, Grenoble, France, 2005, pp. 335 – 338.

[86] D. A. Stenger and T. M. McKenna, *Enabling Technologies for Cultured Neural Networks.* San Diego: Academic Press, 1994.

[87] E. T. McAdams, A. Lackermeier, J. A. McLaughlin, D. Macken, and J. Jossinet, "The linear and non-linear electrical properties of the electrode-electrolyte interface," *Biosens. Bioelectron.*, vol. 10, no. 1-2, pp. 67 – 74, 1995.

[88] W. Franks, I. Schenker, P. Schmutz, and A. Hierlemann, "Impedance characterization and modeling of electrodes for biomedical applications," *Biomedical Engeneering, IEEE Trans on*, vol. 52, no. 7, pp. 1295 – 1302, 2005.

[89] P. W. Atkins, *Physical Chemistry*. Oxford University Press, 1998.

[90] A. J. Bard and L. R. Faulkner, *Electrochemical Methods*. John Wiley and Sons, Inc., 2001.

[91] R. W. de Boer and A. van Oosterom, "Electrical properties of platinum electrodes: impedance measurements and time-domain analysis," *Medical & Biological Engineering & Computing*, vol. 16, no. 1, pp. 1 – 10, 1 1978.

[92] H. P. Schwan, "Linear and nonlinear properties of platinum electrode polarisation iii: equivalense of frequency- and time-domain behaviour," *Med. & Biol. Eng. & Comp.*, vol. 23, pp. 28–32, 1985.

[93] H. Fischler and H. P. Schwan, "Polarisation impedance of pacemaker electrodes: in vitro studies simulating practical operation," *Med. and Biol. Eng. and Comput.*, vol. 19, pp. 579 – 588, 1981.

[94] J. R. Buitenweg, W. L. C. Rutten, and E. Marani, "Extracellular stimulation window explained by a geometry-based model of the Neuron-electrode contact," *IEEE Trans. Biomed. Eng.*, vol. 49, no. 12, pp. 1591 – 1599, 2002.

[95] K. Hladky and J. L. Dawson, "The measurement of corrosion using electrochemical 1/f noise," *Corrosion Science*, vol. 22, no. 3, pp. 231 – 237, 1982.

[96] A. Hassibi, R. Navid, R. W. Dutton, and T. H. Lee, "Comprehensive study of noise processes in electrode electrolyte interfaces," *J. Appl. Phys.*, vol. 96, no. 2, pp. 1074 – 1082, 2004.

[97] F. Heer, W. Franks, A. Blau, S. Taschini, C. Ziegler, A. Hierlemann, and H. Baltes, "CMOS microelectrode array for the monitoring of electrogenic cells," *Biosensors Bioelectronics*, vol. 20, no. 2, pp. 358 – 366, 9 2004.

[98] W. Franks, F. Heer, I. McKay, S. Taschini, R. Sunier, C. Hagleitner, A. Hierlemann, and H. Baltes, "CMOS monolithic microelectrode array

for stimulation and recording of natural neural networks," in *Proc. IEEE Transducers Conf.*, vol. 2, Boston, USA, 2003, pp. 963 – 966 vol.2.

[99] A. Stett, V. Bucher, C. Burkhardt, U. Weber, and W. Nisch, "Patch clamping of primary cardiac cells with micro-openings in polyimide films," *Med. Biol. Eng. Comp.*, vol. 51, pp. 233 – 240, 2003.

[100] W. H. Baumann, E. Schreiber, G. Krause, A. Podssun, S. Homma, R. Schrott, R. Ehret, I. Freund, and M. Lehmann, "Cell monitoring system with multiparametric CMOS sensorchips," μTAS, vol. 2, pp. 554 – 556, 2004.

[101] R. R. Harrison and C. Charles, "A low-power low-noise CMOS amplifier for neural recording applications," *IEEE J. Solid-State Circuits*, vol. 38, no. 16, pp. 958 – 965, 2003.

[102] J. Pelt, P. S. Wolters, M. A. Corner, W. L. C. Rutten, and G. J. A. Ramakers, "Long-term characterization of firing dynamics of spontaneous bursts in cultured neural networks," *IEEE Trans. Biomed. Eng.*, vol. 51, no. 11, pp. 2051 – 2062, 2004.

[103] Y. Papananos, T. Gergantas, and Y. Tsividis, "Design considerations and implementation of very low frequency continuous-time CMOS monolithic filters," *IEE Proc.-Circuits Devices Syst.*, vol. 144, no. 2, pp. 68 – 74, 1997.

[104] T. Delbruck and C. A. Mead, "Adaptive photoreceptor with wide dynamic range," *Proc. IEEE Int. Circuits and Systems Symposium*, vol. 4, pp. 339 – 342, 1994.

[105] J. J. F. Rijns, "CMOS low-distortion high-frequency variable-gain amplifier," *IEEE J. Solid-State Circuits*, vol. 31, no. 7, pp. 1029 – 1034, 1996.

[106] T. Hashimoto, C. M. Elder, and J. L. Vitek, "A template subtraction method for stimulus artifact removal in high-frequency deep brain stimulation," *J. Neurosci. Meth.*, vol. 113, pp. 181 – 186, 2002.

[107] D. A. Wagenaar and S. M. Potter, "Real-time multi-channel stimulus artifact suppression by local curve fitting," *J. Neurosci. Meth.*, vol. 120, pp. 113 – 120, 2002.

[108] J. W. Gnadt, S. D. Echols, A. Yildirim, H. Zhang, and K. Paul, "Spectral cancellation of microstimulation artifact for simultaneous neural recording in situ," *IEEE Trans. Bio-Med. Eng.*, vol. 50, no. 10, pp. 1129 – 1135, 2003.

[109] K. Martin, L. Ozcolak, Y. S. Lee, and G. C. Temes, "Differential switched-capacitor amplifier," *IEEE J. Solid-State Circuits*, vol. 22, no. 1, pp. 104 – 106, 1987.

[110] P. Bonifazi and P. Fromherz, "Silicon chip for electronic communication between nerve cells by non-invasive interfacing and analog-digital processing," *Adv. Mater.*, vol. 14, no. 17, pp. 1190 – 1193, 2002.

[111] J. B. Bates and Y. T. Chu, "Electrode-electrolyte interface impedance: experiments and model," *Annals Of Biomedical Engineering*, vol. 20, no. 3, pp. 349 – 362, 1992.

[112] D. F. Hilbiber, "A new semiconductor voltage standard," *IEEE Int. Solid-State Circuits Conf. Dig. Tech. Papers*, pp. 32 – 33, 1964.

[113] R. J. Widlar, "New developments in ic voltage regulators," *IEEE J. Solid-State Circuits*, vol. 6, pp. 2 – 7, 1971.

[114] A. M. Feltham and M. Spiro, "Platinized platinum electrodes," *Chemical Reviews*, vol. 2, pp. 177 – 194, 1971.

[115] D. A. Borkholder, J. Bao, N. I. Maluf, E. R. Perl, and G. T. A. Kovacs, "Microelectrode arrays for stimulation of neural slice preparations," *Journal of Neuroscience Methods*, vol. 77, no. 1, pp. 61 – 66, 11 1997.

[116] B. Besl and P. Fromherz, "Transistor array with an organotypic brain slice: field potential records and synaptic currents," *European Journal of Neuroscience*, vol. 15, pp. 999 – 1005, 2002.

[117] T. Choi, R. Kaneshiro, R. Brodersen, P. Gray, W. Jett, and M. Wilcox, "High-frequency CMOS switched-capacitor filters for communication applications," *IEEE J. Solid-State Circuits*, vol. SC-18, no. 6, pp. 652 – 664, 1983.

[118] A. Mohr, W. Finger, K. J. Fohr, W. Gopel, H. Hammerle, and W. Nisch, "Performance of a thin film microelectrode array for monitoring electrogenic cells in vitro," *Sensors and Actuators*, vol. 34, pp. 265 – 269, 1996.

[119] V. Lovat, D. Pantratto, L. Lagostena, B. Cacciari, M. Grandolfo, M. Righi, G. Spalluto, M. Prato, and L. Ballerini, "Carbon nanotube substrates boost neuronal electrical signaling," *Nano Letters*, vol. 5, no. 6, pp. 1107 – 1110, 2005.

[120] P. Dayan and L. F. Abbott, *Theoretical Neuroscience*. Cambridge, Massachusetts: The MIT Press, 2001.

[121] W. Dabrowski, P. Grybos, and T. Fiutowski, "Design for good matching in multichannel low-noise amplifier for recording neuronal signals in modern neuroscience experiments," *Microelectronics Reliability*, vol. 44, no. 2, pp. 351 – 361, 2 2004.

[122] D. Auerbach, S. Bantle, S. Keller, V. Hinderling, M. Leu, E. Ehler, and J.-C. Perriard, "Different domains of the m-band protein myomesin are involved in myosin binding and m-band targeting," *Molecular Biology of the Cell*, vol. 10, pp. 1297 – 1308, 1999.

Seite Leer /
Blank leaf

Acknowlegdements

I would like to thank Prof. Dr. Henry Baltes for giving me the opportunity to pursue this work at the Physical Electronics Laboratory. Besides establishing a professional environment, he created an inspiring and team-oriented atmosphere by openly sharing his interdisciplinary way of thinking. I am particularly grateful to Prof. Dr. Andreas Hierlemann for his guidance, support, and motivation throughout this work. He is always well informed about the literature, wants to know how things work and has excellent language skills, from which I was able to profit a lot by him proof-reading my documents.

A special thank goes to Dr. Roland Thewes, who co-refereed this thesis.

Within the Physical Electronics Laboratory, there are many people who helped me realize this work. I thank Wendy Franks, with whom I struggled with the fascinating idea to grow living cells on CMOS chips. We succeeded finally, which is last but not least because of her good teamwork, her chip-processing skills and her candidness in approaching people. I am also indebted to her for the vast amount of proof-reading she did for me. I had the pleasure to share my office with the most interesting persons, who were not only work colleagues to me but also friends. Thanks to Stefano Taschini for all the wonderful discussions. For the time we were sharing the office he acted as my living encyclopaedia. Sadik Hafizović is a fantastic person, he impressed me from the first moment with his relaxed nature, ingenuity and open mind. Thanks to Urs Frey for his very positive personality and his ambition to help wherever he could. By looking at the results he produces, one can get an idea of how well things can be done.

Thanks to Kay-Uwe Kirstein who led the design group at PEL in a very cooperative way, helping out at any time on any problem. He also acted as a co-referee of this thesis. Frauke Greve brought the cell culturing into our lab and helped me out very often with test-chips, cells and fruitful discussions. Ian McKay and Christoph Hagleitner gave me invaluable support on circuit design at the beginning of my thesis. Thanks to Donat Scheiwiller who, besides running our lab equipment, organized the most amazing bike tours, which I enjoyed together

121

with him, Wendy and Sadik. Martin Zimmermann supported our lab in many ways - he kept our design software running, tried to tidy up things and always offered an open ear for questions. Nothing would run at PEL without the excellent work of Erna Hug and Yelena von Allmen in the administration, and Christoph Kolb and Igor Levak in computing systems. Thanks to Timo who kindly offered me his belly whenever I felt the need to pet something. Thanks to all other PELers who supported me in one way or another: Diego Barrettino, Sergio Coronini, Cyril Vancura, Tobias Vancura, Markus Graf, Oliver Brand, Nicole Kerness, Adrian Kummer, Petra Kurzwawski, Dirk Lange, Michael Mayer, Yue Li, Jan Lichtenberg, Jürg Schwizer, Tormod Volden, Rene Pedron, Tomi Salo, and Wan Ho Song.

I am deeply indebted to our project partners from TU Kaiserslautern, Germany. I enjoyed each of my many visits to Kaiserslautern with the objective for a successful measurement. We had a long dry spell, but finally it worked thanks to the patience of Prof. Dr. Axel Blau, Tanja Ugniwenko and Barbara Kochte-Clemens.

I would like to thank the students, with whom I had the pleasure to work: Andreas Dick who designed a best-performing amplifier; Stephan Henry who characterized my chips; Norbert Stoop who never gave up trying to package my chip regardless of the difficulties he had to face; and Marco Fell who transferred the neuron-electrode system into SPICE.

I am thankful for my friends. Raphael has kept me going through darker times, not forgetting all the fun we have had and continue to have in the future. And thanks also to Dr. Tom, Steve, This, Philipp, Mike and Lauch who often reminded me that there are other things besides work.

Last but by no means least, a loving thanks to my mother and sister for their support and Janina for her love.

Publications

Journal Articles

F. Heer, S. Hafizovic, W. Franks, A. Blau, C. Ziegler, A. Hierlemann; "Metal-electrode-based CMOS microsystem for interfacing with neuronal networks", Journal of Solid-State Circuits (submitted).

F. Heer, W. Franks, A. Blau, S. Taschini, C. Ziegler, A. Hierlemann, and H. Baltes, CMOS microelectrode array for the monitoring of electrogenic cells, Biosensors & Bioelectronics, vol. 20, no. 2, pp. 358 - 366, 9 2004.

W. Franks, S. Tosatti, F. Heer, P. Seif, M. Textor, A. Hierlemann, "Self Assembled Structures for Patterned Cell Adhesion on a CMOS Cell-Based Biosensor", Biosensor & Bioelectronics (in press).

Conference Contributions

S. Hafizovic, F. Heer, W. Franks, A. Blau, C. Ziegler, A. Hierlemann, "CMOS Bidirectional Electrode Array for Electrogenic Cells", MEMS 2006, Istanbul, Turkey.

F. Heer, S. Hafizovic, W. Franks, T. Ugniwenko, A. Blau, C. Ziegler, and A. Hierlemann, "Fully integrated 128-electrode CMOS chip for bidirectional interaction with electrogenic cells", in Proc. Eurosensors XIX, Barcelona, Spain, 2005.

F. Heer, S. Hafizovic, W. Franks, T. Ugniwenko, A. Blau, C. Ziegler, and A. Hierlemann, "CMOS microelectrode array for bidirectional interaction with neuronal networks", in Proc. Eur. Solid-State Circuits Conf., Grenoble, France, 2005, pp. 335-338.

F. Heer, W. Franks, I. McKay, S. Taschini, A. Hierlemann, H. Baltes; "Cmos Microelectrode Array for Extracellular Stimulation and Recording of Electrogenic Cells", in Proc. ISCAS Vancouver 2004

W. Franks, F. Heer, S. Tosatti, S. Hafizovic, P. Seif, M. Textor, A. Hierlemann; "CMOS Biosensor with Guided Cell Growth", in Proc. IEEE Sensors, Vienna, Austria, 2004.

W. Franks, S. Tosatti, F. Heer, A. Hierlemann, M. Textor, "Biomimetic self-assembled surfaces for highly selective guided cell growth on cell-based biosensors", in Proc. Biosensors 2004, Granada, Spain.

F. Heer, W. Franks, A. Blau, S. Hafizovic, F. Greve, S. Taschini, C. Ziegler, A. Hierlemann, H. Baltes, "CMOS Microchip for recording and stimulation of electrogenic cells", in Proc. MEA meeting 2004, Reutlingen, Germany.

W. Franks, F. Heer, I. McKay, S. Taschini, R. Sunier, C. Hagleitner, A. Hierlemann, and H. Baltes, "CMOS monolithic microelectrode array for stimulation and recording of natural neural networks", in Proc. IEEE Transducers Conf., vol. 2, Boston, USA, 2003, pp. 963 - 966 vol.2.

Flavio Heer, Sadik Hafzovic, Wendy Franks, Axel Blau, Christiane Ziegler, Stefano Taschini, Andreas Hierlemann, Henry Baltes; "CMOS Neurochip for Stimulation and Recording of Electrogenic Cells"; European Cells & Materials Journal, Vol. 6, Sup. 1, 2003, pp. 95.

Curriculum Vitae

Flavio Heer

Born 11 February 1976 in Sursee, Switzerland

Citizen of Switzerland

November 2005	Defense of the dissertation entitled *CMOS-based Microelectrode Array for Communication with Electrogenic Cells.*
September 2005	ESSCIRC 2005 Young Scientist Award on the paper entitled *CMOS Microelectrode Array for Bidirectional Interaction with Neuronal Networks*
2001 - present	Working at the Swiss Federal Institute of Technology (ETH) in Zürich pursuing the doctoral degree at the Physical Electronics Laboratory under the supervision of Prof. Dr. Andreas Hierlemann and Prof. Dr. Henry Baltes.
March 2001	Degree in Physics from the Swiss Federal Institute of Technology (ETH) in Zürich.
1996 - 2001	Studies in Physics at Swiss Federal Institute of Technology (ETH) in Zürich, Switzerland.
July 1996	Matura Typus C, Gymnasium Kantonsschule Sursee, Luzern.